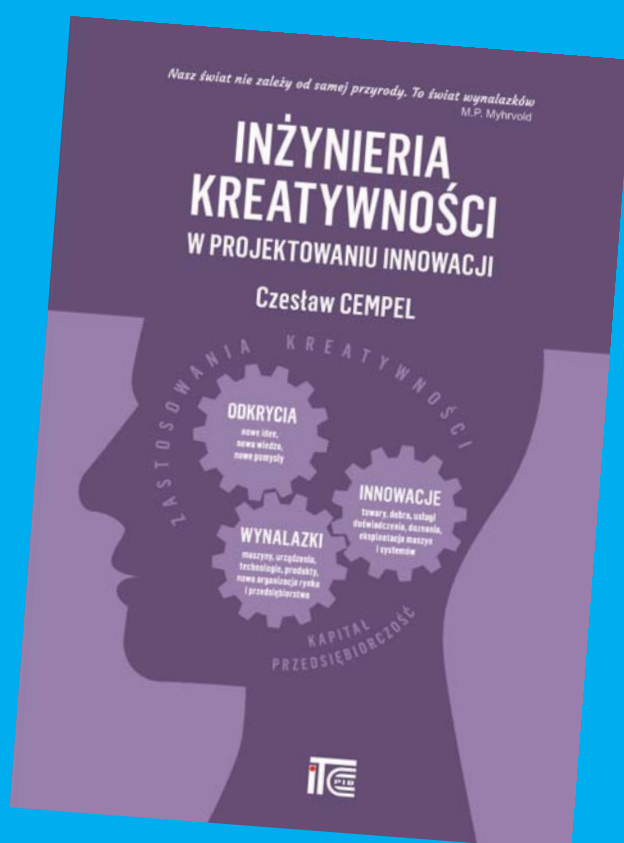




Diagnostyka

Applied Structural Health,
Usage and Condition Monitoring

ISSN 1641-6414



Vol. 14, No. 1

RADA PROGRAMOWA / PROGRAM COUNCIL

PRZEWODNICZĄCY / CHAIRMAN:

prof. dr hab. dr h.c. mult. **Czesław CEMPEL** *Politechnika Poznańska*

REDAKTOR NACZELNY / CHIEF EDITOR:

prof. dr hab. inż. **Wiesław STASZEWSKI** *AGH w Krakowie*

CZŁONKOWIE / MEMBERS:

prof. dr hab. inż. **Jan ADAMCZYK**
AGH w Krakowie

prof. **Francesco AYMERICH**
University of Cagliari – Italy

prof. **Jérôme ANTONI**
University of Technology of Compiègne – France

prof. dr. **Ioannis ANTONIADIS**
National Technical University Of Athens – Greece

dr inż. **Roman BARCZEWSKI**
Politechnika Poznańska

prof. dr hab. inż. **Walter BARTELMUS**
Politechnika Wroclawska

prof. dr hab. inż. **Wojciech BATKO**
AGH w Krakowie

prof. dr hab. inż. **Adam CHARCHALIS**
Akademia Morska w Gdyni

prof. **Li CHENG**
The Hong Kong Polytechnic University – China

prof. dr hab. inż. **Wojciech CHOLEWA**
Politechnika Śląska

prof. dr hab. inż. **Zbigniew DĄBROWSKI**
Politechnika Warszawska

prof. **Charles FARRAR**
Los Alamos National Laboratory – USA

prof. **Wiktor FRID**
Royal Institute of Technology in Stockholm – Sweden

dr inż. **Tomasz GAŁKA**
Instytut Energetyki w Warszawie

prof. **Len GELMAN**
Cranfield University – England

prof. **Mohamed HADDAR**
National School of Engineers of Sfax – Tunisia

prof. dr hab. inż. **Jan KICIŃSKI**
IMP w Gdańsku

prof. dr hab. inż. **Daniel KUJAWSKI**
Western Michigan University – USA

prof. **Graeme MANSON**
University of Sheffield – UK

prof. dr hab. **Wojciech MOCZULSKI**
Politechnika Śląska

prof. dr hab. inż. **Stanisław RADKOWSKI**
Politechnika Warszawska

prof. **Bob RANDALL**
University of South Wales – Australia

prof. dr **Raj B. K. N. RAO**
President COMADEM International – England

prof. **Riccardo RUBINI**
University of Modena and Reggio Emilia – Italy

prof. **Massimo RUZZENE**
Georgia Institute of Technology – USA

prof. **Vasily S. SHEVCHENKO**
BSSR Academy of Sciences Mińsk – Belarus

prof. **Menad SIDAHMED**
University of Technology Compiègne – France

Prof. **Tadeusz STEPINSKI**
Uppsala University - Sweden

prof. **Wiesław TRĄMPCZYŃSKI**
Politechnika Świętokrzyska

prof. dr hab. inż. **Tadeusz UHL**
AGH w Krakowie

prof. **Vitalijus VOLKOVAS**
Kaunas University of Technology – Lithuania

prof. **Keith WORDEN**
University of Sheffield – UK

prof. dr hab. inż. **Andrzej WILK**
Politechnika Śląska

dr **Gajraj Singh YADAVA**
Indian Institute of Technology – India

prof. dr hab. inż. **Radosław ZIMOROZ**
Politechnika Wroclawska

prof. dr hab. inż. **Bogdan ŻÓLTOWSKI**
UTP w Bydgoszczy

WYDAWCA:

Polskie Towarzystwo Diagnostyki Technicznej
ul. Narbutta 84
02-524 Warszawa

REDAKTOR NACZELNY:

prof. dr hab. inż. **Wiesław STASZEWSKI**

SEKRETARZ REDAKCJI:

dr inż. **Sławomir WIERZBICKI**

CZŁONKOWIE KOMITETU REDAKCYJNEGO:

dr inż. **Krzysztof LIGIER**
dr inż. **Paweł MIKOŁAJCZAK**

ADRES REDAKCJI:

Redakcja Diagnostyki
Katedra Budowy, Eksploatacji Pojazdów i Maszyn
UWM w Olsztynie
ul. Oczapowskiego 11, 10-736 Olsztyn, Poland
tel.: 89-523-48-11, fax: 89-523-34-63
www.diagnostyka.net.pl
e-mail: redakcja@diagnostyka.net.pl

KONTO PTDT:

Bank PEKAO SA O/Warszawa
nr konta: 33 1240 5963 1111 0000 4796 8376

NAKLAD: 500 egzemplarzy

Spis treści / Contents

Michele COTOGNO, Marco COCCONCELLI, Riccardo RUBINI – <i>University of Modena and Reggio Emilia</i> ...3 A Window based method to reduce the end-effect in empirical mode decomposition	
Marek FIDALI, Wojciech JAMROZIK, Anna BZYMEK, Anna TIMOFIEJCZUK – <i>Politechnika Śląska</i> 11 Segmentation of welding arc images for purposes of welding diagnostics <i>Segmentacja obrazów łuku spawalniczego dla potrzeb diagnostyki spawania</i>	
Waldemar MIRONIUK – <i>Akademii Marynarki Wojennej</i> 19 Analysis of compartments flooding time and metacentric height after hull damage <i>Analiza czasu zatopienia przedziału okrętowego i wysokości metacentrycznej po uszkodzeniu kadłuba</i>	
Łukasz BREŃKACZ, Paweł BAGIŃSKI, Małgorzata BOGULICZ – <i>Institute of Fluid-Flow Machinery – Polish Academy of Sciences</i> 25 Dynwir S-70 program for modal analysis of multisupported and multimass rotors <i>Dynwir S-70 program do analizy modalnej wielopodporowych i wielomasowych wirników</i>	
Mirosław PAJOR, Henryk MAĆKOWIAK, Jacek ZAPŁATA – <i>West Pomeranian University of Technology of Szczecin</i> 31 Examination of thermal deformation of micro milling machine tool SNTM-CM-ZUT-1 <i>Ocena odkształceń cieplnych obrabiarki do mikrofrezowania SNTM-CM-ZUT-1</i>	
Kajetan DZIEDZIECH, Wiesław J. STASZEWSKI, Tadeusz UHL – <i>AGH University of Science and Technology in Kraków</i> 37 Time-frequency analysis of time-variant systems <i>Czasowo-częstotliwościowa analiza systemów zmiennych w czasie</i>	
Tomasz WRÓBLEWSKI, Agnieszka PEŁKA – SAWENKO, Małgorzata ABRAMOWICZ, Stefan BERCZYŃSKI – <i>West Pomeranian University of Technology of Szczecin</i> 43 Parameter identification of steel-concrete composite beams by finite element method <i>Identyfikacja parametrów stalowo-betonowych belek zespolonych metodą elementów skończonych</i>	
Piotr KOHUT, Krzysztof HOLAK, Krzysztof MENDROK, Wojciech MAJ – <i>AGH University of Science and Technology in Kraków</i> 47 Structure's damage detection supported by contact and contact-less global methods <i>Wykrywanie uszkodzeń konstrukcji z wykorzystaniem globalnych metod kontaktowych i bezkontaktowych</i>	
Przemysław MAGDA, Tadeusz UHL – <i>AGH University of Science and Technology in Kraków</i> 57 Maintenance on demand for vehicle suspension system <i>Monitorowanie stanu zawieszenia w pojazdach</i>	
Grzegorz ŻYWICA, Paweł BAGIŃSKI, Łukasz BREŃKACZ – <i>Institute of Fluid-Flow Machinery, Polish Academy of Sciences</i> 65 Dynamic state assessment of the water turbine with the power of 600 kW <i>Ocena stanu dynamicznego turbiny wodnej o mocy 600 kW</i>	
Andrzej SOBOLEWSKI, Paweł OSTAPKOWICZ – <i>Białystok University of Technology</i> 71 Leak detection in liquid transmission pipelines using statistical analysis <i>Detekcja przecieku płynów w rurociągach za pomocą analizy statystycznej</i>	
Warto przeczytać / Worth to read 78	

A WINDOW BASED METHOD TO REDUCE THE END-EFFECT IN EMPIRICAL MODE DECOMPOSITION

Michele COTOGNO, Marco COCCONCELLI, Riccardo RUBINI

Department of Science and Engineering Methods, University of Modena and Reggio Emilia, 2, Amendola street, Morselli Building, 42122 Reggio Emilia, Italy

michele.cotogno@unimore.it, marco.cocconcelli@unimore.it, riccardo.rubini@unimore.it

Abstract

Empirical Mode Decomposition technique (EMD) is a recent development in non-stationary and non-linear data analysis. It is an algorithm which adaptively decomposes the signal in the sum of Intrinsic Mode Functions (IMFs) from which the instantaneous frequency can be easily computed. EMD has proven its effectiveness but is still affected from various problems. One of these is the “end-effect”, a phenomenon occurring at the start and at the end of the data due to the splines fitting on which the EMD is based. Various techniques have been tried to overcome the end-effect, like different data extension or mirroring procedures at the data boundary. In this paper we made use of the IMFs orthogonality property to apply a symmetrical window to the data before EMD for end-effect reduction. Subsequently the IMFs are post-processed to compensate for data alteration due to windowing. The simulations show that IMFs obtained with this method are of better quality near the data boundaries while remaining almost identical to classical EMD ones.

Keywords: Empirical Mode Decomposition, Intrinsic Mode Functions, end-effect problem, windowing.

1. INTRODUCTION

The Empirical Mode Decomposition (EMD) is a signal processing method firstly developed by N.E. Huang [5] particularly suited for non-linear and non-stationary data analysis. It aims to decompose the signal in the sum of Intrinsic Mode Functions (IMF) rather than sinusoidal functions (as Fourier transform does) or other a priori chosen expansion basis. The IMFs represent single oscillatory modes leading to meaningful instantaneous frequency estimates, so far allowing a better insight on the physical processes involved in the data under analysis. In fact, an IMF is a function defined in [5] as follows:

- 1) in the whole dataset, the number of extrema and the number of zero-crossings must either equal or differ at most by one;
- 2) at any point, the mean value of the envelope defined by the local maxima and the envelope defined by the local minima is zero.

In another words an IMF is almost symmetric with a unique local frequency. The properties of the IMF also set the convergence criterion of EMD. The EMD procedure is described as following:

- 1) find out the local maxima and the local minima of the signal $s(t)$ firstly, then the upper (lower) envelope can be get as the cubic spline interpolation of the maxima (minima).
- 2) Compute the mean envelope $m(t)$ as the average of the upper envelope and the lower one. Let $h = s(t) - m(t)$ be the new signal and repeat the procedure above up to h satisfies the IMF definition, then set $c_i = h$.
- 3) Separate the IMF from the signal, $r_{i+1} = s(t) - c_i$.

- 4) Let r_{i+1} be the new signal now (i.e. $s(t) = r_{i+1}$), repeat the sifting until the final residue $r_n(t)$ has at most one extreme or it is a constant or a monotonic function. Thus:

$$s(t) = \sum_{i=1}^n c_i(t) + r_n(t) \quad (1)$$

The obtained IMFs form a local orthogonal basis as stressed in [5], although orthogonality can't be theoretically proved. In fact, the EMD method is totally data adaptive - leading to the aforementioned advantages in non-linear and non-stationary data analysis - but still lacks of a firm mathematical background. This is the main cause of two of the principal problems of EMD process, which are the convergence criterion and the end-effect, the latter being treated in this paper. The convergence criterion declares if the result of the last completed sifting is an IMF or not. In the EMD literature various criteria are proposed and here we recall some of the principal ones. In [5] is made use of a Cauchy type convergence criterion which stops the sifting process at iteration k when the parameter SD_k is less than a predetermined value. SD_k is defined as follows:

$$SD_k = \frac{\sum_{t=0}^T [h_{k-1}(t) - h_k(t)]^2}{\sum_{t=0}^T [h_{k-1}(t)]^2} \quad (2)$$

where k is the actual iteration number, t is the signal sample index and T is the signal's total samples number. Typically, the stopping values for SD lie in the 0.2 - 0.3 range. In this paper we made use of this

stopping criterion, and the SD stopping value had been set to 0.2. In [2] the Mean Value criterion is illustrated, where the SD value is simply the mean envelope $m(t)$ at current iteration and must be smaller than a predetermined value everywhere to stop sifting. In [6] the Fixed Siftings criterion is proposed, where the sifting process is stopped after a given number of iterations (typically around 10). In [4] the S -number criterion is illustrated, where the sifting is stopped when for S consecutive iterations the signal's number of extrema and zero crossings stay the same and are equal or differ at most by one. Typical values for S are in the 4 - 8 range. The next sections will discuss the end-effect problem in details, and propose a windowing method to reduce it. The reduction of the end-effect problem is the main target and novelty of this paper.

2. THE EMD END-EFFECT

The end-effect is a phenomenon occurring in EMD due to splines fitting at the beginning and at the end of the data. The upper and lower envelope in the sifting process will swing at the two ends of the data sequence, due to the lack of constraints for the spline definition. If we adopt the classical mathematic definition of local extrema in a limited set, a boundary data point is always a local maximum or minimum, depending on the following data point (or the preceding one if the data point considered is the last one). Therefore, there is always one spline of the two envelopes to be calculated (upper and lower) which lacks of definition between the first (or last) local extrema and the data boundary. This results in a swing of the envelope splines (and consequently of the mean spline) that will gradually pollute inside the whole data sequence making the result seriously distorted, particularly the lowest frequency IMFs (which are the last extracted by the sifting process). As previously mentioned, this IMFs corruption is called end-effect in the EMD jargon. Researchers have been developing several techniques to reduce the end-effect, the most of them dealing with signal extension outside the endpoints in order to resolve the splines uncertain definition at the boundaries. Direct data mirroring [7] is an operation that chooses two endpoints of a signal as the mirror positions, expands it beyond the two mirrors in the outside directions, and obtains a new periodic signal with a length of two times the original one. Since only the extrema are needed for envelopes calculation, the natural update of the mirroring method aims to the correct estimation of the data extrema beyond the boundaries by means of existing signal processing tools. In [1] this is achieved by virtue of a neural network estimation, while in [8] the extrema extension is done by the use of a Support Vector regression at both endpoints. In [10] the Ratio Boundary Extension technique is proposed, an approach that couples the mirror expansion with the extrapolation prediction of regression function to the treatment of end-effects, with extrema estimation by means of a quadratic

interpolation on the near-endpoints extrema. Other works are concerned with applications of Auto-Regressive and Moving-Average (ARMA) modeling [3], polynomial regression and so on. In our view, all of these kinds of signal processing tend to loose the philosophical approach of EMD which is the source of its powerful outcomes. In fact, the aforementioned signal processing tools have been developed on some starting hypotheses on the data that the original EMD doesn't guess (due to its algorithmic form), thus potentially losing the non-stationary/non-linear adaptability of EMD. Moreover, the end-effect problem could still remain due to the fact that even if extended perfectly, a digitized signal has always two endpoints to deal with. In our view the original EMD approach (i.e.: no a priori hypothesis on the data) is conserved, and in the next section we propose a signal symmetrical windowing in order to reduce the end-effect.

3. A WINDOW BASED METHOD TO REDUCE EMD END-EFFECT

The basic idea is similar to the one proposed in [9], where the signal is symmetrical windowed in order to have always the endpoints with zero value. By doing this, during the sifting process the upper and lower envelope are forced to have the first and the last point with zero value, resolving the uncertainty of the envelope value at the endpoints. Unlike in [9] where a "flat top" and classic cosine windows were used, such as Hanning and Hamming, we made use of a triangular window (also called Bartlett window) in order to give less weight to the signal near the boundaries and no significance at all at the endpoints, where the windows is zero valued. This approach simulates the perspective of the human eye watching the horizon: the further one watch, the less detail is retrieved (i.e.: the less certainty on what is being looked at). In our case, the "observer" is placed in the middle of the signal and his horizons are the endpoints, by virtue of the windowing. Furthermore, if $w(t)$ is the window, we rewrite Eq. 1 for the windowed signal as:

$$w(t)s(t) = w(t) \left(\sum_{i=1}^n c_i(t) + r_n(t) \right) \quad (3)$$

Since the EMD process separates the IMFs simply by differentiation, and IMFs are locally orthogonal, we thought that we could extract the IMFs of the windowed signal and subsequently multiply them by $1/w(t)$, obviously rejecting the endpoints where the window reciprocal is infinite (i.e.: multiply both sides of Eq. 3 by $1/w(t)$ where possible). By doing this, we should be able to retrieve the original signal's IMFs. To prove the effectiveness of this procedure, we tested it on simulated data and the results are compared with the standard EMD without any end-effect compensation.

4. SIMULATIONS AND DISCUSSION OF THE RESULTS

The window based method proposed had been tested on different simulated signals, all of which have a sampling frequency of 10 kHz and a timespan of 5 seconds. We tested the triangular window, described by the following Eq. 4:

$$w(t) = 1 - \left| \frac{t-a}{a} \right| \quad (4)$$

where $a = T/2$ is half the length of the signal. The first signal tested is given by the following Eq. 5, and is reported in Fig. 1a along with its windowed version (Fig. 1b).

$$s_1(t) = \sin(2\pi \cdot 0.5 \cdot t) \cdot \sin(2\pi \cdot 20 \cdot t) + 0.1 \cdot \cos(2\pi \cdot 10 \cdot t) + t(2-t) \quad (5)$$

$s_1(t)$ is the sum of an amplitude modulated (AM) sine, a cosine and a parabolic term: this is done to evaluate the effect of windowing when the data is composed of simple oscillating functions and a

nonlinear “trend”. In this case, applying the direct mirror extension will fail due to the parabolic term induced boundaries asymmetry. From this signal the standard EMD extracts three IMFs (Fig. 2a – Fig. 2c)) while the proposed method with triangular window extract 4 IMFs (Fig. 2d – Fig. 2g). It can be seen how in this case the windowing doesn’t corrupt the IMFs far from the endpoints while some swing still occurs. It is also noticeable how the second IMF from the standard EMD (Fig. 2b) suffers the end-effect probably due to some mode-mixing with the nonlinear (parabolic) trend, while the proposed method doesn’t fail (Fig. 2e). In fact, the trend extracted by the standard EMD (Fig. 2c) is distorted near the right endpoint to compensate for the previous IMF corruption whilst the window method is not affected by the cited phenomenon, but the latter spreads the trend in two components (Fig. 2f – Fig. 2g). Finally, notice that the triangular window discontinuity at the center point is reflected in the residual IMFs (Fig. 2f – Fig. 2g) extracted by the proposed method.

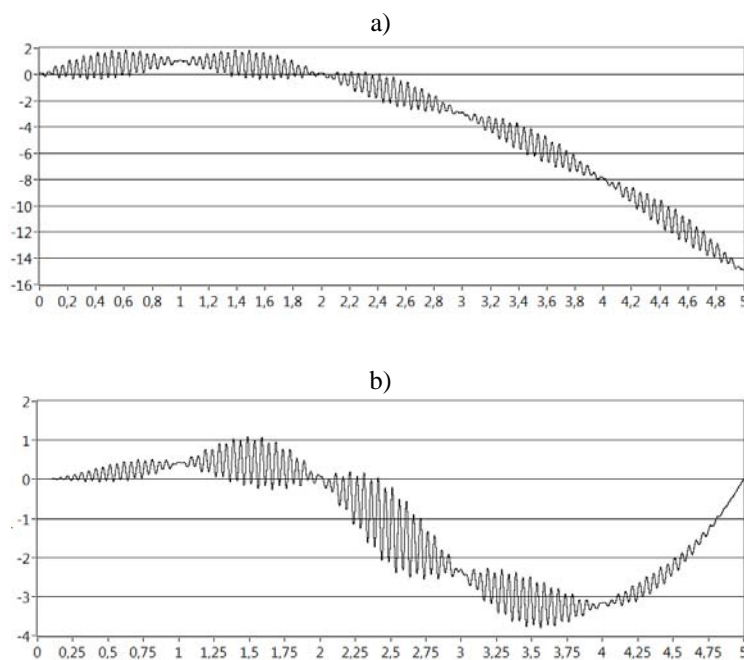


Figure 1. $s_1(t)$ (a) and its triangular windowed version (b)

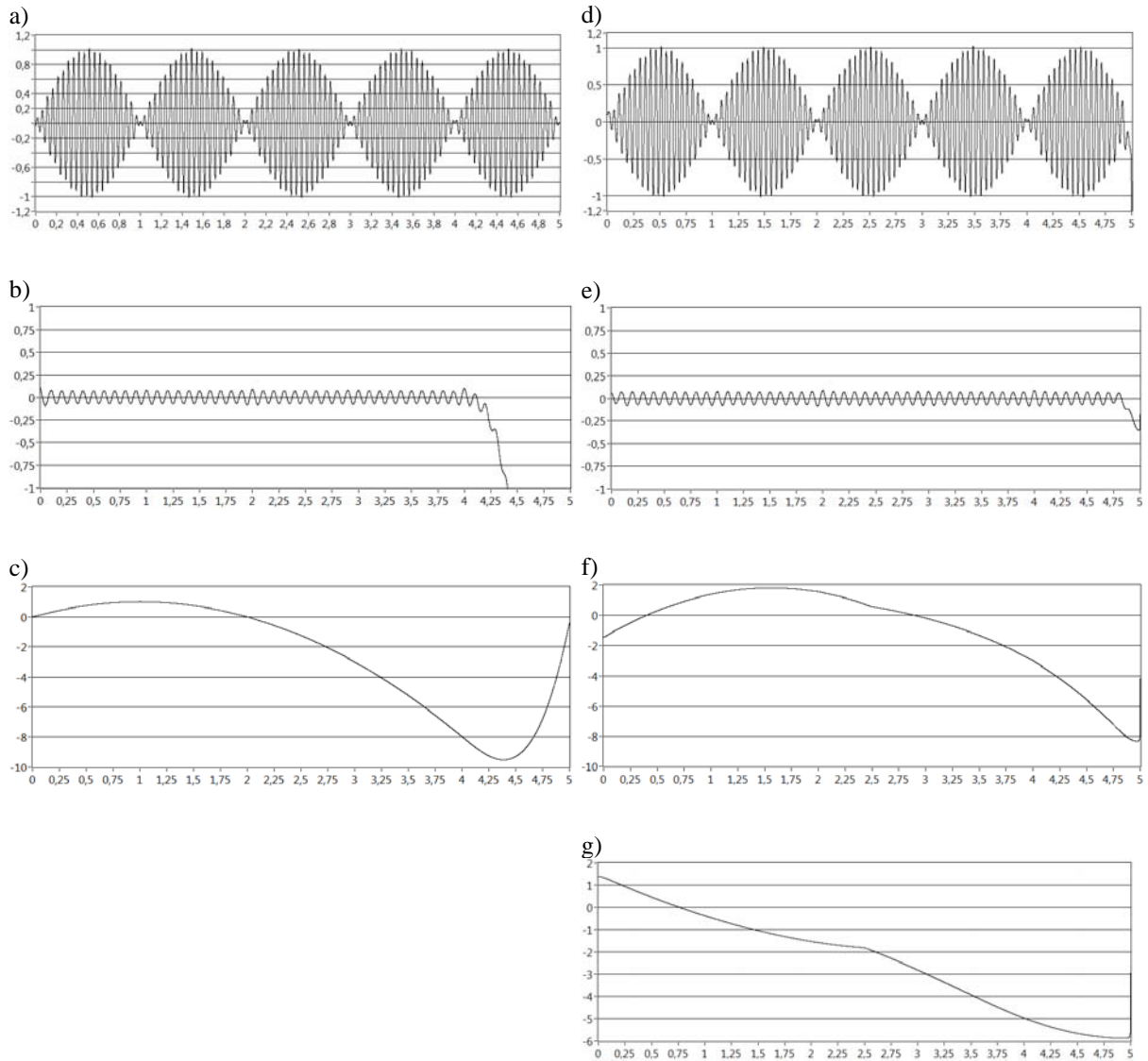


Figure 2. In the left column (a-c) the IMFs extracted by the standard EMD from $s_1(t)$, whilst in the right column (d-g) the corresponding IMFs extracted by the proposed windowing method

The second simulated signal $s_2(t)$ is given by the following Eq. 6 and it is illustrated in Fig. 3a along with its windowed counterpart (Fig 3b):

$$s_2(t) = \sin(2\pi \cdot 0.5 \cdot t) \cdot \sin(2\pi \cdot 20 \cdot t) + \sin(2\pi \cdot e^t) + t(2-t) \quad (6)$$

$s_2(t)$ embodies an AM sine, an exponential chirp and a parabolic term in order to evaluate the performance of the algorithm in presence of a strongly nonlinear component. Since in the proposed method we

implemented the standard EMD we expect also strong mode-mixing in the IMFs due to the chirp. In the EMD jargon the mode-mixing denotes the split of a signal component among two or more IMFs. A characteristic example is indeed the chirp signal, its frequency components cover a wide band spectrum and they consequently appear in different IMFs. In Fig. 4 are reported the results of the simulation; standard EMD extracts four IMFs and also does windowed EMD. It can be seen how the IMFs behavior is very similar between the two methods also in presence of strong mode-mixing and nonlinear components.

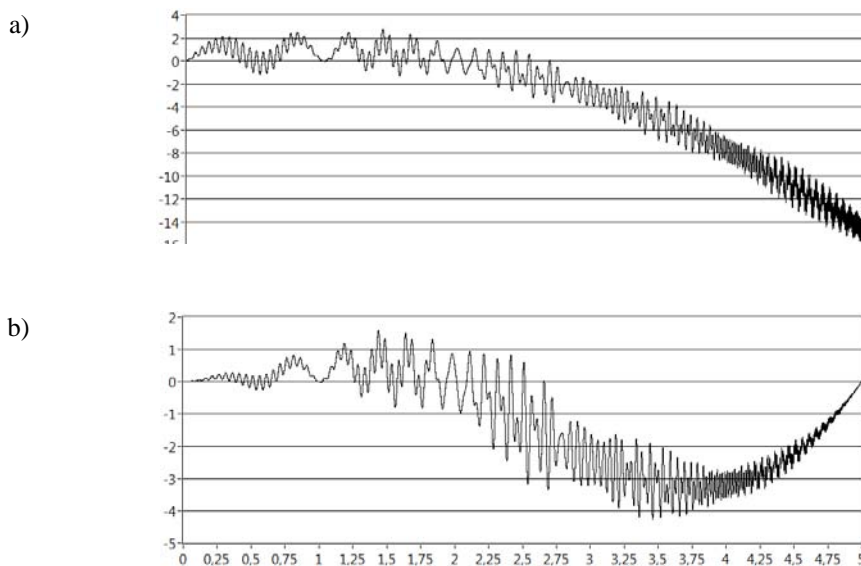


Figure 3. Simulated signal $s_2(t)$ (a) and its triangular windowed version (b)

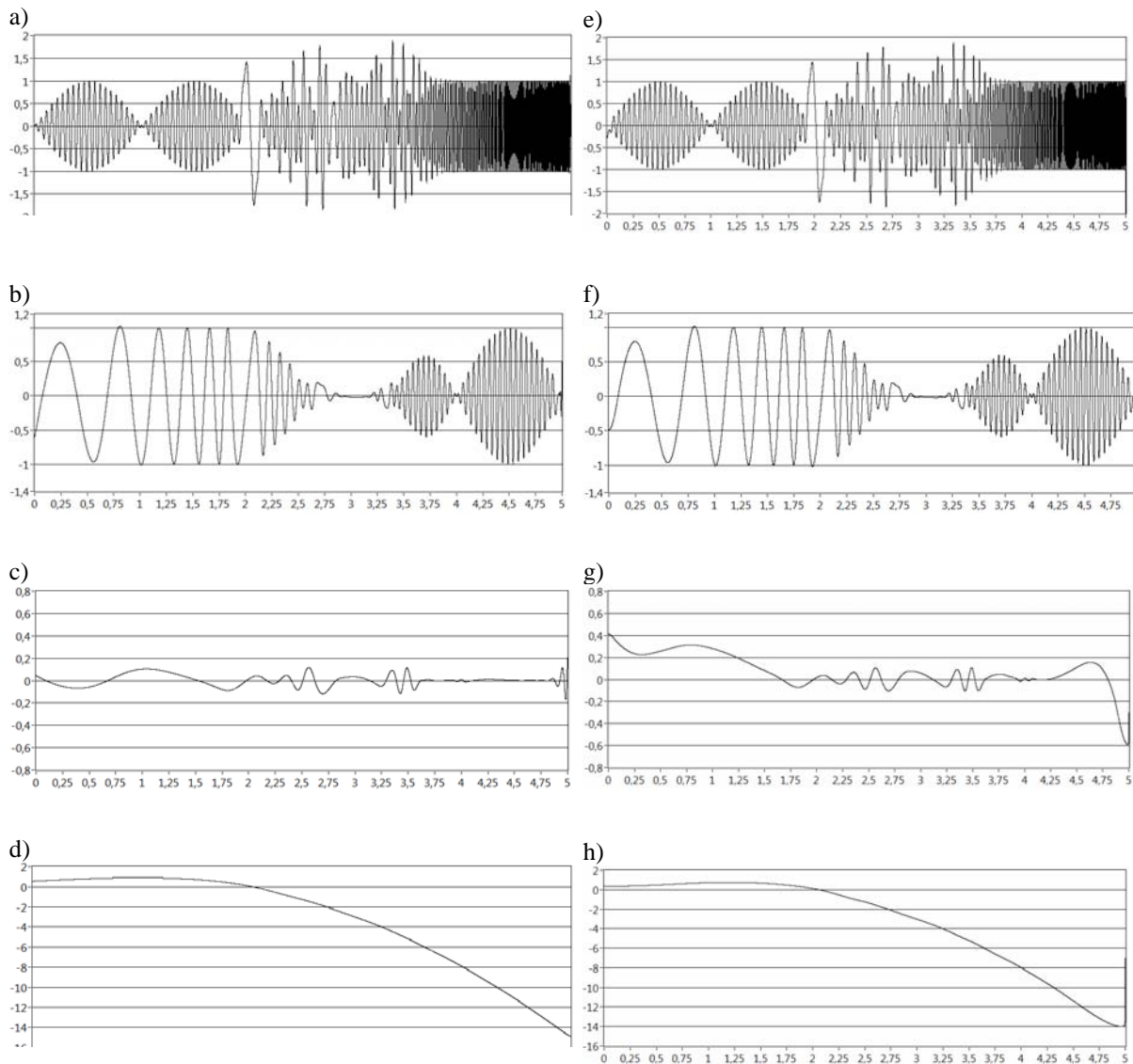


Figure 4. In the left column (a-d) the IMFs extracted by the standard EMD from $s_2(t)$, whilst in the right column (e-h) the corresponding IMFs extracted by the proposed windowing method

The main difference in the two IMF sets is in the third IMF since in the window method's one (Fig. 4g) there is more swing at the beginning than the standard EMD counterpart (Fig. 4c): however, this IMF seems to be a mode-mixing product of EMD.

The last simulated signal tested, $s_3(t)$, is reported in Fig. 5a along with its windowed version (Fig. 5b) and is given by the following Eq. 7:

$$s_3(t) = \sin(2\pi \cdot 0.1 \cdot t) \cdot \sin(2\pi \cdot 20 \cdot t) + e^{1-t} \cos(2\pi \cdot 10 \cdot t) + t(2-t)(4-t) \quad (7)$$

$s_3(t)$ embodies an AM sine, a fading cosine function and a polynomial function acting as a nonlinear trend; this is done in order to compare the performances of the proposed algorithm in case of this kind of signal mixture from the ability of signal's component retrieval point of view. The obtained IMFs are reported in Fig. 6.

In this case again mode-mixing is present, as expected. The first IMFs are very similar, but the one gathered by the windowed EMD (Fig. 6e) offers

a more precise representation of the original component near the left endpoint in terms of its decaying amplitude dynamics. The second IMF from the standard EMD (Fig. 6b) shows what at a first glance could be judged as a swing resulting from the end-effect: in our view, the swing comes from mode-mixing of the fading cosine with the nonlinear (cubic) trend which is subsequently spread in the following IMFs (Fig. 6c – Fig. 6d). The second IMF, windowed version, (Fig. 6f) shows a similar effect but much more limited in amplitude: in fact, the following IMFs (Fig. 6g – Fig. 6h) represents in a better fashion the nonlinear trend. The latter is split in two components probably because of its dynamics (i.e.: oscillations) indeed the zero crossings in the third IMF (Fig. 6g) occur near $t=2$ and $t=4$ which are the real component's zeroes, while almost no trace of the same information could be retrieved from the standard EMD correspondent third and fourth IMF (Fig. 6c – Fig. 6d respectively).

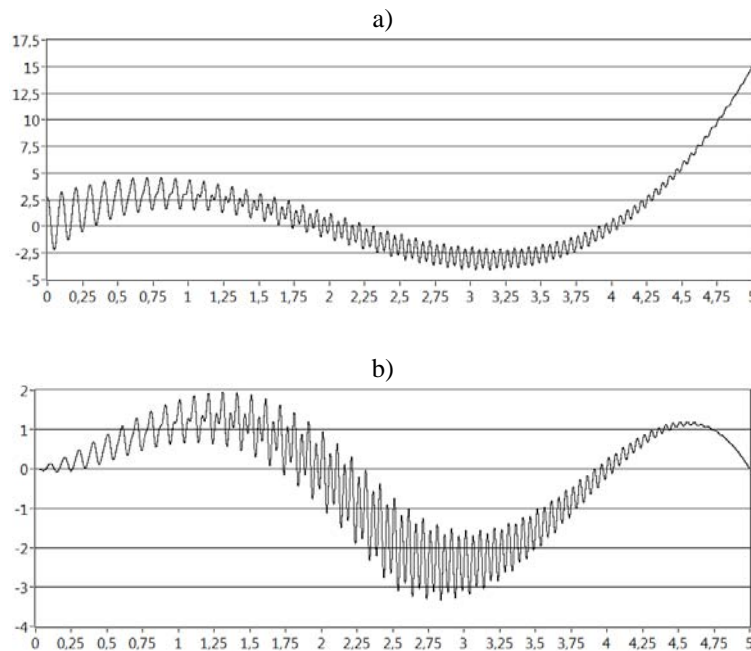


Figure 5. Simulated signal $s_3(t)$ (a) and its triangular windowed version (b)

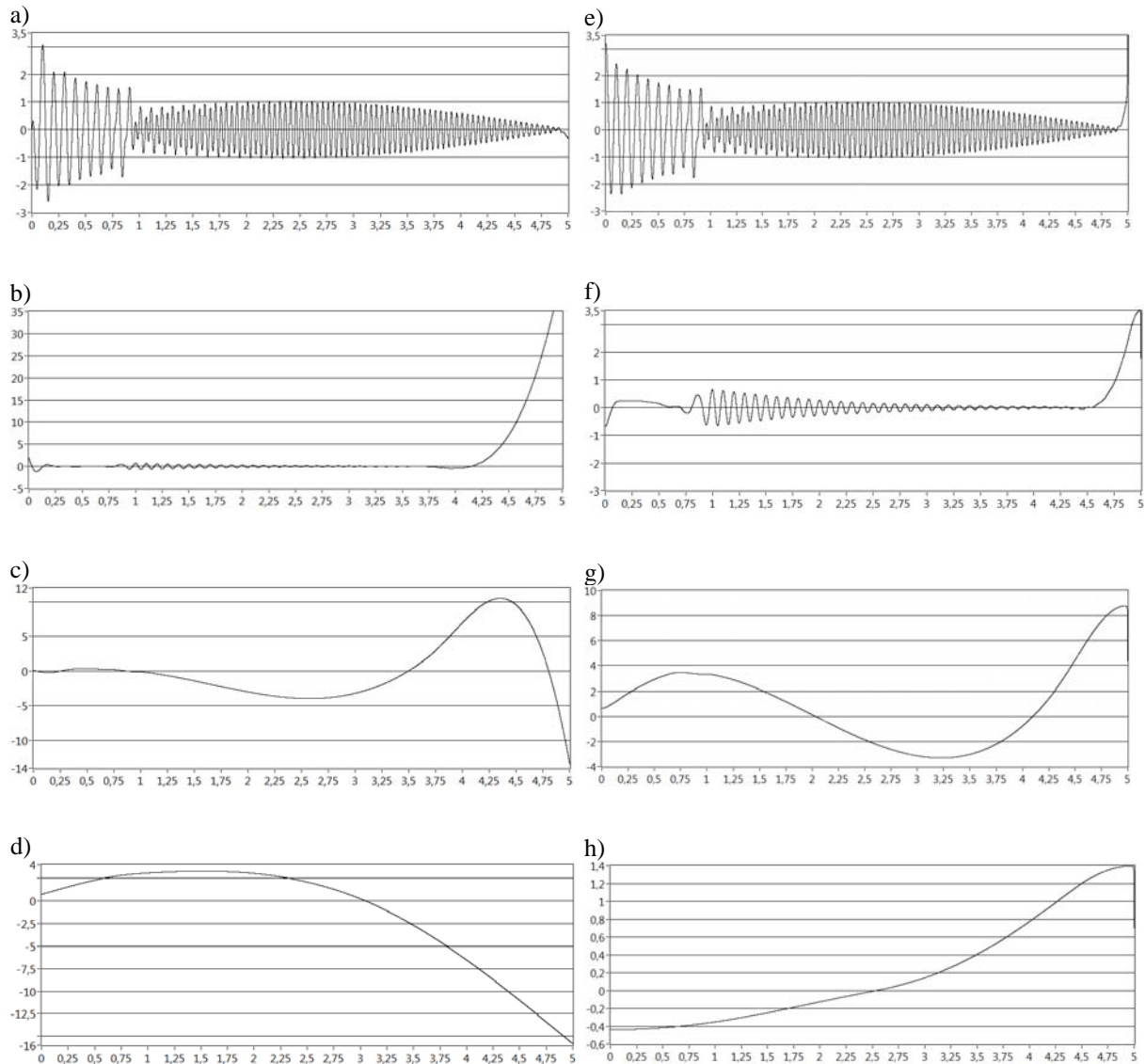


Figure 6. In the left column (a-d) the IMFs extracted by the standard EMD from $s_3(t)$, whilst in the right column (e-h) the corresponding IMFs extracted by the proposed windowing method

5. CONCLUSIONS

The presented signal windowing method for EMD end-effect reduction works well: cases have been showed where end-effect or mode-mixing induced swings in IMFs are strongly reduced. Swings still occur near the endpoint, but their amplitude is smaller than in standard EMD. In some cases, the proposed method produced better quality IMFs in presence of strong mode-mixing. The simulations performed (here we reported a few extracts because of available space) have shown in general a more precise representation of the low frequency component(s) particularly in case of asymmetry of the data. These results are obtained while maintaining the EMD data adaptability since no a priori assumption is made on the signal (or parts of it), in contrast with other techniques dealing with EMD end-effect which do (explicitly or implicitly). In our view, another important result comes from the use of the local orthogonality of the

IMFs which allows us to compensate for the signal windowing by multiplication by the window reciprocal after the IMF extraction. We think that this behavior of EMD should be taken in consideration by the researchers who are working on mathematical base for EMD. In fact, since EMD is defined only as an algorithm it was not certain if this operation (i.e., windowing and post EMD windowing compensating) could have produced consistent results. Moreover, we think that a mode-mixing avoiding technique could also improve the performance of windowed EMD particularly in presence of divergent trends near the endpoints.

6. ACKNOWLEDGEMENTS

The authors wish to thank the Inter Departmental Research Center INTERMECH MoRE of the University of Modena and Reggio Emilia for the financial support.

REFERENCES

- [1]. Y. Deng, W. Wang, C. Qian, Z. Wang, D. Dai, *Boundary-processing-technique in EMD method and Hilbert transform*. Chinese Science Bulletin Vol. 46, No. 1 (2001).
- [2]. P. Flandrin, G. Rilling, P. Goncalves, *Empirical mode decomposition as a filter bank*. Signal Processing Letters, IEEE, 11(2) (2004) 112–114.
- [3]. Q. Gai, X.-J. Ma, H.-Y. Zhang, Y.-K. Zou, *New method for processing end effect in local wave method*. J. Dalian Univ. Technol. 42 (1) (2001) 115–117.
- [4]. N. E. Huang, M. Wu, S. R. Long, S. P. Shen, W. Qu, P. Gloersen, K. L. Fan, *A confidence limit for the empirical mode decomposition and Hilbert spectral analysis*. Proc. R. Soc. Lond. A, 459 (2003)2317–2345.
- [5]. N. E. Huang, Z. Shen, S. R. Long, M. L. Wu, H. H. Shih, Q. Zheng, N. C. Yen, C. C. Tung, H. H. Liu, *The empirical mode decomposition and Hilbert spectrum for nonlinear and non-stationary time series analysis*. Proc. R. Soc. London, Ser. A 454 (1998) 903–995.
- [6]. N. E. Huang, Z. Wu, G. Wang, X. Chen, F. Qiao, *On intrinsic mode function*, Adv. in Adaptive Data Analysis. Vol. 2, No. 3 (2010) 277–293.
- [7]. Y. S. Lee, S. Tsakirtzis, A. F. Vakakis, L. A. Bergman, D.M. McFarlan, *Physics-based foundation for empirical mode decomposition*. Adv. in Adaptive Data Analysis, Vol. 47, No. 12 (2009) 2938–2963.
- [8]. D. Lin, Z. Guo, F. An, F. Zeng, *Elimination of end effects in empirical mode decomposition by mirror image coupled with support vector regression*. Mechanical Systems and Signal Processing 31 (2012) 13–28
- [9]. D. Ren, S. Yang, Z. Wu, G. Yan, *Evaluation of the EMD end effect and a window based method to improve EMD*. International Technology and Innovation Conference, November 6-7 (2006) China.
- [10]. Q. Wu, S. D. Riemenschneider, *Boundary extension and stop criteria for empirical mode decomposition*. Adv. in Adaptive Data Analysis, Vol. 2, No. 2 (2010) 157–169.



Michele COTOGNO was born in Italy on October 23rd, 1984. He is a research fellower in Applied Mechanics at the University of Modena and Reggio Emilia, Reggio Emilia, Italy. His research interests include bearings, CBM and machine diagnostics.



Marco COCCONCELLI was born in Italy on November 9th, 1977. He is a researcher in Applied Mechanics at the University of Modena and Reggio Emilia, Reggio Emilia, Italy. His research interests include machine diagnostics, bearings, CBM and vibration analysis.



Riccardo RUBINI was born in Italy on July 11th, 1965. He is an Associate Professor in Applied Mechanics at the University of Reggio Emilia (Italy). His research interests include machines dynamics, advanced techniques for the monitoring and diagnostics of mechanical components.

SEGMENTATION OF WELDING ARC IMAGES FOR PURPOSES OF WELDING DIAGNOSTICS

Marek FIDALI, Wojciech JAMROZIK, Anna BZYMEK, Anna TIMOFIEJCZUK

Politechnika Śląska, Wydział Mechaniczny Technologiczny, Instytut Podstaw Konstrukcji Maszyn
Konarskiego 18a, 44-100 Gliwice, 32 237 13 60, marek.fidali@polsl.pl

Summary

The paper concerns the research on diagnostics of a welding process. The estimation of the process state is being performed by means of the analysis of infrared images and images recorded within visible range of electromagnetic radiation. To carry out the image analysis it is necessary to cut out the area called region of interests (ROI). In case of welding which is the dynamical process this operation appeared complicated. The most important point of the operation is image segmentation. The author proposed and tested an algorithm of the definition of the ROI as well as verified numerous image segmentation methods.

Keywords: process diagnostics, welding monitoring, infrared, image fusion, image processing.

SEGMENTACJA OBRAZÓW ŁUKU SPAWALNICZEGO DLA POTRZEB DIAGNOSTYKI SPAWANIA

Streszczenie

W artykule przedstawiono badanie nakierowane na diagnozowanie procesu spawania. Estymacja stanu procesu była przeprowadzana poprzez zastosowanie metod analizy obrazów termowizyjnych, jak również obrazów zarejestrowanych w widzialnym paśmie promieniowania elektromagnetycznego. Przeprowadzenie analizy obrazów wymagało wyboru i wycięcia obszaru, zwanego regionem zainteresowania (ang. region of interests, ROI). W przypadku spawanie będącego procesem bardzo dynamicznym operacja ta jest dość skomplikowana, a jej najważniejszym etapem jest segmentacja obrazu. Autorzy zaproponowali i zweryfikowali algorytm definiowania ROI, przy zastosowaniu kilku różnych metod segmentacji obrazów.

Słowa kluczowe: diagnostyka procesów, monitorowanie spawania, fuzja obrazów, przetwarzanie obrazów

1. INTRODUCTION

Monitoring and diagnosing of a welding process with use of vision systems is nowadays an object of interest of many research institutes and industrial companies [1, 2, 3, 4]. In the Department of Fundamentals of Machinery Design (Silesian University of Technology), research concerning welding process diagnostics with use of multisensor data fusion, has been carried out for several years [5, 6]. One of tasks being realized has been an application of image fusion of welding arc infrared and regular images. The goal is to diagnose the welding process [7, 8].

An evaluation of the welding process state is performer on the background of image series recorded during the process. Every image of the series is processed and analysed. As the result one or some relevant features are being obtained. Values of these features arranged in time order are considered as diagnostic signals. They are fundamental to basic diagnostic stages such as defect detection, localization and identification.

The process of estimation of feature values is usually conducted for a selected image area which is

known as a region of interests (ROI). There are some advantages of examination of the ROI instead of the whole image. Examples are a decrease of processed image sizes as well as image analysis time. These factors are particularly important in case of on-line diagnostic systems.

An issue of the ROI selection seems to be a simple in case of single images. A specific area of determined size and shape can be indicated manually. In case of image series which are on-line recorded, processed and analysed the ROI selection may turn out more complicated task. The main problem is an image content very often difficult to be predicted. It may change dynamically during the process or object observation. An example is mentioned above the welding process. A welding arc visible in images recorded within visible range of electromagnetic radiation as well as a weld pool present in infrared images may change their shapes and sizes. In this case defined ROIs require particular attention and initial research.

2. IDEA OF A DYNAMIC ROI SELECTION

The main task of the application of vision systems to process diagnostics is quick detection of process abnormalities. Processed images present scenes which consist of several objects. Among them some are crucial to process evaluation, whereas others are unnecessary. The scene is a result of a camera placement and optical set application and is often difficult to be changed. To evaluate the process quickly and effectively the ROI is necessary to be selected. This specific area should be focused on proper scene objects. Apart from removing insignificant object, the approach let us also decrease the image size and the same limit analysis time. The simplest solution is to define the shape, size and localization of the ROI. These parameters can be used for every image of the series. Such approach is correct in case one assure invariability of the process. It means that localization of the observed objects as well as changes of their shapes and sizes can be passed over. The ROI selection appears to be more complicated in case of observation and evaluation of a dynamic process. In the course of such processes the objects visible in the image which carry information on the process state may change their parameters dynamically. Additionally the intensity of these changes is often related to process abnormalities. Extra factors making the ROI selection more difficult are deviations of an observed phenomenon source and camera localization. A typical example is discussed the welding process. In Fig. 1 two images of the welding arc are presented. The images have been recorded within range of visible electromagnetic radiation. Two different courses of the process were observed. The evaluation of the process was achieved on the basis of features estimated for the welding arc area. The size, shape and localization within the ROI (Fig. 1a) were calculated for a single image sequence. It is clearly noticeable that the ROI properly defined for one sequence (Fig. 1a) turned out to be improper for other images (Fig. 1b). In the second case the welding torch was accidentally moved during welded elements assembly. Additionally, significant changes of the arc shape caused by oil on welded surface were observed.

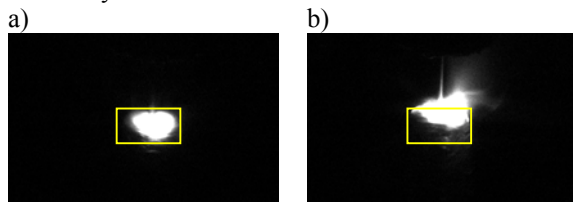


Fig. 1. Examples of properly a) and improperly b) ROI selection

The analysis of the ROI corresponding to Fig. 1b led to incorrect results of the algorithms, thus wrong conclusions on the process abnormalities. In such case a method of the ROI selection is necessary to be especially elaborated. As it was mentioned above,

one assumed that basic parameters of the ROI are its shape, size and localization. One can assume any shape of the ROI. It can results from the shape of the observed object. However, the most often its shape is rectangular since it can be represented as a numeric array and easily processed by computer systems. Regardless of the shape, the ROI size is usually defined by means of two parameters such as width and high of the rectangle within the shape is inscribed. The ROI localization is defined through coordinates of the rectangle mass centre. It appears that to describe the ROI the size and localization of the rectangle mass centre are only necessary to be defined. Taking into account the process dynamics the ROI shape, size and localization change and may be different for each image from the sequence. It is not favourable since the parameters should be recalculated for each image. Moreover, the size of the matrix corresponding to the ROI also changes. The changes of the ROI localization and size may also influence values of the diagnostic signals. Additional interference and step changes may be interpreted by an inference algorithm as state changes. In order to avoid such problems two-stage method of ROI selection was proposed and elaborated. Firstly, so-called working ROI is estimated. It is characterized by the constant size and localization. In the second stage the appropriate shape of the observed object is searched within the working ROI. The search is dynamically conducted. Next, the object is analysed and some additional estimators are calculated.

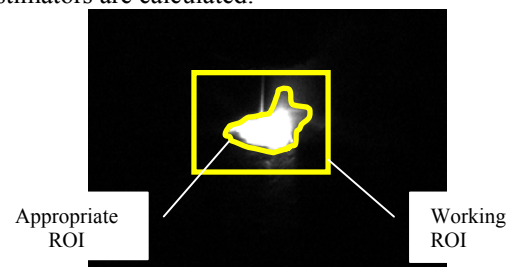


Fig.2. Working and appropriate ROIs

To perform the first stage a sequence of training images is necessary to be prepared and processed. The sequence should include representative cases corresponding to different states that may occur during the welding process. In the second stage the appropriate ROI is estimated for a currently recorded image. It is important that both stages require the application of proper segmentation methods.

The proposed algorithm of ROI definition consists of the following steps:

- Prepare a training sequences of the image.
- Define the shape of the estimated objects for every image of every training sequences; a proper segmentation method should be applied.
- Estimate the height h_0 and width w_0 of the object.
- Find coordinates x_0, y_0 of the object centroid.
- Record the size parameters of the object (h_0, w_0) and coordinates of its centroid x_0, y_0 .

- Estimate mean values x_{om}, y_{om} on the basis of a set of centroid coordinates defined for all images of all sequence.
- Find maximal values h_{omax}, w_{omax} on the basis of a set of size parameters estimated for all images of all sequence.
- Define the rectangular working area of the high h_{omax} and width w_{omax} with the centre localized in x_{om}, y_{om} for every image.
- Define the appropriate ROI within the working ROI; a proper segmentation methods should be applied.

The essential point of the algorithm is to detect correctly the observed object. In case of the majority of images analysed during the welding process, the observed object is the welding arc. Object detection can be performed automatically with the application of one of the image segmentation methods. In the further parts of the paper selected methods of segmentation have been characterized. To estimate the possibility of their application as a part of the elaborated algorithm of ROI selection, some tests have been carried out. Properties of these methods have been also examined to check their application to definition the appropriate ROI.

3. IMAGE SEGMENTATION METHODS

Image segmentation methods have been developed since the beginning of research on image processing and analysis. In the literature numerous of methods of segmentation are described. The image segmentation is called subdivision of an image into its constituent regions (e.g. objects) [10]. Results of the application of different segmentation methods strongly depend on a type of the scene that is represented in the image. For very complex images where the difference between the background and interested object is small, it is very hard to find an appropriate method of image segmentation and in many cases the segmentation is almost impossible or gives results that are far from the one expected [11]. In case of the images with difference between the objects and background is distinct (e.g. bright objects on the dark background) this operation is easier and less complicated. The segmentation is very important in numerous applications (such as monitoring, visual inspection), especially in the cases where further analysis of the extracted object is performed in order to define dimensions, shape or localization of the real object represented in the image.

The algorithms of segmentation of monochromatic images are based usually on two types of features. They are distribution of intensity values in the image: similarity and discontinuity. Therefore one can distinguish a group of methods that divide images into regions which are similar according to some conditions (region-based methods) and a group of methods based on searching an abrupt change in intensity (edge-based methods). Another group of the segmentation

methods is represented by histogram. There are method based on thresholding or multi-thresholding where thresholding could be performed globally (one threshold value for whole image) or as adaptive thresholding (the image is divided into subregions and in each subregion new threshold value is being set).

In this article the authors made an attempt to compare chosen segmentation methods, applied to welding arc images. Procedures have been tested on the series of images of two types: infrared and vision images. Some examples of the application of chosen methods for the vision images of welding arc have been presented below.

3.1. Region-based methods

This group gathers methods based on the analysis of the intensity values of neighbouring pixels. Depending on the algorithm, pixels with the value of intensity that fulfils some conditions - could be included or excluded or split into regions [10]. Differences between methods have been described below.

Region growing - in this approach to segmentation it is obligatory to define initial "seed points" and the algorithm examines neighbouring pixels and determines whether the pixel neighbours should be added to the region. The result of the method is a final region which grows from the seed pixel. Some methods of region growing enable directional growing where pixels with the highest intensity value of a pixel are added to a region firstly [12].

Region merging - an idea of region merging is to verify the value of the features of neighbouring small regions, if the constraints are fulfilled - these regions are merged.

Region splitting - the basic idea of region splitting is to break the image into sets of disjoint regions which are coherent within themselves. The algorithm starts from the assumption that whole image is an area of interests. After verification of assumed similarity constraint, region image is split into sub-areas

Split and merge - split-and-merge segmentation is based on a partition of an image. It is sometimes called quadtree segmentation. This method starts at the root of the tree that represents the whole image. If the region is not sufficiently coherent, region is split into four quadrants and these steps are recursively applied to each new region (the splitting process). If the entire region is coherent (i.e., if all pixels in the region have sufficient similarity), the region is left unmodified. Those regions could be merged as several connected components (the merging process). This process continues recursively until no further splits or merges are possible. Since this algorithm starts with regions larger than single pixels, this method is more efficient in comparison to the merging method [13]. A modification of this method is an application of split and merge algorithm to analyse histogram of the image instead of the image itself [14].

3.2. Edge-based methods

This kind of segmentation is based on searching lines or curves (edges) that represents region boundaries, since there is often abrupt change of intensity at the region boundaries. In order to find edges located horizontally, vertically or skew different masks such as Sobel, Canny, Prewitt, Roberts are usually used [10].

3.3. Clustering method

In this group the most popular algorithm of segmentation is the K-means algorithm. It is an iterative technique that is used to divide an image into K clusters. The K-Means algorithm is called an unsupervised clustering that classifies the input data points into multiple classes based on an inherent distance from each other. The chosen criterion takes a measure of the similarity between data elements of a group and the dissimilarity between different groups for segmenting the images [15]. The difference is typically based on a pixel colour, intensity, texture, and location, or a weighted combination of these factors. K can be selected manually, randomly, or by an heuristic.

3.4. Watershed segmentation

The watershed transformation is applied for the images considered as the gradient magnitude of an analysed image as a topographic surface. The highest gradient magnitude intensities (GMIs) of pixels correspond to watershed lines. These lines represent the region boundaries. Water placed on any pixel enclosed by a common watershed line flows downhill to a common local intensity minimum (LIM) Pixels belonging to this local minimum compose the segment. Let suppose that the grey level range of an image is [0,255]. Algorithm starts from the pixels of intensity values equal to 0. They form the basis for new watersheds. If the pixels with intensity equal to 1 are next to existing watersheds (0-intensity pixels), they are added to these regions. If not, a new region is started for each pixel that is not close to an existing region. This process repeats for each intensity k up to the maximum (255 in presented case) [13].

3.5. Active contours method

This method of segmentation differs from the ones shortly described above. In this method searching of the object in the image is dynamic and based on the model of active contours to detect objects in the image [16]. Assumptions of the method are based on techniques of curve evolution. An algorithm starts from defining "starting region" anywhere in the image and then the algorithm finds the inner contour of the object. Finally it becomes a

boundary of the region found. In Fig. 3 some results has been presented. The active method of segmentation can be very useful in situations, where shape and size of the welding arc is changing very fast. This was the first attempt to apply the active methods to image segmentation and became very promising.

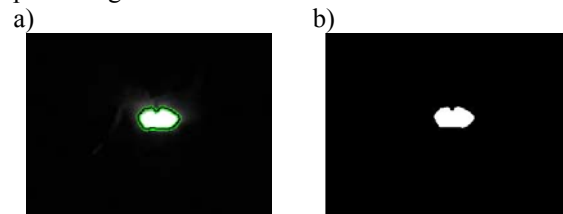


Fig. 3. Example of application of active contour method to vision image of welding arc a) original image with indicated object boundary, b) final effect of segmentation

4. CHARACTERIZATION OF CONSIDERED IMAGES

During the research considered infrared and vision images taken during welding of plates made of steel S235JR (EN 10027-1) with dimensions 300x150x5 mm on the mechanised welding stand for rectilinear MIG/MAG welding equipped in microprocessor controlled welding machine Castolin TotalArc 5000. The edges of the joined plates were bevelled at an angle of $\alpha=60^\circ$ and the offset between them was $b=1,0$ mm. For welding purposes a solid electrode wire with a diameter of 0,2 mm (Castolin CastoMag 45255) and a shield gas M21 (82%Ar+18%CO₂) were used. Nominal welding parameters are presented in Tab. 1.

Infrared and vision images were synchronically acquired with rate 50 fps by use of uncooled infrared camera Infratec VarioCam Head with resolution 640x480px equipped in lens $f=50$ mm and visible light CCD camera ImagingSource DMK21AF04 with resolution 640x480px and lens with focal length $f=25$ mm. Camera's lenses were equipped in a suitable filters suppressing the excess of the electromagnetic radiation and protecting it against splatters generated during welding. Cameras connected to the computers and images acquisition process was controlled by software developed in LabView environment. Series of experiments simulating different faults of welding process were carried out. It permitted to record the collection of sequences of infrared and vision images for 12 different states of welding.

Table 1. Optimal MAG welding parameters

Welding current [A]	Welding voltage [V]	Welding speed [cm/min]	Wire feeding rate [m/min]	Shield gas flow [l/min]	Electrode outlet [mm]
240	25	32	7,4	15	15

Process classified in the following way:

- correct welding process.
- welding with decay of the shielding gas flow.
- welding of the plates with distinct outbreaks of atmospheric corrosion on the welded surfaces.
- welding with use of corroded wire.
- welding of plates with irregularities of the plate edges from side of the weld root.
- welding of plates with oil contamination.
- welding with deviation of current.
- welding of plates with different offset intervals.
- welding with deviation of voltage.
- welding of the plates with improper welding groove geometry.
- welding with deviation of speed.
- welding with use of worn rollers of wire feeder.

Because of the huge number of images acquired during the experiment, results of application of the segmentation methods have been shown only for couple of chosen images.

5. Comparison of usefulness of segmentation methods to sequences of images recorded during welding

To verify the elaborated algorithm of the working and appropriate ROI definition the sequence of the infrared images has been selected. It should be stated that these images are more complicated in comparison to the images recorded within visible range of electromagnetic radiation. The use of these images let us more effectively check different segmentation methods. The image sequence used in the verification stage was recorded during the welding process when decay of the shielding gas was observed. The images presented in the further parts of the paper were recorded during different stages of the process. The images show also process diversity and dynamics. In Fig. 4 selected infrared images have been presented. In Fig. 5 - 10 there are corresponding to them images resulting from the application of the following segmentation methods: Region Growing, Region Merge, Region Split and Merge, K-means Clustering, Otsu Thresholding, Watershed Transformation. The results differ depending on the segmentation method. Considering the further analysis the most important objects of the images are the weld pool and heat affected zone. These objects are fundamental to diagnostic signals estimation. The majority of the tested method let us detect these areas properly in case of the images characterized by significant contrast between searched objects and other areas visible in the images. In case of images distinctly showing the cooling joint some methods presented only one area.

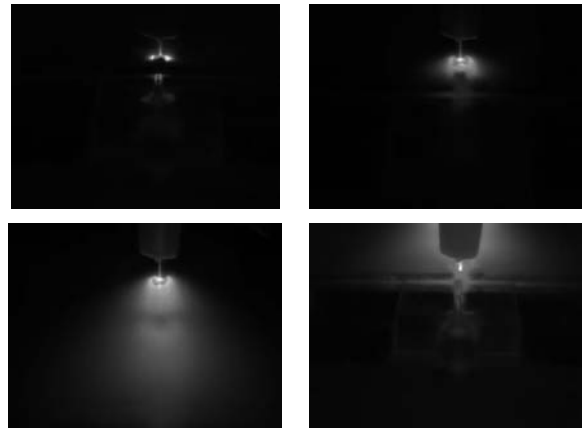


Fig. 4. Selected images of acquired infrared images sequence during welding with decay of the shielding gas flow

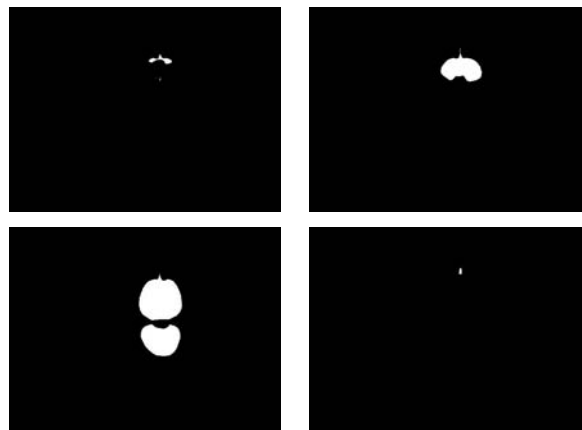


Fig. 5. Results of segmentation of infrared images presented in Fig. 4 by use of Region Growing method

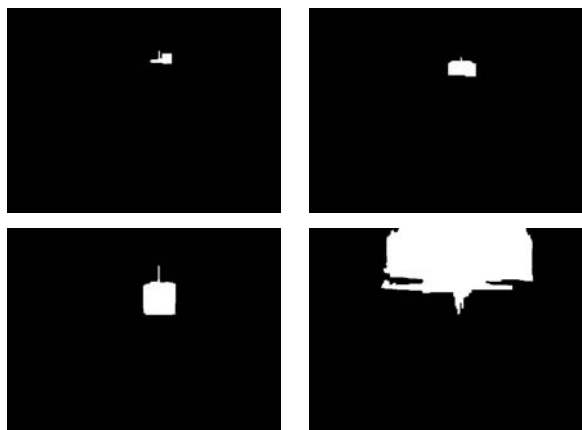


Fig. 6. Results of segmentation of infrared images presented in Fig. 4 by use of Region Merge method

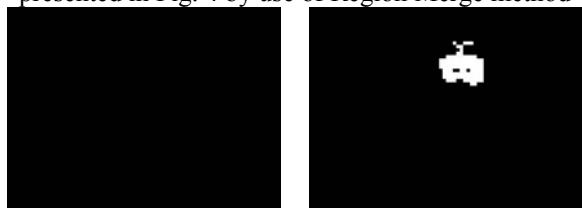




Fig. 7. Results of segmentation of infrared images presented in Fig. 4 by use of Region Split and Merge method

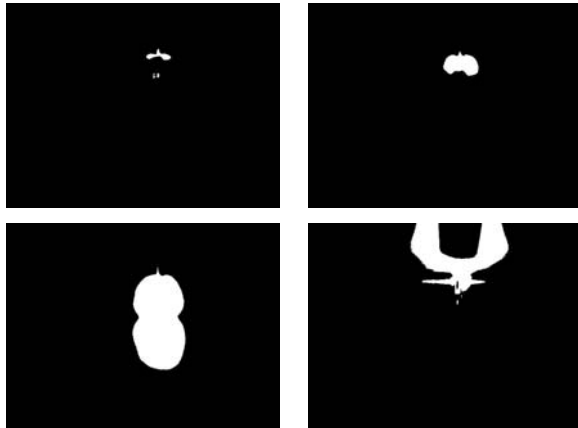


Fig. 8. Results of segmentation of infrared images presented in Fig. 4 by use of K-means Clustering method

The weld pool and heat affected zone were shown together (Fig. 8 and Fig. 9). Results of other methods showed areas of infrared radiation different for the weld pool and arc. Examples are images recorded during decay of the shielding gas were observed (Fig. 6, Fig. 8 and Fig. 9).

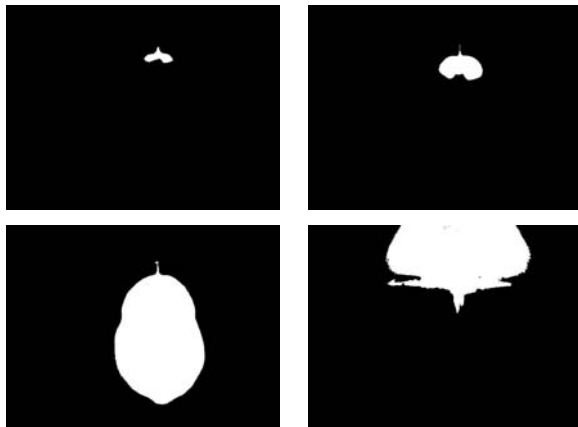


Fig. 9. Results of segmentation of infrared images presented in Fig. 4 by use of Otsu Thresholding method

According to the proposed algorithm the mean values of centroid coordinates and maximal values of width and height of the object resulting from the segmentation have been estimated. These values can be background to the inference on changes of the process state. Mentioned parameters have been

presented in Tab. 2. Exemplary infrared image with the drawn ROIs on the basis of the parameters collected in Tab. 2 were presented in Fig. 11.

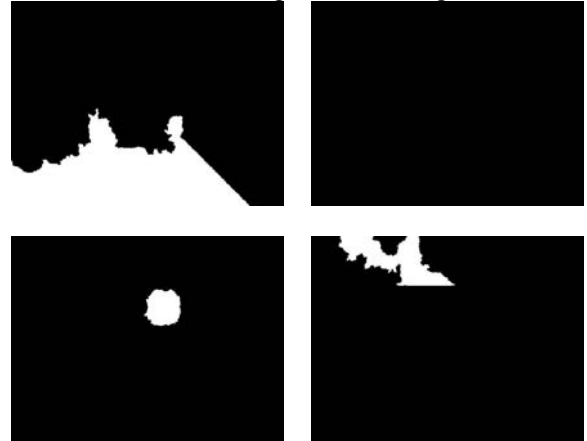


Fig. 10. Results of segmentation of infrared images presented in Fig. 4 by use of Watershed transformation method

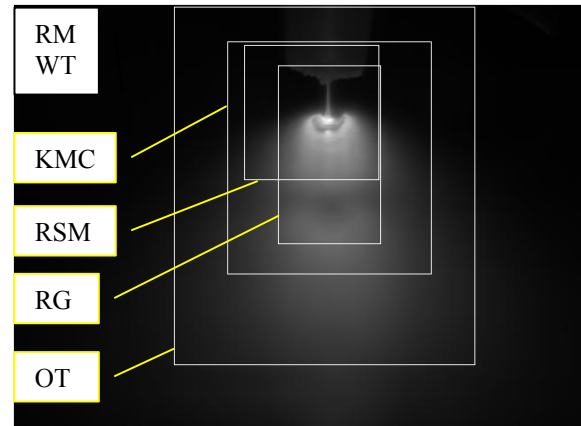


Fig. 11. Exemplary infrared images with drawn ROIs which parameters estimated on the basis of presented algorithm applied different segmentation methods

In Fig. 12 exemplary comparison between the coordinate y_o and high h_o of the objects resulting from the segmentation based on Region Growing and Watershed transformation was presented. In case of the Region Growing values of the parameters (object high and width) increase as an effect of gradually heat up of the welded elements. The course of changes of the object parameters let us also identify the moment when instability of the welding process occurred. In the presented example the instability was triggered off by instability of the shielding gas. In case of the method based on the Watershed transformation there is a significant difference between estimated parameters. It indicates a high sensitivity of the methods.

Table 2. Comparison of working ROI parameters calculated on the basis of infrared image sequence

	Mean X Centroid x_o^m	Mean Y Centroid y_o^m	Max Width w_o^{max}	Max Height h_o^{max}
Region Growing (RG)	357	170	116	201
Region Merge (RM)	357	157	640	480
Region Split and Merge (RSM)	337	123	152	152
K-means Clustering (KMC)	357	174	230	262
Otsu Thresholding (OT)	351	205	339	403
Watershed transformation (WT)	187	122	640	480

The approach is especially sensitive to temperature changes dynamics what is reflected in pixel values in infrared images. Considering the Watershed method and resulting images it is clearly visible that the moment of the instability occurrence is also difficult to identify. On the basis of analysis of mean values of coordinates of the mass centre (Tab. 2) one can conclude that except of the Watershed transformation all the methods tested let us identify horizontal localization x_o^m of the working ROI. The localization was within the range corresponding to the centre of the image. In case of the vertical coordinate y_o^m better results were achieved with use of the Region Split and Merge as well as Watershed transformation. These results allowed us to localize the centre of the working ROI close to centre coordinates of the weld pool. The rest of the methods gave resulting objects larger then one expected. It was an effect of joining several hot areas visible in the image.

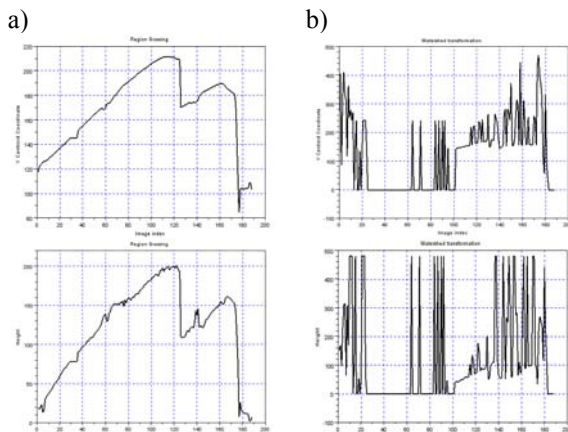


Fig. 12. Comparison of values of Y Centroid coordinate and height of objects being result of segmentation using Region Growing method a) and Watershead transformation b)

The verification of the segmentation methods was also performed to determine their usefulness as elements of diagnostic procedures. In this case the methods can be used to estimate the appropriate ROIs. The estimated objects resulting from the application of different segmentation methods were characterized among others parameters by an area. Fig. 13 presents the comparison of changes of values of the object area. The objects were detected with use of the segmentation based on Region Growing and Otsu thresholding. The segmentation based on

the Otsu thresholding made it impossible to exactly detect the moment of the process abnormality (decay of the shielding gas). It was detected by means of the method based on the Region Growing.

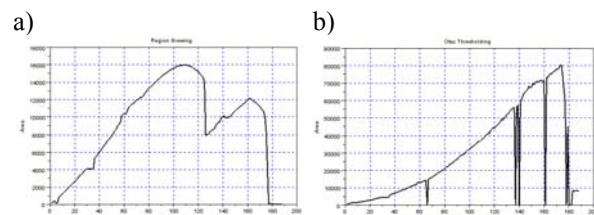


Fig. 13. Comparison of diagnostic signal of area values of objects being result of segmentation using Region Growing method a) and Otsu thresholding method b)

6. SUMMARY

The results shown in the paper let us conclude that in case of estimation of the infrared image sequence during the welding process each of the tested segmentation methods gave different results. It should be stated that some of these results were very unfavourable taking into account the algorithm of the appropriate ROI definition. The conclusion based on a subjective estimation of the obtained result seems to be that the most beneficial approach is the Region growing. The method is only slightly sensitive to rapid changes of the image contents. The next conclusion of the verification research is the most promising solution is to apply not only one but several methods of segmentation. It will let us optimally select the parameters of the working ROI. A very important factor of the proposed algorithm is that effective detection of the objects in the analyzed images corresponds to a proper choice of the segmentation method. The choice can be performed by means of optimization. It is the further step of the research conducted by the authors.

However it is necessary to stress that the images selected to verification were very complex. Despite of the variety of the obtained results and in some cases poor results it is worth to underline that one was able to verify the proposed algorithm and simultaneously estimate usefulness segmentation methods. Considering the part of the verification with use of images of the welding arc recorded within range of visible radiation which was not shown in the paper it is necessary to remark that the contrast between the objects in images was more distinct. In this case the majority of the tested

segmentation methods gave correct and acceptable results. An exception was the Watershed approach. Generally, all the achieved results were better than in case of infrared images.

Summarizing, one can state that to define the appropriate ROI the segmentation methods based on the active searching for the object contour seems to be the best solution. At present, the application of these approaches to analysis of images recorded in visible range of electromagnetic radiation is examined by the authors.

REFERENCES

- [1] Rockinger, O.: *Image Sequence Fusion Using a Shift Invariant Wavelet Transform*. Proceedings of the International Conference on Image Processing, vol.3, pp. 288-291, 1997.
- [2] Sadjadi F.: *Comparative Image Fusion Analysis*, Proc. of the 2005 IEEE Computer Society Conference on Computer Vision and Pattern Recognition (CVPR'05) - Workshops, Vol. 03, p.8, 2005.
- [3] Information on <http://www.ishotimaging.com/weldi-home.html>, Weld-i Series, Weld Monitoring Inspection Systems.
- [4] Camilleri D., Gray T., and Comlekci T.: *Use of Thermography to Calibrate Fusion Welding Procedures in Virtual Fabrication Applications*. Proc. of Information 2004 Conference, vol. 5 pp. 121 -131, 2004.
- [5] Bzymek A., Fidali M., Jamrozik W., Timofiejczuk A.: *Diagnostic vision system for welded joint and welding process assessment*. Maintenance Problems, 4/2008, pp. 39-52.
- [6] Jamrozik W.: *Method of diagnosis of industrial processes with use of data fusion*, PhD Thesis, Gliwice, 2012.
- [7] Fidali M., Jamrozik W.: *The processing of fused infrared and vision images of a welding arc for fault detection*, Proceedings of 11th Quantitative InfraRed Thermography, 11-14 June 2012, Naples, Italy.
- [8] Bzymek A., Timofiejczuk A.: *Estimation of welding process stability based on image analysis and recognition*, Diagnostyka 4(52) / 2009, pp 41-44.
- [9] Zhang, Y. M., Kovacevic, R., Ruan, S.: *Sensing and Control of Weld Pool Geometry for Automated GTA Welding*, Transactions of the ASME, 1995, vol. 117, pp.210-222.
- [10] Gonzales R. C., Woods R. E., Eddins S. L.: *Digital image processing using Matlab*, Pearson, Prentice Hall, London, 2004.
- [11] Zuva T., Olugbara O. O., Ojo S. O. and Ngwira S. M.: *Image Segmentation, Available Techniques, Developments and Open Issues*, Canadian Journal on Image Processing and Computer Vision Vol. 2, No. 3, March 2011.
- [12] Hojjatoleslami, S. A., Kittler, J.: *Region growing: a new approach*, *Image Processing, IEEE Transactions on*, vol.7, no.7, pp.1079-1084, Jul 1998 doi: 10.1109/83.701170.
- [13] Information on http://homepages.inf.ed.ac.uk/rbf/CVonline/LOCAL_COPIES/MORSE/region.pdf.
- [14] Reyad Y. A., El-Zaar A., Mathkour H., Al-Zuair M.: *Image Thresholding Using Split and Merge Techniques with Log-Normal Distribution*, Canadian Journal on Image Processing and Computer Vision, Vol. 1, No. 3, July 2010.
- [15] Tatiraju S., Mehta A.: *Image Segmentation using k-means clustering*, EM and Normalized Cuts, doi=10.1.1.187.6371.
- [16] Chan, T. F., Vese L. A.: *Active contours without edges*, *IEEE Transactions on Image Processing* vol.10, no.2, pp.266-277, Feb 2001, doi: 10.1109/83.902291.



Marek FIDALI, PhD, assistant professor at Institute of Fundamentals of Machinery Design. Main area of research: technical diagnostics, infrared thermography, modal analysis, signal and image processing



Wojciech JAMROZIK, PhD, assistant professor at Institute of Fundamentals of Machinery Design. His primary fields of interest are methods of technical diagnostics, applications of thermovision, image processing and analysis, as well as fusion of uncertain and conflicting information.



Anna BZYMEK, PhD., assistant professor in Institute of Fundamentals of Machinery Design. The main area of research: methods of image processing, analysis and recognition, vision systems in technical diagnostics, signal processing.



Anna TIMOFIEJCZUK, professor in Institute of Fundamentals of Machinery Design. Main area of research: time-frequency signal analysis, diagnostic inference, image processing, analysis and recognition.

ANALYSIS OF COMPARTMENTS FLOODING TIME AND METACENTRIC HEIGHT AFTER HULL DAMAGE

Waldemar MIRONIUK

Katedra Eksploatacji Jednostki Pływającej Akademii Marynarki Wojennej
Wydział Nawigacji i Uzbrojenia Okrętowego ul. Śmidowicza 69, 81-103 Gdynia,
tel. (58) 626 27 24, e-mail w.mironiuk@amw.gdynia.pl

Summary

The paper presents research on damage stability and unsinkability. The result of it is a valuable source of knowledge of behaving a ship while flooding its compartments. In the paper, a short description of accidents and damages of Polish warships taking place in 1985-2004 is presented. The time when compartments are flooded (t_f) and stability parameters are one of the key elements which have influence on a rescue action. The knowledge of the time mentioned and a metacentric height (GM) are very important for a commanding officer making decisions while damage of the ship. To provide the information about the time t_f a new method was designed. Firstly, volume of damaged compartments was calculated. To estimate a real quantity of the water, the permeability of flooding compartment μ is used. Permeability of the main engine and auxiliary power plant was estimated on the basis of preliminary research presented in the paper. Its value, shown in the article, is dependent on the water level inside compartments. The metacentric height (GM), while flooding process of damage compartments, was calculated in the next step. On the basis of the built computer program, a simulation of the flooding process and value of metacentric height (GM) of the damaged main engine and auxiliary power plant ship's type 888 was shown. The developed method was tested experimentally and results of the tests are presented in the paper. The results of the experiments can be a base to define general rules to make proper decisions during the process of damage control.

Keywords: damage stability, survivability, flooding time of compartment.

ANALIZA CZASU ZATOPIENIA PRZEDZIAŁU OKRĘTOWEGO I WYSOKOŚCI METACENTRYCZNEJ PO USZKODZENIU KADŁUBA

Streszczenie

W artykule zaprezentowano wyniki badań stateczności awaryjnej i niezatapialności okrętu stanowiące źródło wiedzy o zachowaniu się okrętu podczas zatapiania jego przedziałów. Przedstawiono krótką charakterystykę wypadków i awarii okrętowych w latach 1985 – 2004. Podstawowymi elementami sygnalizowanymi w artykule są czas zatopienia przedziału okrętowego i parametry stateczności mające wpływ na bezpieczeństwo okrętu i prowadzenie akcji ratowniczej. Znajomość wymienionych parametrów jest bardzo istotna dla oficera odpowiedzialnego za akcję ratowniczą i niezbędna do wypracowania decyzji o sposobie jej prowadzenia. Do określenia czasu zatopienia przedziału okrętowego opracowano nową metodę. W pierwszej kolejności określono objętość uszkodzonego przedziału. W celu oceny rzeczywistej ilości wody napływającej do uszkodzonego przedziału wykorzystano współczynnik zatapialności przedziału, którego wartość dla siłowni głównej i pomocniczej określono dla rosnącego poziomu wody w przedziale. Następnie na podstawie zbudowanego programu komputerowego obliczono i przedstawiono graficznie wyniki wartości wysokości metacentrycznej oraz symulację zatapiania przedziałów siłowni głównej i pomocniczej. Otrzymane wyniki badań eksperymentalnych mogą być podstawą do opracowania metod walki z awariami w ramach obrony przeciwawaryjnej okrętu.

Słowa kluczowe: stateczność awaryjna, niezatapialność, czas zatopienia przedziału.

INTRODUCTION

Even highly organized fleets struggle with accidents and technical breakdowns which cannot be completely eliminated. The breakdowns can be classified based on their causes. The basic causes of the breakdowns are: warfare, defects of materials and defects within the production process,

constructional defects, technological defects in the process of renovation, material's wear and tear, not meeting the requirements in operating and servicing an equipment, not taking security measures while storing dangerous cargoes, e.g. explosive materials, petroleum products and other chemical components of serious fire hazard, environmental hazards.

A partial or total loss in functionality of mechanisms and installations can occur both during warfare and during daily operating a ship.

Failures caused by navigational errors or wrong maneuvering represent a group of ship accidents and breakdowns which can lead to dangerous loss of buoyancy of a ship due to flooding its compartments.

The statistical data prepared by the Polish Navy Commission of Warship Accidents and breakdowns reveal 156 warship accidents and breakdowns between 1985 and 2004. The data mentioned are presented in figure 1 [3].

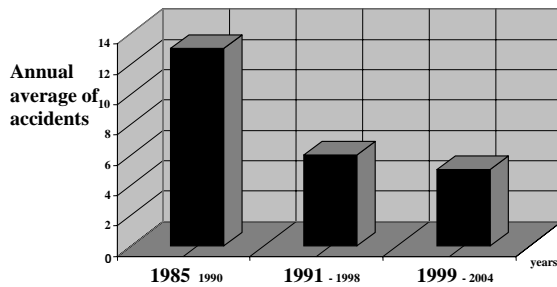


Fig. 1. The overall graph of accidents and breakdowns between 1985- 2004

In a situation of a breakdown crew activities deciding about ability of a warship to fight should be directed to take a proper actions during the process of damage control and to protect stability and maneuverability of the ship.

Exercises within the boundaries of the process of damage control, apart from construction solutions, increase the safety of both the ship and the crew. Training is carried out in well prepared training centers which are situated in the United Kingdom, Germany, Netherlands and Pakistan. The centers are equipped with ship models designed for simulating failure states which most frequently occur while operating a ship. The same models were also used in the experiments reported in the paper. One of the goals of the experiments mentioned was to determine the following parameters: t_f and GM for the ship type 888. This warship is used for training of Polish seafarers taking part in numerous international cruises. Main dimensions of the ship are: length L-72 m, breadth B-12 m, draught T-4,2 m and displacement 1750 t. Photo of the ship is shown in Figure 2.

Presently, only simplified methods to calculate the parameters above mentioned exist. The method presented in the paper has a distinctive difference compared to the existing, similar methods discussed in some publications. The worked out method considers the permeability value dependent on the water level inside the damaged compartment. Due to this, we can estimate more accurately the quantity of water in the compartment and finally more accurately the flooding time of the damaged

compartment. The aim of presented method is to provide experimental validation.



Fig.2. Ship type 888

The information about t_f and stability parameters is very important for a commanding officer. It enables him to make a proper decision during the process of damage control. The officer, based on the information should determine the point in time, when further fighting for survivability is senseless and when all effort should be directed to save the crew and documents.

COMPUTING THE VOLUME OF DAMAGED COMPARTMENTS

The volume and shape of damaged compartments is necessary to present a simulation process of flooding compartments. The lines plan of the ship's hull is used to compute the theoretical volume. Moreover, the plan was also used to have sections extracted at the place of ribs number 35, 40, 45, 50, where we can find the damaged compartment. The sections are shown in Figure 3 [4, 6].

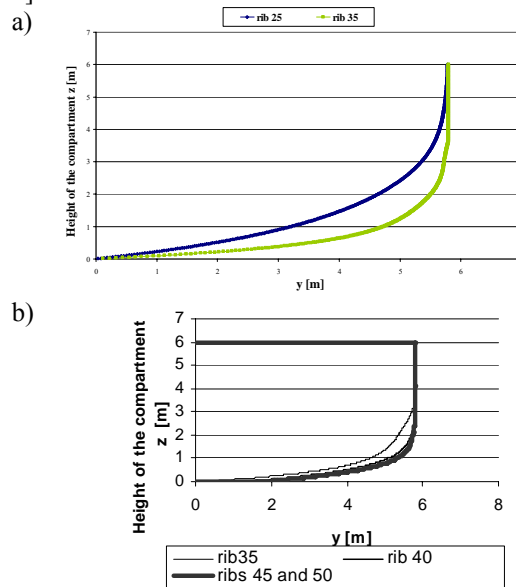
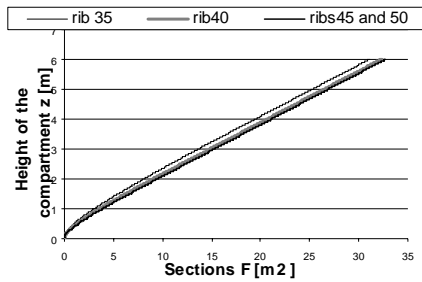


Fig. 3. Sections of: a) auxiliary power plant, b) engine room

The area of the sections was calculated to estimate the accurate volume of the damaged

compartment. Integral curves of sectional areas, obtained in this way, are presented in graphic form as a multinomial degree 7 in Figure 4.

a)



b)

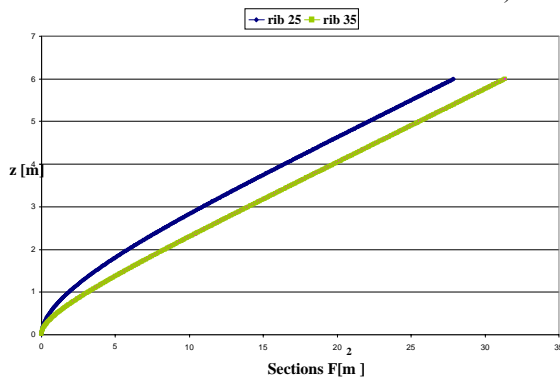


Fig. 4. Integral curve sectional areas: a) engine room, b) auxiliary power plant

Using section areas and a distance between them, the theoretical compartment volume can be calculated, by the formula [1,2]:

$$v_t = \sum \frac{(F_i + F_{i+1}) \cdot l_w}{2} \quad (1)$$

where l_w = the distance between sectional areas

F_i, F_{i+1} = section areas.

THE PERMEABILITY CALCULATION

The volume of the empty compartment was calculated with the aid of the computer program. The real quantity of the water, flooding the compartment, is less than the theoretical volume of the compartment due to the volume of all mechanisms and devices inside the compartment. Usually, to calculate a real quantity of the water, the permeability of flooding compartment μ is used. Permeability is used in ship survivability and damaged stability calculations. In this case, the permeability of a space is a coefficient from 0 to 1. The permeability of a space is the percentage of volume of the space which may be occupied by seawater if the space is flooded. The remaining volume (not filled with seawater) being occupied by machinery, cargo, accommodation spaces, etc. The values of permeability for compartment is calculated by the formula [1]:

$$\mu = \frac{v}{v_t} \quad (2)$$

where v_t = theoretical compartment volume;

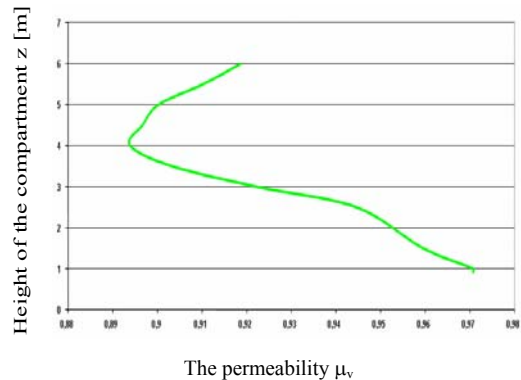
v = real quantity of the water inside the compartment.

The numerical value of the permeability depends on both, a kind and destination of damaged compartment. The permeability of the compartment μ , which is announced in the SOLAS Convention, is usually used to calculate the real volume of the compartment. Typical values from the SOLAS Convention are:

- 0.95 for voids (empty spaces), tanks, and living spaces;
- 0.85 for machinery spaces;
- 0.60 for spaces allocated to stores.

This implies that for damaged stability calculation purposes, machinery spaces are only 15% full with machinery by volume (100% - 85% = 15%). In preliminary research presented in the paper, permeability of the main engine room and the auxiliary power plant was estimated. Its value depends on the height of the water inside the compartment. The graph of the permeability is shown in Figure 5 [4, 6].

a)



b)

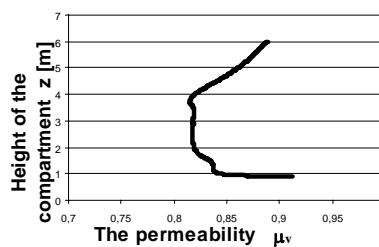


Fig. 5. Graph of permeability: a) the auxiliary power plant, b) the engine room permeability μ_v

The average value of the permeability for chosen compartments, obtained as a result of experiments, is comparable with the value of the SOLAS Convention and equals 0,84.

THE MODEL OF SIMULATION FOR DAMAGED COMPARTMENTS

The simulation models of the auxiliary power plant and the engine room, equipped with all main

mechanisms and devices, were made in the next part of the research. The view of the compartments being flooded and the position of the ship are shown in Figure 6 [4, 6].

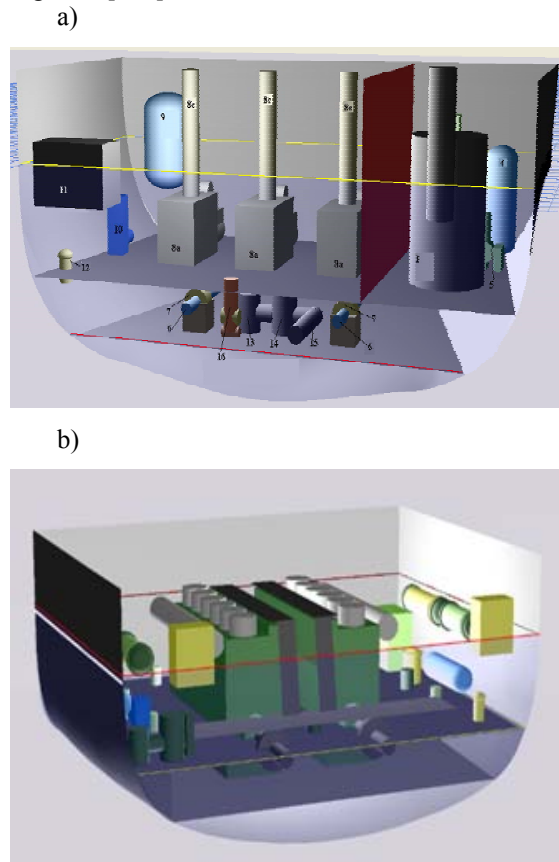


Fig. 6. Compartments being flooded: a) auxiliary power plant, b) engine room

THE ANALYSIS OF THE INFLUENCE OF DAMAGE PARAMETERS ON THE TIME T_f FOR THE COMPARTMENT SHIP TYPE 888

The experimental research on t_f for engine room ship type 888 was carried out for different parameters of damages. In the research, the place and the dimensions of damage were taken into consideration.

During the numerical simulation t_f of damaged compartment, the variability volumetric flow rate of the water flowing to the compartment was taken into account. This parameter depends on both the depth of the hole and water level inside the compartment. Assuming, that the flooding process is a hydrostatic, the movement of the vessel was not taken into consideration and the ship is without a heel and trim. Only the draft of the ship caused by the adoption of water to the damaged compartment was taken into account.

In the first stage of the research, t_f for the engine room was estimated. The calculations of t_f were made for the following example conditions: ship's draught $T=4$ m, the dimension of damages $R=0,03$ m, $R=0,05$ m, $R=0,1$ m and $R=0,2$ m (R - denotes

radius). The holes were placed from 0,1m to 3,0 m below the surface of the sea. The results of the research are shown in Figure 7.

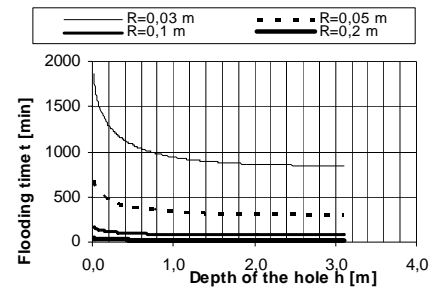


Fig. 7. Flooding time t_f for the engine room

Figure 7 presents that t_f for the compartment with dimension of damage $R=0,2$ m, placed 3 m below the surface of the sea, equals 3,4 minutes. This time is too short to seal the damage. Consequently, further activities of crew should be directed to protect spreading the water covering interior of the ship and to strengthen the construction of the watertight bulkhead.

THE METACENTRIC HEIGHT CALCULATION

The next part of the research was devoted to estimate a metacentric height while flooding a damaged compartment. To calculate this parameter the added mass method was used. The result of calculations is shown in Figure 8.

To calculate the metacentric height the free surface effect was taken into consideration. Figure 9 implies that in the early stage of flooding the compartment, the metacentric height $G_{up}Mu$, is less than GM . In the later stages, $G_{up}Mu$ increases and improves stability of a ship. This situation takes place due to adding a mass in the lower part of the ship.

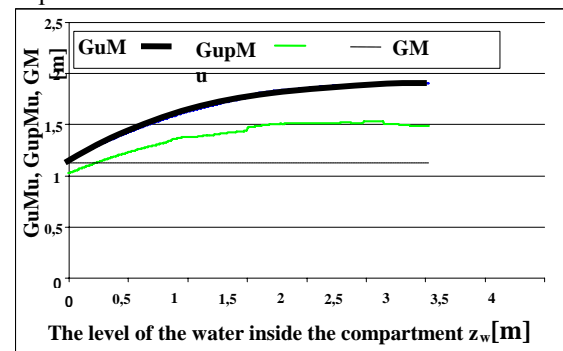


Fig. 8. Metacentric height (GM - initial metacentric height (before damage); $G_{u}Mu$ - metacentric height while flooding engine room; $G_{up}Mu$ - metacentric height while flooding engine room with free surface.

CONCLUSIONS

The knowledge of the time t_f and metacentric height allows a commanding officer to make decisions while fighting for survivability of the ship.

The method of determining the permeability presented in the paper enables us to make calculating the time t_f more accurate.

The modified method can be used to calculate the time t_f for ship type 888 with different types of hull damages. The method can be adopted for some other type of warships.

Computer visualisation of flooding process damaged compartments and ship position can be a base to define general rules to make proper decisions during the process of damage control.



kmdr dr. inż. **Waldemar MIRONIUK**
Akademia Marynarki Wojennej,
Wydział Nawigacji i Uzbrojenia.

REFERENCES

- [1] Derett D. R., *Ship stability for Masters and Mates*. BH. Oxford,UK,2003.
- [2] Dudziak J., *Teoria okrętu*, WM, Gdańsk, 2006.
- [3] Korczewski Z., Pawłędzio A., Wróbel R., *Analiza ilościowa wypadków i awarii na okrętach Marynarki Wojennej RP w latach 1985-2004*, Przegląd Morski nr 2. Gdynia, 2005.
- [4] Kowalke O., *Komputerowa symulacja zatapiania przedziału siłowni okrętu typu 888*, AMW, Gdynia, 2006.
- [5] Mironiuk W., *Preliminary research on stability of warship models*, COPPE Brazil, Rio de Janeiro, 2006.
- [6] Tarnowski K., *Badania modelowe stateczności awaryjnej okrętu typu 888 po zatopieniu siłowni pomocniczej*, AMW, Gdynia, 2008.

DYNWIR S-70 PROGRAM FOR MODAL ANALYSIS OF MULTISUPPORTED AND MULTIMASS ROTORS

Łukasz BREŃKACZ, Paweł BAGIŃSKI, Małgorzata BOGULICZ

Institute of Fluid-Flow Machinery – Polish Academy of Sciences, Rotor Dynamics and Slide Bearings Department, Fiszerza 14 street, 80-231 Gdansk, email: lbrenkacz@imp.gda.pl

Summary

The article provides a brief description of the program Dynwir-S-70 (currently being developed in the Rotor Dynamics and Slide Bearings Department in the Institute of Fluid-Flow Machinery Polish Academy of Sciences in Gdansk) which is a program for analysis of multi-supported and multi-mass rotors. Used algorithms and the construction of mass and stiffness matrix were presented. Damping matrix structure based on Rayleigh damping was presented. The article also shows the influence of alpha and beta factors on form and frequency of proper vibrations of rotors. Results of the author's program were compared with the commercial program Madyn 2000.

Keywords: modal analysis, rotor dynamics.

DYNWIR S-70 PROGRAM DO ANALIZY MODALNEJ WIELOPODPOROWYCH I WIELOMASOWYCH WIRNIKÓW

Streszczenie

W artykule zamieszczono krótki opis programu Dynwir-S-70 (rozwijanego w Zakładzie Dynamiki Wirników i Łożysk Ślizgowych IMP PAN w Gdańsku) który jest programem do analizy wielopodporowych i wielomasowych wirników. Przedstawiono stosowane algorytmy oraz budowę macierzy mas i sztywności. Przedstawiono budowę macierzy tłumienia w oparciu o tłumienie Rayleigha. W artykule pokazano również wpływ współczynników alfa i beta na częstotliwości i postaci drgań własnych wirników. Wyniki programu porównano z wynikami komercyjnego programu Madyn 2000.

Słowa kluczowe: analiza modalna, dynamika wirników.

1. INTRODUCTION

There are many programs for modal analysis, why is being developer another one? The answer to this question is simple. Modal analysis programs usually do not allow the analysis of power machinery rotors supported on sliding bearings – and such is the purpose of the development program Dynwir-S-70. This article applies to Dynwir-S-70 developed in the Institute of Fluid-Flow Machinery Polish Academy of Sciences in Gdansk in the Department of Rotors Dynamics and Slide Bearings. This program is part of the system MESWIR. Dynwir-S-70 is used for the analysis of free bending, torsional and longitudinal free vibrations of multi-mass and multi-supported rotors [1]. The program calculates all the values of the vibrations and the corresponding values of damping coefficients.

There are commercial programs used for modal analysis of rotating machinery - such as program Madyn 2000. Work is underway to upgrade Dynwir-S-70 for nonlinear elements in the modal analysis. Madyn 2000 was used to verify the Dynwir-S-70 in some cases.

2. DESCRIPTION OF THE PROGRAM

One of the main criteria used in the design of mechanical systems are dynamic properties of the structure. They have a direct impact on the vibrations, emitted noise, fatigue, controllability and stability of the structure [2]. One of the basic mechanical properties of the rotating machines are natural frequencies and mode shapes.

Free vibrations are the vibrations of the system, on which - after the initial excitation – do not act any forces. The frequencies with which the system vibrates we call natural frequencies, because they characterize the mechanical properties of the system.

There are many ways to solve natural frequency problem and the literature on this issue is very extensive. It is impossible to provide the best method, because whether it is depended from type of problem and computer capabilities. Types of problems are distinguished by specific cases of proper vibration equations of motion. Thus, we have the following types of equations [3]:

a) Undamped free vibration

$$M\ddot{x} + Kx = 0 \quad (1)$$

b) Damped free vibration

$$M\ddot{x} + C\dot{x} + Kx = 0 \quad (2)$$

where:

M – inertia matrix,

C – damping matrix,

K – stiffness matrix,

x – generalized displacement vector.

Methods of solving of natural frequency problems are divided into: transformational and iterative. Iterative methods are: the method of Jacobi, Givens, Householder, LR and QR. In Dynwir-S-70 program we use connection of QR and Householder methods, and so the program is based on the iterative methods. In Dynwir S-70 matrix from which they are calculated eigenvalues (3) is a unsymmetric matrix. The exact process is to reduce the computational matrix using Householder transformation to the almost upper triangular matrix (Hessenberg form), after that eigenvalues are calculated by QR algorithm. Transformation time to Hessenberg form takes the most time in the whole process of calculating the eigenvalues

It is worth noting that for a system with n degrees of freedom, the procedure used in Dynwir-S-70, solves the eigenvalue problem for the matrix $AP = 2n \times 2n$ (3), which gives 2n eigenvalues and 2n eigenvectors.

$$AP = \begin{bmatrix} -MC^{-1} & -M^{-1}K \\ I & 0 \end{bmatrix} \quad (3)$$

where:

I- identity matrix,

0- zero matrix.

The resulting eigenvalues in the considered issue are complex or real numbers. Imaginary parts of the complex numbers represent the natural frequencies of the system expressed in [rad / s], whereas the real parts correspond to damping [-] corresponding to the frequency. Eigenvectors corresponding to complex eigenvalues have complex coordinates and are treated as forms of vibrations occurring at particular frequencies. It is assumed that the eigenvalues which are real numbers do not correspond to any natural frequencies. In the output files eigenvalues in which the absolute value of the imaginary part is less than 1 are skipped (when natural frequency is lower than 1 [rad/s]).

3. BASE MODEL

Calculations in Dynwir-S-70 was presented at a simple example: rotor supported on two supports at each end of the shaft are bearings (fig. 1).

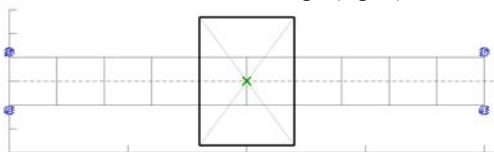


Fig. 1. Construction of the base model. At the ends of the rotor are two slide bearing supports.

The following are the characteristics of the system:

- the length of the rotor: 20 [mm],
- the diameter of the rotor shaft: 20 [mm],
- the diameter of the rotor blade: 50 [mm],
- the thickness of the rotor blade: 40 [mm],
- the bearings stiffness: $5 \cdot 10^7$ [N/m],
- the bearings damping: $5 \cdot 10^5$ [N s/m]

4. NUMERICAL MODEL BUILT USING BERNOULLIE-EULERA AND TIMOSHENKO BEAMS

The following are the results of a test of the analysis of the base model (fig. 1). This model has been discredited using two types of beams (fig. 2). The first type is a Bernoulli-Euler beam, the second type is a Timoshenko beam. The difference between them lies in the fact that, in the numerical model constructed with the Bernoulli-Euler beam are taken into account the bending, compressing, extension, and torsion stresses, built in the model of Timoshenko beams are also taken into account shear stresses.

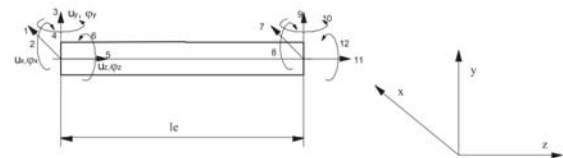


Fig. 2. Beam finite element with two nodes and 12 degrees of freedom [4].

The following indices of directions were determined:

- 1 – x-axis displacement – U_x
- 2 – rotation about the x-axis – φ_x
- 3 – y-axis displacement – U_y
- 4 – rotation about the y-axis – φ_y
- 5 – z-axis displacement (longitudinal vibrations) – U_z
- 6 – rotation about the z-axis (torsional vibrations) – φ_z

Vibration forms described in this article as the first and second, third and fourth, and the next ones are like a pair of similar nature to each other. They are inclined at different angles in space (Fig. 3).

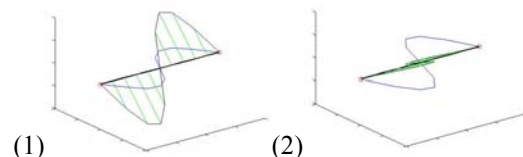


Fig. 3. The difference between the third (1) and fourth (2) form of vibrations in the analyzed cases is the different position in the space.

Table 1 shows the natural frequencies and corresponding damping coefficients for the basic model built using the Timoshenko beam. Six consecutive natural forms of vibrations were

indicated in parentheses. They are shown in Figure 4.

Tab. 1. The first eight natural frequencies and corresponding damping coefficients for the basic model with coefficients $\alpha=3,0$; $\beta=0,000005$

	Timoshenko beam	
	$\alpha=3,0$; $\beta=0,000005$	
	frequency[Hz]	damping [-]
1	568,51 (1)	-38,09
2	568,51 (2)	-38,09
3	2929,75 (3)	-864,74
4	2929,75 (4)	-864,74
5	6259,80 (5)	-3943,53
6	6259,80 (6)	-3943,53
7	7281,64	-5330,29
8	7281,64	-5330,29

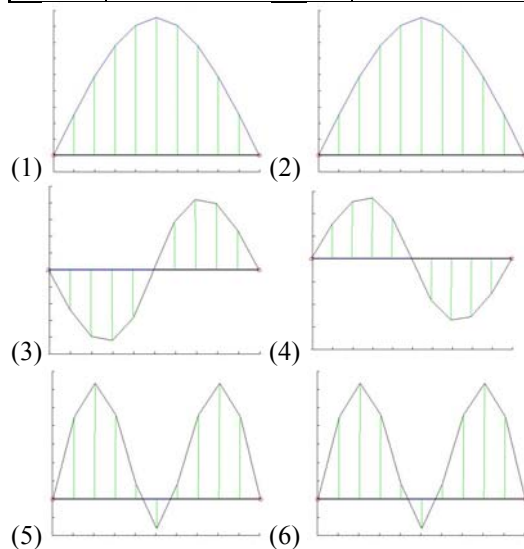


Fig. 4. Form of vibrations for the base model built using Timoshenko beam. The frequencies of these vibrations are given in the Table 1.

Table 2 shows the natural frequencies and corresponding damping coefficients for the base model built using the Euler-Bernoulli beam. Six consecutive natural forms of vibrations were indicated in parentheses. They are shown in Figure 5.

In the model constructed from Euler-Bernoulli beam at some frequencies (tab. 2. position 3 i 4) appear the forms of vibrations, which, should not be disclosed in the real object due to the high damping. The differences between the results of the model built from the Bernoulli-Euler beam and Timoshenko are small. The difference between the frequencies of the first four forms of vibrations is about 1%. The difference between the frequencies of fifth and sixth eigenvector is about 8%. Model adopted for further analysis (after verification of the results with the program Madyn 2000) was a model built with Timoshenko beam (taking into account the shear stresses).

Tab. 2. The first eight natural frequencies and corresponding damping coefficients for the basic model with coefficients $\alpha=3,0$; $\beta=0,000005$

	Bernoulli-Euler beam	
	$\alpha=3,0$; $\beta=0,000005$	
	frequency [Hz]	damping [-]
1	574,14 (1)	-38,84
2	574,14 (2)	-38,84
3	1162,08	-399598,49
4	1162,08	-399598,49
5	2966,76 (3)	-886,51
6	2966,76 (4)	-886,51
7	6808,11 (5)	-4673,91
8	6808,11 (6)	-4673,91

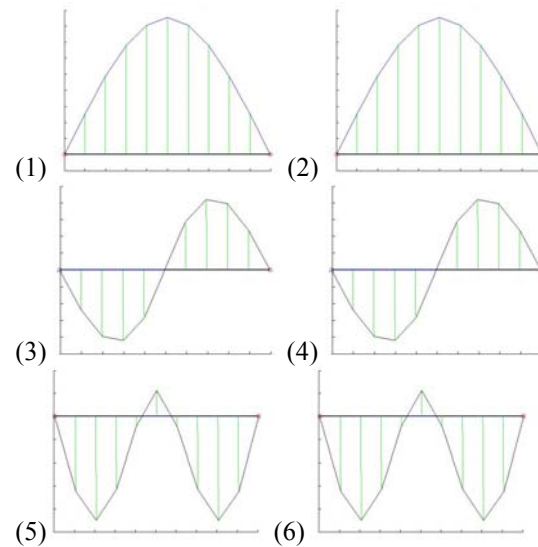


Fig. 5. Form of vibrations for the base model built using Bernoulli-Euler beam. The frequencies of these vibrations are given in the Table 2.

5. RAYLEIGH DAMPING

Damping material has been set by the adoption of proportional coefficients α and β (Rayleigh damping). For such a model of damping the damping matrix (C) of the system is created by the linear combination of an inertia matrix [M] and stiffness matrix [K] that is :

$$[C]=\alpha [M]+\beta [K] \quad (4)$$

Assuming constant damping coefficient ζ understood as the ratio between the damping and critical damping in the case of steel $\zeta=0.01$ and using the relationship (5) [5]:

$$\zeta=\frac{\alpha}{w_{kr}}+\frac{\beta\omega_{kr}}{2} \quad (5)$$

and then analyzing various values (for some natural forms of vibrations) coefficients α and β were obtained namely $\alpha=3$ and $\beta=0,000005$.

Table 3 shows the process of building mass and stiffness matrix. Based on those matrices, the

damping matrix is constructed. After the construction of the damping matrix some elements are added into mass, stiffness and damping matrix.

Tab. 3. Construction of the stiffness, inertia and damping matrix and then supplement these with additional elements.

The construction of the inertia of the shaft matrix [M]
The construction of the stiffness of the shaft matrix [K]
The construction of the damping matrix $C = \alpha [M] + \beta [K]$
Supplementing the inertia matrix [M] among others in parts of inertia associated with disks
Supplementing the stiffness matrix [K] including stiffness parts associated with the foundation, external seals and dampers
Supplementing the damping matrix [C] among others in damping parts associated with the torsion vibration dampers, gyroscopic damping, damping foundation, seals and bearings damping.

During the construction of the damping matrix (C) from Rayleigh damping coefficients we need to know α and β . The following section shows how these coefficients affect the frequency and the forms of rotor vibrations.

5.1. Influence of β coefficient

Two analyzes were performed. In the first one α coefficient remained unchanged ($\alpha=3,0$) and β coefficient has been increased twice (from $\beta=0,000005$ to $\beta=0,00001$). In the second analysis β coefficient has been increased tenfold ($\beta=0,00005$)

In the first test, the coefficient β was increased twice in relation to the basic. The results are shown in Tab. 4. A view of the individual forms of vibration was shown in Figure 6. The differences between the first six frequencies in basic model and this are about 1 %.

In a next analysis, the coefficient β was multiplied by ten. The results are shown in tab. 5. A view of the individual mode shapes is shown in Figure 7. The differences between the first and the second frequency in this model and base model is approximately 1 %. The difference between the third and fourth frequency is approximately 11 %. The difference between the fifth and sixth frequency is as high as 84 %.

Tab. 4. The first eight natural frequencies and corresponding damping coefficients for the basic model with coefficients $\alpha=3,0$; $\beta=0,00001$.

	$\alpha=3,0$; $\beta=0,00001$	
	frequency [Hz]	damping [-]
1	568,41 (1)	-69,95
2	568,41 (2)	-69,95
3	2920,04 (3)	-1712,63
4	2920,04 (4)	-1712,63
5	6164,74 (5)	-7842,80
6	6164,74 (6)	-7842,80
7	7131,85	-10625,86
8	7131,85	-10625,86

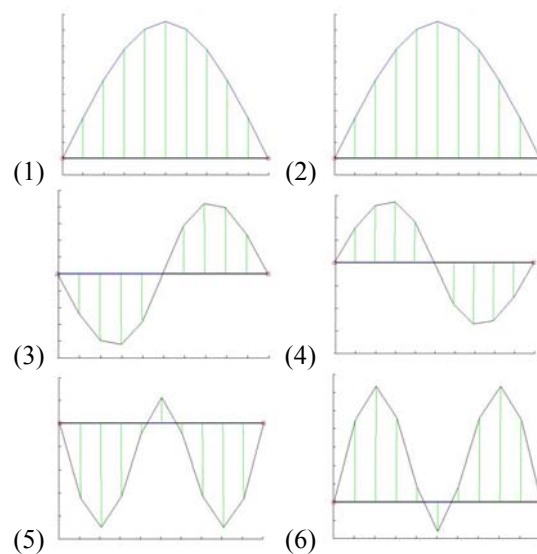


Fig. 6. Forms of vibration for the base model $\alpha=3,0$; $\beta=0,00001$.

Tab. 5. The first eight natural frequencies and corresponding damping coefficients for the basic model with coefficients $\alpha=3,0$; $\beta=0,00005$.

	$\alpha=3,0$; $\beta=0,00005$	
	frequency [Hz]	damping [-]
1	566,03 (1)	-324,75
2	566,03 (2)	-324,75
3	1009,69 (3)	-38924,78
4	1009,69 (4)	-38924,78
5	2600,80 (5)	-8486,10
6	2600,80 (6)	-8486,10
7	2249352,99	-11126,08
8	2249352,99	-11126,08

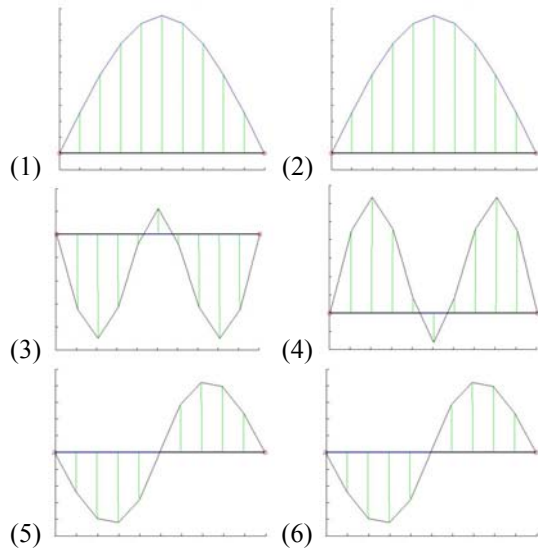


Fig. 7. Mode shapes for the base model, $\alpha = 3,0$; $\beta = 0,000005$.

5.2. Influence of α coefficient

Two tests were performed during which β coefficient was constant ($\beta = 0,000005$) while the coefficient α was decreased tenfold ($\alpha = 0,3$), and increased it tenfold ($\alpha = 30,0$). Below are the results. In the first test, the coefficient α has been reduced in relation to the base of ten. The results are shown in Tab. 6. In the second test coefficient α was increased tenfold ($\alpha = 30,0$). The results are shown in Tab. 7. Mode shapes at all frequencies are the same as in the base case. The difference between the frequencies of the first six mode shapes in this model and base model are negligible, and thus it can be concluded that the coefficient α slightly affects the natural frequency of the rotor in this case.

Tab. 6. The first eight natural frequencies and corresponding damping coefficients for the reference model, the coefficients $\alpha = 0,3$; $\beta = 0,000005$.

$\alpha = 0,3; \beta = 0,000005$		
	frequency [Hz]	damping [-]
1	568,51 (1)	-37,66
2	568,51 (2)	-37,66
3	2929,75 (3)	-864,06
4	2929,75 (4)	-864,06
5	6259,82 (5)	-3942,38
6	6259,82 (6)	-3942,38
7	7281,65 (7)	-5329,52
8	7281,65 (8)	-5329,52

Tab. 7. The first eight natural frequencies and corresponding damping coefficients for the reference model, the coefficients $\alpha = 30,0$; $\beta = 0,000005$.

$\alpha = 30,0; \beta = 0,000005$		
	frequency [Hz]	damping [-]
1	568,50 (1)	-42,39
2	568,50 (2)	-42,39
3	2929,70 (3)	-871,48
4	2929,70 (4)	-871,48
5	6259,62 (5)	-3955,11
6	6259,62 (6)	-3955,11
7	7281,50 (7)	-5337,97
8	7281,50 (8)	-5337,97

6. COMPARISON WITH COMMERCIAL SOFTWARE

The results of the Dynwir-S-70 were compared with a commercial program for analysis of rotors - Madyn 2000. In both programs, models have been constructed with regard to the same geometrical parameters and the same conditions in the bearing support. Natural frequencies received using Madyn 2000 software are presented in Table 8. The corresponding mode shapes are shown in Figure 8.

Tab. 8. The first eight natural frequencies and corresponding damping in Madyn 2000 software.

$\zeta = 0,1$		
	frequency [Hz]	damping [%]
1	568,40 (1)	0,2
2	568,59 (2)	0,2
3	2918,95 (3)	0,1
4	2948,99(4)	0,1
5	6320,71(5)	0,1
6	6323,07(6)	0,1
7	7344,37	0,1
8	7370,84	0,1

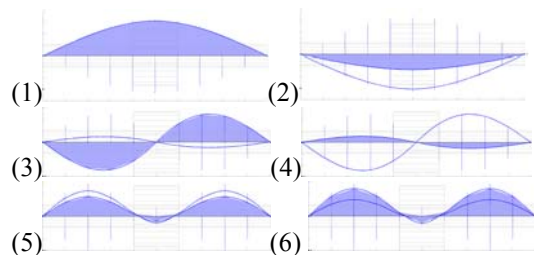


Fig. 8. Mode shapes – calculated in Madyn 2000.

The differences in frequencies between particular mode shapes in Madyn 2000 and Dynwir-S-70 for the base case are approximately 1 %. These differences may be due to a different algorithm of calculating the eigenvalues, or a different discretization of the model.

7. SUMMARY AND CONCLUSIONS

The paper presents basic information about the Dynwir-S-70 software. Influence of discretization model (using Bernoulli-Euler beam and Timoshenko beam) on natural mode shapes and natural frequencies of the system was presented. This paper briefly discusses the Rayleigh proportional damping model and the impact of the coefficients (α and β) for the natural frequencies and. By appropriate selection of α and β coefficient some forms of vibration can "reveal" or can "disappear" in modal analysis. As it turns out, in this case much greater impact on the results of the modal analysis is the value of the coefficient β than α .

Developing the Dynwir-S-70 software allows the modal analysis of the rotor supported on slide bearings. In the nearest future it is planned to expand the program Dynwir-S-70 with non-linear elements in the modal analysis.

BIBLIOGRAPHY

- [1] Markiewicz-Kicińska A., *Instrukcja – ogólne uwagi dotyczące niektórych programów obliczeniowych i graficznych stosowanych w 04/Z3*, Gdańsk, Oprac. wew. IMP PAN Nr Arch.: 4125/04, 2004.
- [2] Uhl T., *Praktyczne problemy analizy modalnej konstrukcji*, Kraków, Wydawnictwo AGO, 1996.
- [3] Kruszewski J., *Metoda elementów skończonych w dynamice konstrukcji*, Warszawa, Wydawnictwo Arkady, 1984.
- [4] Kiciński J., *Dynamika wirników i łożysk ślizgowych*, Gdańsk, Maszyny przepływowe pod redakcją Eustachego S. Burki, tom 2, Wydawnictwo IMP PAN 2005.
- [5] Kiciński J., *Identyfikacja parametrów modelu oraz nieliniowa analiza wpływu wybranych defektów w pracy obiektu rzeczywistego turbozespołu -13K215. Część I: Identyfikacja parametrów modelu*, Gdańsk, Nr Arch. 129/97, Instytut Maszyn Przepływowych PAN



Lukasz BREŃKACZ – an assistant in the Rotor Dynamics and Slide Bearings Department in the Institute of Fluid-Flow Machinery Polish Academy of Sciences in Gdansk.



Pawel BAGIŃSKI – an assistant in the Rotor Dynamics and Slide Bearings Department in the Institute of Fluid-Flow Machinery Polish Academy of Sciences in Gdansk.



Malgorzata BOGULICZ – a specialist in the Rotor Dynamics and Slide Bearings Department in the Institute of Fluid-Flow Machinery Polish Academy of Sciences in Gdansk.

EXAMINATION OF THERMAL DEFORMATION OF MICRO MILLING MACHINE TOOL SNTM-CM-ZUT-1

Mirosław PAJOR¹, Henryk MAĆKOWIAK¹, Jacek ZAPŁATA²

¹Institut Technologii Mechanicznej, ²Katedra Mechaniki i Podstaw Konstrukcji Maszyn,
Zachodniopomorski Uniwersytet Technologiczny w Szczecinie,
Al. Piastów 19, 70-310 Szczecin, tel.: 91-449-42-66, faks: 91-449-44-42,
miroslaw.pajor@zut.edu.pl, henryk.mackowiak@zut.edu.pl, jacek.zaplata@zut.edu.pl

Summary

This paper presents thermal analysis of micro milling machine tool SNTM-CM-ZUT-1. Infrared camera images are utilised to identify major heat sources in the machine tool. The influence of the heat generated in linear motors and frictional heat generated in spindle on the machine tool body temperature is examined. Basing on the CAD geometry and IR measurement, the thermal expansion of the machine is evaluated by means of the FEM analysis. The study indicates places where constructional improvements can be made in order to decrease thermal error influence. Moreover, the time period ensuring the thermal stability is identified.

Keywords: thermal error, micromachining, FEM, IR measurement.

OCENA ODKSZTAŁCEŃ CIEPLNYCH OBRABIARKI DO MIKROFREZOWANIA SNTM-CM-ZUT-1

Streszczenie

W pracy przedstawiono analizę odkształceń cieplnych obrabiarki do mikrofrezowania SNTM-CM-ZUT-1. Celem zidentyfikowania głównych źródeł ciepła maszyny wykorzystano pomiar kamerą termowizyjną. Zbadano wpływ ciepła wydzielanego podczas pracy napędów liniowych oraz wrzeczona na temperaturę korpusów mikrofrezarki. Na podstawie zmierzonych temperatur oraz znajomości geometrii obrabiarki opracowano model MES. Pozwolił on oszacować odkształcenia cieplne jakim poddawana jest obrabiarka podczas pracy. Wskazano potencjalne elementy konstrukcji, których modyfikacja może zredukować wielkość odkształceń cieplnych. Dodatkowo, wyznaczono cieplne stałe czasowe maszyny.

Słowa kluczowe: odkształcenia cieplne, mikroobróbka, MES, termografia.

1. INTRODUCTION

The influence of the thermal error in traditional machining is usually noticeable at the stage of the finishing treatment. In the case of micromachining, where feed rates and machine depth have micrometer orders of magnitude, the influence of thermal error might be crucial [1].

Conventional mechanical FEM analysis, used to project and examine features of machine tools design, augmented with multiphysics analysis, allows to predict the thermal expansion of machine tool body causing the thermal errors [2, 3]. Thus, it allows to implement the necessary structural changes in future machines or algorithms compensating thermal errors in the existing ones [4, 5].

In the described method, the FEM model consists of two parts: the thermal one and the mechanical one. The temperature distribution obtained on the basis of the thermal analysis constitutes a part of the boundary conditions for further mechanical analysis.

In this paper, an IR measurement of an existing facility was used in order to simplify the modelling process by taking the thermal boundary conditions a priori. IR measurements, owing to the use of high-resolution radiometric matrixes, are characterised by good imaging properties in order to examine the whole of thermal phenomena [6]. The combination of multiphysical FEM modelling with thermography provides a convenient way to estimate the machine thermal deformation.

2. IR MEASUREMENT OF A MACHINE

The negative features of IR measurements include the measurement uncertainty based upon the measurement scheme itself. It has to be emphasised that in not the temperature of the examined surfaces that is recorded, but the amount of radiation reaching the radiometric converter. The amount of the radiated energy from the surface which is examined depends on the temperature of the measured body, as well as the condition of this surface – emissivity coefficient. In addition, the impact on recorded value

have the ambient radiation and the radiation of external sources reflected from the examined surface. Therefore, IR measurements always require due diligence, attention and in-depth knowledge from the operator performing the measurement.

To make the value of the registered temperatures independent from the surface condition, the observed machine was covered with tape, which had a known emissivity coefficient. To verify the conducted IR measurements, additional PT100 temperature sensors were mounted on the observed machine. Those are indicated in Fig. 1 with the following symbols: S1, S2 and S3.

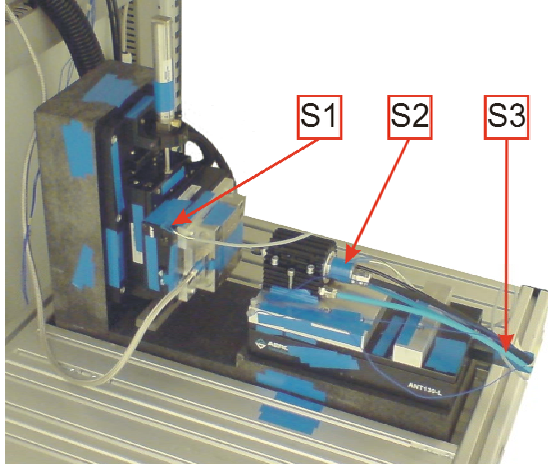


Fig. 1. Micro-milling machine tool covered with a tape with a reference emissivity coefficient, the temperature sensors marked: S1, S2, S3

2.1. Infrared observation of the spindle

The measurement of the current supplying the spindle of the SNTM-CM-ZUT-1 micro milling machine tool showed that the thermal power emitted in the spindle is somewhat between 8÷50W, depending on the rotational speed. The device is provided with two parallel spindle cooling methods: with a radiator (by convection and radiation) and flowing water.

The amount of heat convected and emitted from the radiator to ambient air depends on the temperature of both. The ambient temperature is to be maintained at a constant level, by means of an air-conditioned chamber, in which the device is located. The amount of the heat convected and emitted only radiator is insufficient for the micro milling machine to reach stable thermal conditions quickly. At rotational speed rate 35,000 rpm, heat generation rate equal to $P = 8W$, the stable conditions were not achieved at this conditions even after 45min, if additional cooling is not used. (see Fig. 2).

In order to quickly stabilise the temperature of the milling machine and prevent seizure of the bearings with higher rotational speeds, it is necessary to activate the water cooling system.

The effectiveness of water cooling is dependent on the temperature of coolant and its flow rate. The installed cooling system enables achieving stable conditions already after 20 minutes.

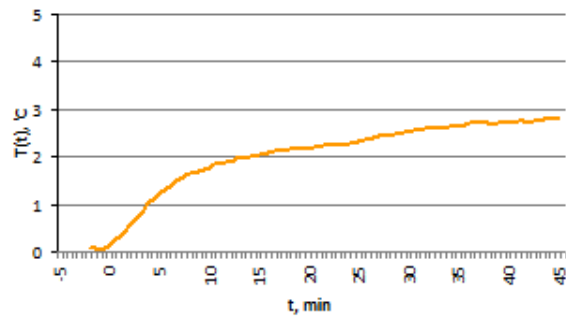


Fig. 2. Temperature surplus of the spindle, relative to ambient, registered by sensor S2 during the work of the micro milling machine tool. Water cooling system off, spindle velocity - 35,000 rpm

Changing the spindle rotational speed affects the temperature of the system. During the experiment for the rotational speed of 75,000 rpm, heat generation rate equal to $P = 40W$, the spindle temperature stabilises after about 20 minutes at the level of 5 °C below the ambient temperature. For the rotational speed of 35,000 rpm, heat generation rate equal to $P = 8W$, the temperature of the previously heated spindle stabilises after about 20 minutes at the level of 6.5 °C below the ambient temperature (Fig. 3).

The conducted measurements suggest that in order to eliminate the influence of thermal deformation resulting from thermal elongation of the spindle, basing the tool relative to the workpiece should be performed after about three time constants. Knowing the $\tau \approx 5$ min, this results in about 15 minutes time for thermal stabilization from the moment of switching on the spindle.

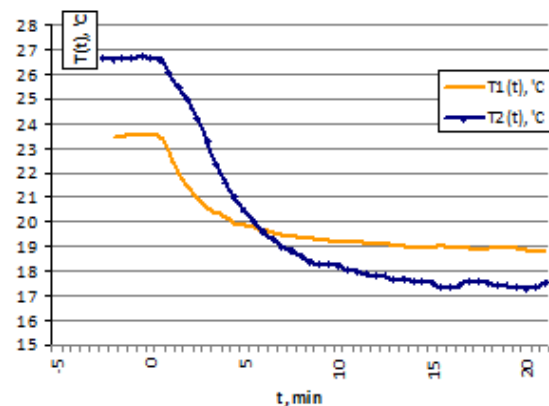


Fig. 3. The temperature recorded by sensor S2 during the work of the micro milling machine with active water cooling system, constant ambient temperature, different initial temperatures of the system, the rotational speeds of:
T1: $v_r = 75,000$ rpm, T2: $v_r = 35,000$ rpm

In addition, Fig. 3. shows the fact that with a significant change of the spindle rotational speed it may be necessary to rebase the tool.

Fig. 4. presents the impact of water cooling system work on the temperature of headstock and the body elements of the micro milling machine.

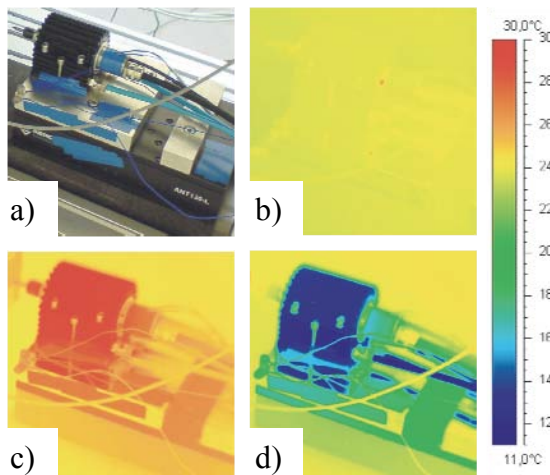


Fig. 4. Results of the IR spindle temperature measurements: a) photo of the spindle taken in the visible range; b) spindle under conditions of the thermal equilibrium with the surroundings; c) spindle heated by turning on the rotation d) spindle heated by turning on the rotation with an activated water cooling system

2.2. Infrared observation of the Z axis

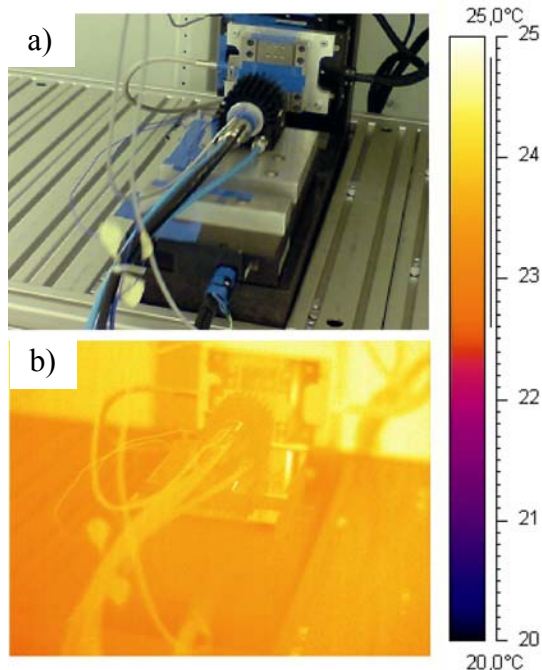


Fig. 5. Results of IR measurement of axis Z temperature: a) photo of the micro milling machine taken in the visible range; b) negligible impact of the Z axis movement on the temperature of the micro milling machine

The relative motion of the the tool in relation to the workpiece is driven by linear motors, different power each. The thermal image (Fig. 5.) indicates that the amount of heat generated in the linear motor of the Z axis when it moves, is insignificant for the

machine tool temperature, even when its velocity reaches 50mm/s.

2.3. Infrared observation of the X and Y axis

The work of the motors in the X and Y axis has a significant impact on the temperature of the micro milling machine body.

In order to balance the gravitational vertical load of the micro milling machine axis Y, this axis is equipped with a pneumatic actuator powered by constant pressure at an adjustable level. However, despite the apparent relief of the linear motor of the feed axis Y by means of a pneumatic actuator, the linear motor of the Y axis is constantly loaded. This causes the heating of the Y axis motor from the moment of turning on, even if it is seemingly idle. The heating rate of the micro milling machine is presented in the reading from the sensor S1 located on the movable table of the feed axis X (Fig. 6.).

The movements of the feed axis X and Y were activated in the 40th minute, which may be observed as an increase in the rate of temperature measured by the S1 sensor.

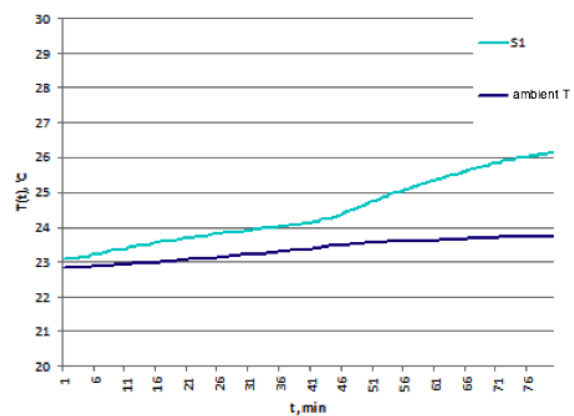


Fig. 6. The temperature recorded by sensor S1 and ambient temperature during the idle operation of the micro milling machine linear motors, movement of the feed axis X and Y activated approximately at 40-th minute

The heat flux generated in the linear motor of the Y and X axis causes heating of the vertical granite column of the device base. Pictures taken with the infrared camera provide information on the temperature distribution field of the machine tool (Fig. 7).

Due to low conductivity and high heat capacity of the granite, both in transient and fixed states, a clear temperature gradient can be observed in the abovementioned column. The occurrence of the temperature gradient in this element results in the thermal deflection of the granite column.

Approximating the measured change of the temperature in the column in time with the exponential function, we receive a time constant of the temperature change in the column, amounting to approx. 1h. To eliminate the effect of thermal deformation of the column on the relative position of the tool and the workpiece, it is necessary to wait

until the system reaches stable thermal conditions or introduce structural changes, reducing the impact of the described effect.

The remaining elements, mostly made of aluminium, are characterised by high thermal conductivity and low heat capacity. These elements, with a good approximation, may be treated as lumped capacity elements.

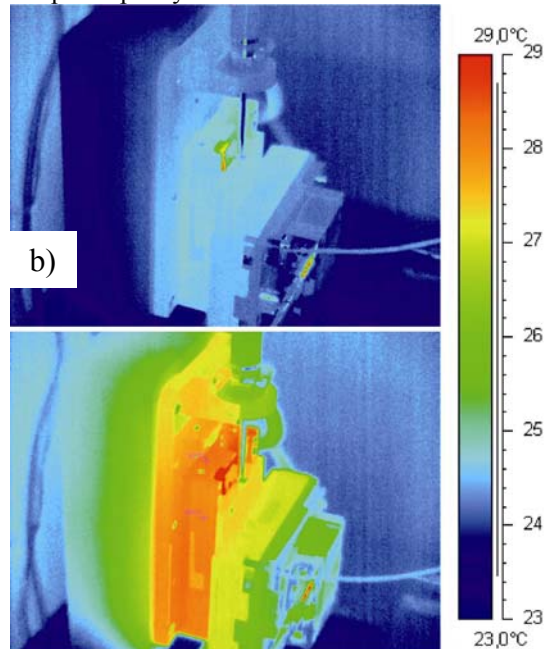


Fig. 7. Photo of the feed X and Y axis of the micro milling machine taken with an IR camera: a) immediately after switching on the motors; b) after 35 min from the moment of switching on the motors

3. FEM MODEL

On the basis of the possessed CAD data, a simplified model of the machine tool geometry for the FEM calculation purposes was constructed. The assumed physical properties of materials are presented in Table 1.

Tab. 1. Assumed physical properties of materials

	Granite	Aluminium	Steel
Thermal expansion coefficient α , $\mu\text{m}/\text{m}/^\circ\text{C}$	10	24	12
Density ρ , kg/m^3	2700	2700	7850
Specific heat c_p , $\text{J}/\text{kg}/^\circ\text{C}$	700	300	500
Thermal conductivity coefficient λ , $\text{W}/\text{m}/^\circ\text{C}$	3,5	230	50
Young modulus, GPa	14	37	210

It was assumed that the elements of the driving components are made of aluminium [12], the column of granite, and the spindle elements of steel. The view of the geometric model divided into elements is presented in Fig. 8. The grid consists of default elements: "hexa" and "tetra." To simplify

the calculation process, only the symmetric part of the machine was modelled.

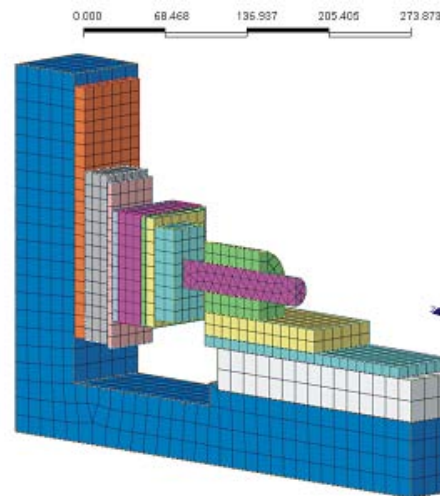


Fig. 8. FEM model of a micro milling machine tool

3.1. Thermal model

On the basis of the analytical dependencies and the IR measurements, some assumptions allowing to calculate the temperature distribution field of the machine tool were made. Furthermore, it was assumed the heat transfer coefficient on free surfaces is equal to $5 \text{ W}/\text{m}^2/^\circ\text{C}$. In order to map the conduction of heat to the table on which the machine tool is located, it was assumed that the heat transfer coefficient at the base surface amounts to $100 \text{ W}/\text{m}^2/^\circ\text{C}$.

It was assumed that the density of the heat flux penetrating the column of the headstock amounts to $100 \text{ W}/\text{m}^2$, which corresponds to the heat rate 1.6 W transferring to the granite column. The ambient temperature was set at the level of 26°C . In addition, it was assumed that the elements made of aluminium with a good approximation, have a uniform temperature amounting respectively to: 29.5°C - dynamometer, 30.0°C - plate under the dynamometer; 31.0°C - X axis, the upper part; 31.5°C - X axis, the lower part, plate under the X axis, Y axis, the upper part; 33.0°C - Y axis, the lower part; 32.5°C - plate under the Y axis; 26.0°C - spindle, radiator, Z axis, the upper part, Z axis, the lower part, plate under the Z axis.

It should be emphasised that calculating the temperature distribution field of the whole micro milling machine is necessary, since the IR measurements provide data only concerning the surface temperature distribution of the machine tool, whereas in order to estimate heat deformations, it is necessary to provide the data concerning the temperature of the machine tool throughout its whole volume. Due to the fact that there is no heat flow between the elements of the same temperature, it was assumed that the plane of symmetry is an excellent insulator.

Comparing Fig. 9. and Fig 10., which present the temperature distribution field calculated using the numerical method and recorded with an infrared camera, it can be assumed that the results were satisfactorily consistent.

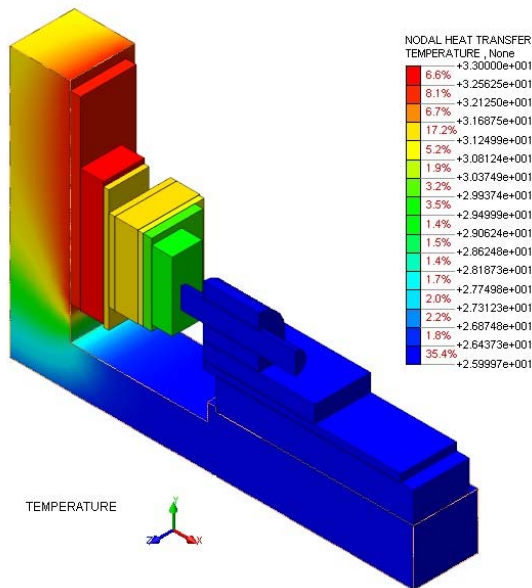


Fig. 9. Temperature field distribution of the micro milling machine calculated by means of FEM

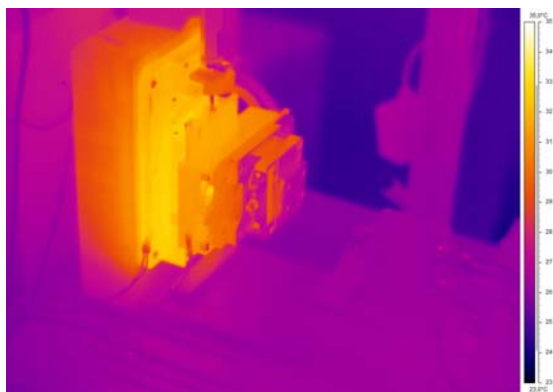


Fig. 10. Temperature distribution field of the micro milling machine recorded with an infrared camera

3.2. Mechanical Model

In the mechanical model it was assumed that the plane of symmetry has removed degrees of freedom connected with translation in the Z axis. In addition, it was assumed that the tool tip point has removed degrees of freedom corresponding to X and Y axis translation.

In the presented Fig. 11, apart from the errors resulting from the translation of the tool relative to the workpiece as a result of linear thermal expansion of structural elements, it is visible that the occurrence of the temperature gradient in the granite column leads to its deflection. This phenomenon will cause the distancing of the tool from the workpiece.

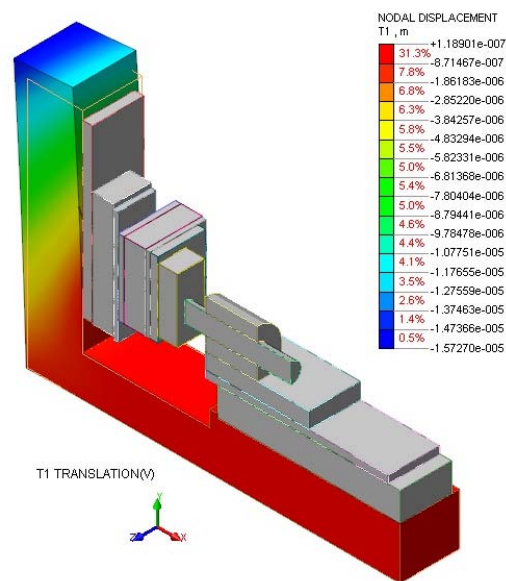


Fig. 11. Deformation of the granite base in the X axis calculated with the use of the finite element method

4. Experimental verification

The verification studies focused on the thermal deformation of the column. In order to verify the calculations, it was necessary to measure the translation of the point located on the granite column.



Fig. 12. Photo of the measurement system used to measure thermal deformations of the micro milling machine

The measurement was conducted with a Renishaw XL80 laser interferometer. The first mirror was mounted on the granite column, whereas the second one on the stationary Z axis (Fig. 12). Thermographic pictures show that the increase in the temperature of the interferometer mirrors was so slight that it was possible to neglect thermal expansion of these optical elements.

The study showed that the heat deformations of the column, expected according to an estimate of

deformations by means of the FEM method, occurred. The order of magnitude of deformations is consistent with the conducted estimate, which is confirmed by Fig. 13.

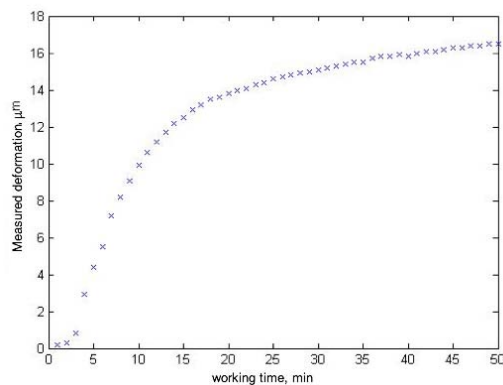


Fig. 13. The measurements of thermal deformations of the granite base collected in the experiment, along X axis

5. CONCLUSIONS

The conducted investigation showed that thermal deformations can have a significant impact on the geometric errors of the micro milling machine. This as a result, leads to the disruption of micromachining parameters, which orders reach micrometers.

IR measurement on the basis of the engineering knowledge allows for diagnosing the modes of thermal deformations essential for the work of the machines.

The application of the finite element method in terms of heat flow analysis in connection with the traditional mechanical modelling allows to estimate the nature and range of thermal deformations.

Precise estimation of thermal deformations is problematic due to the non-stationary nature of heat phenomena and multiplicity of parameters within the models.

LITERATURE

- [1] Chae J., et al.: *Investigation of micro-cutting operations*. International Journal of Machine Tools & Manufacture 46, 2006, p. 313–332
- [2] Min X., et al.: *An improved thermal model for machine tool bearings*. Int. Journal of Machine Tools & Manufacture 47, 2007, p. 53–62
- [3] Jong-Jin Kim, et al.: *Thermal behavior of a machine tool equipped with linear motors*. Int. Journal of Machine Tools & Manufacture 44, 2004, p.749–758
- [4] Pietruszewicz K., Pajor M., Urbański Ł.: *Dynamic corrections of the tooling errors possibilities within the mechatronic actuator for motors with permanent magnets*. Archiwum Technologii Maszyn i Automatykacji vol. 31 nr 2, 2011, p. 181-190.

- [5] Pajor M., Zapłata J.: *Compensation of thermal deformations of the feed screw in a CNC machine tool*. Advances in Manufacturing Science and Technology, 2011 Vol. 35, No. 4, 2011, p. 9-17
- [6] Rutkowski, P.. Oprac. Madura, Henryk. Red.: *Pomiary termowizyjne w praktyce*. Warszawa, Agenda Wydawnicza SIMP, 2004
- [7] Minkina, W. Red.: *Wybrane problemy współczesnej termografii i termometrii w podczerwieni*. Częstochowa, Wydawnictwo Politechniki Częstochowskiej, 2011
- [8] Broel-Plater B., Waszczuk P., Kobyłkiewicz A.: *System diagnostyki i procesu mikroskrawania*. Napędy i Sterowanie. 2011, nr 6, s. 90-94
- [9] Adams V., Askenazi A.: *Building Better Products with Finite Element Analysis*. Santa Fe, OnWord Press 1999
- [10] Lewis R. W., Nithiarasu P., Seetharamu K. N.: *Fundamentals of the finite element method for heat and fluid flow*. New York, John Wiley & Sons 1984
- [11] Kreith F., Bohn M. S.: *Principles of heat transfer, fifth edition*. Boston, PWS Publishing Company 1997
- [12] Raznjevic K.: *Tablice cieplne z wykresami: Dane liczbowe w układzie technicznym i międzynarodowym*. WNT, Warszawa 1964
- [13] <http://www.aerotech.com/product-catalog/stages/linear-stage.aspx>



Mirosław PAJOR, PhD, Eng., Prof. of the WPUT, Head of the WPUT Institute of Mechanical Technology and Head of the WPUT Mechatronics Centre. Interests: machine dynamics, intelligent control and diagnostic systems of CNC machine tools.



Henryk MAĆKOWIAK, PhD, Eng., Dean of the WPUT for Student Affairs, senior lecturer at the Institute of Mechanical Technology of the WPUT. Interests: machine tools, machine dynamics, computer analysis of machine properties, databases.



Jacek ZAPŁATA, M.Sc. PhD student of the WPUT. Research assistant at the Department of Mechanics and FMC. Interests: heat deformations of machine tools, IR measurements, robotics.

TIME-FREQUENCY ANALYSIS OF TIME-VARIANT SYSTEMS

Kajetan DZIEDZIECH, Wiesław J. STASZEWSKI, Tadeusz UHL
Akademia Górniczo-Hutnicza im. Stanisława Staszica, Katedra Robotyki i Mechatroniki
Al. Mickiewicza 30, 30-059 Kraków, Fax : +48 12 634 3505, E-mail: dziedzie@agh.edu.pl,
w.j.staszewski@agh.edu.pl, tuhl@agh.edu.pl

Summary

System identification is an important and often complex process in many areas of engineering. This process is not easy when parameters of the analysed system vary with time. In such cases classical methods fail to identify parameters properly. The work demonstrated in this paper deals with time-frequency representations for identification of natural frequencies of time-variant systems. The method involves the estimation of time-variant transfer functions. A "Crazy Climbers" algorithm - based on Monte Carlo simulations and Markov chains - is used to overcome difficulties associated with the method.

Keywords: system identification, time-frequency analysis, functional ridges, "Crazy Climbers"

CZASOWO-CZĘSTOTLIWOŚCIOWA ANALIZA SYSTEMÓW ZMIENNYCH W CZASIE

Streszczenie

Identyfikacja parametrów systemów mechanicznych jest bardzo ważnym i skomplikowanym procesem. Proces ten jest o wiele bardziej skomplikowany kiedy dotyczy systemów mechanicznych, których parametry zmieniają się w czasie. W takim przypadku klasyczne metody identyfikacji nie są w stanie poprawnie zidentyfikować tych parametrów. Artykuł zajmuje się wykorzystaniem reprezentacji czasowo-częstotliwościowych w celu identyfikacji częstotliwości drgań rezonansowych systemów o zmiennych w czasie parametrach. Jednym z kroków podczas estymacji funkcji przejścia jest dzielenie spektrum odpowiedzi przez spektrum wymuszenia, co często prowadzi do dzielenia przez wartości bliskie zera, a to prowadzi do nieskończonych (lub niezdefiniowanych) wartości. W celu ominięcia tego problemu zastosowano probabilistyczną metodę „CrazyClimbers”, opartą na symulacjach Monte Carlo oraz łańcuchach Markova.

Słowa kluczowe: identyfikacja systemów, analiza czasowo-częstotliwościowa, grzbiety funkcji, "CrazyClimbers"

1. INTRODUCTION

Estimation of instantaneous frequency of mono-component signals $x(t)$ can be obtained from the instantaneous phase which is argument of complex function of Hilbert transform of given signal [1]. It is well known that the Hilbert transform can be calculated from the Fourier transform by a proper manipulation of spectral components. When multi-component signals are used some additional signal processing is required to extract the instantaneous frequency. This results from the simple fact, that every multi-component signal can be decomposed into a series of mono-component signals, e.g. by means filtering or the Empirical Mode Decomposition (EMD). The latter leads to a number of the so-called Intrinsic Mode Functions (IMFs). Instantaneous frequencies can be extracted from each of these IMFs in same manner as in case of mono-component signals. The entire process is often called the Hilbert-Huang Transform (HHT) despite the fact that the EMD is not a transform in a

mathematical sense. Nevertheless the method is a powerful tool in signal processing and has been used to solve many engineering problems [2].

An alternative approach for estimation of instantaneous frequencies can be proposed when ridges of time-frequency representations are analysed. Intuitively, ridges are curves that concentrate signal's energy. Methods concerning identification of instantaneous frequency with the use of ridges are relatively well established in the case of mono-component signals. The simplest approach for ridge identification is based on calculation of local time-frequency maxima [3]. It is well known that local maxima (or in fact ridge values) correspond to instantaneous frequency of signal. This process can be written as

$$|TF(t, \omega_t)| = |\max_{\omega} TF(t, \omega)| \quad (1)$$

where TF denotes time-frequency transformation or distribution, t denotes time variable, ω is frequency variable and \max_{ω} is maximal value along

frequency variable. It is important to note that the above definition is limited to mono-component signals only. The ridge-based method can be also applied to multi-component signals when appropriate time-frequency filtering is used. However this is not an easy task particularly when noisy data - often associated with real measurements - are used. In such cases various optimization algorithms are required to obtain ridges.

Various approaches can be used for identification of time-variant systems. Parametric methods are often used for estimation of FRFs for time-variant systems. These methods are based on parametric models. The Auto-Regressive (AR), Auto-Regressive Moving-Average (ARMA), Auto-Regressive Moving-Average with exogenous inputs (ARMAX) models and many other approaches can be used for LTI systems [4]. Time-variant systems are often analysed using similar but modified approaches. There exist a number of time-dependent parametric methods, starting from simple models such as the Time-dependent AR (TAR) and Time-dependent ARMA (TARMA) to more complex and computationally demanding models such as the Recursive Maximum Likelihood estimated TARMA (RML-TARMA), Smoothness Priors TARMA (SP-TARMA), Functional Series TARMA (FS-TARMA) and other variations of these models are discussed in [5]–[8].

The objective of the paper is to present alternative method to parametric methods. This method will be based on non-parametric transformations such as Short Time Fourier Transform (STFT), in combination with Crazy Climbers algorithm. However, other time-frequency or even time-scale representations can be also used, as shown in [9], [10].

The structure of the paper is as follows. For the sake of completeness Section 2 briefly describes input-output analysis of classical time-invariant systems. The Time-Variant Frequency Response Functions (TVFRF) is presented in Section 3. The concept of ridges is presented in Section 4. The optimization algorithm used for ridge extraction is shown in Section 5. Simulated examples and results are given in Section 6. Finally the paper is concluded in Section 7.

2. INPUT-OUTPUT ANALYSIS OF SYSTEMS

Different methods can be used for signals. The two most common approaches utilise time responses and power spectra. Analysis of time response leads to information on signal amplitude and localisation of events in time. The simplicity is the major advantage of this approach. Relatively very little signal post-processing is required to obtain basic information. In contrast, analysis in the frequency domain, based for example on power spectra, provides information about frequency content of the

analysed signal. The well-known Fourier transform defined as:

$$X(\omega) = F[x(t)] = \frac{1}{2\pi} \int_{-\infty}^{+\infty} x(t)e^{-j\omega t} dt \quad (2)$$

can be used to obtain power spectra. In modal analysis the FRF defined as the frequency-domain ratio between the output (or response) $Y(\omega)$ and input (or excitation) $X(\omega)$, i.e.

$$H(\omega) = \frac{Y(\omega)}{X(\omega)} = \frac{F[y(t)]}{F[x(t)]} \quad (3)$$

allows for modal parameters (natural frequency, damping and mode shapes) to be estimated. Once the FRF is given the response can be obtained in the time domain using the inverse Fourier transform as

$$y(t) = \frac{1}{2\pi} \int_{-\infty}^{+\infty} Y(\omega)e^{j\omega t} d\omega \quad (4)$$

Another way of representing dynamic response of mechanical systems to given excitations is the well-known impulse response function defined as

$$h(t) = \frac{1}{2\pi} \int_{-\infty}^{+\infty} H(\omega)e^{j\omega t} d\omega \quad (5)$$

It is clear that the response of the analysed system can be obtained from the impulse response function using the convolution theorem as

$$y(t) = \int_{-\infty}^{+\infty} h(s) x(t-s) ds \quad (6)$$

The major disadvantage of the classical method described in this section is the fact that the Fourier Transform is capable to analyse properly only time-invariant signals. The application of this approach to time-variant systems may lead to incorrect FRFs and identified physical/modal parameters. This is the reason why other approaches are required.

3. TIME-VARIANT FREQUENCY RESPONSE FUNCTION

The classical FRF can be extended intuitively for time-variant systems to provide time-frequency localisation capability. When the analysis is limited to small periods of time that exhibit time-invariant behaviour, time-variations are negligibly small and the Time-Variant Frequency Response Function (TVFRF) can be defined as

$$H(t, \omega) = \frac{Y(t, \omega)}{X(t, \omega)} = \frac{TF[y(t)]}{TF[x(t)]} \quad (7)$$

where TF denotes time-frequency transformation or distribution. More information about this ratio can be found in [9]–[11]. For simplicity, the work presented in this paper utilises the STFT to obtain input and output time-frequency spectra needed to calculate the TVFRF in Equation (7).

Equation (7) is relatively simple often not easy to use in practice. For values of $TF[x(t)]$ that are close to zero, the $H(t, \omega)$ tends to infinity. This makes it very difficult to interpret. That is why additional post-processing is required to avoid the above problem.

4. RIDGES OF FUNCTIONS

For the sake of completeness concept of canonical representation of real signals is recalled in this section for better understating related to functional ridges. It is well known that any real signal can be represented in terms of its instantaneous amplitude A and phase φ

$$x(t) = A(t) \cos(\varphi(t)) \quad (8)$$

Instantaneous frequency can be easily derived from instantaneous phase:

$$\omega(t) = \frac{1}{2\pi} \frac{d\varphi(t)}{dt} \quad (9)$$

More information on both instantaneous signal characteristics be found in [12], [13]. Various methods can be used to obtain the instantaneous amplitude and frequency of signals. The most commonly used algorithm is based on the Hilbert transform. These characteristics can be also obtained from the time-frequency and time-scale representation. The major areas where the signal energy is concentrated need to be localized. These areas form a smooth curve that joins local maxima of the transform. The curve is often called a ridge of the transform. Ridges can be then used to obtain the instantaneous frequency and amplitude. The former is obtained when ridge localization is performed. The process of combining single ridges into sequence is called chaining. The latter is achieved when the amplitude corresponding to ridge area is analyzed.

When Equation (7) is used the entire concept of ridges can be utilised in system analysis. Then instead of instantaneous frequency, natural frequency will be considered.

5. RIDGE EXTRACTION PROCEDURE

5.1 Crazy Climbers Algorithm

The time-variant FRF defined by Equation (7) does not involve any data averaging in the time domain. When additionally the data analysed are noisy and close vibration modes are involved, the process of ridge extraction and ridge chaining can lead to significant numerical errors and difficult interpretation. Various post-processing algorithms can be applied to avoid such difficulties. The so-called "Crazy Climbers" algorithm is one of the possible methods that can be used in practice. This

method is based on the Monte Carlo Markov Chain (MCMC) simulations. The main idea of the method is to use the TVFRF to generate a random walk on the time-frequency plane, in such way that the random walker is attracted by the ridges of the hills. In addition, the random walk is done at a given "temperature" which changes with time. The temperature is gradually decreased in the process, as in the simulated annealing algorithm. However, contrary to the simulated annealing procedure, the motion of the walker is unrestricted in one direction and walker is never stuck on the ridge. Thanks to the temperature schedule, each climber is expected to spend most of his time walking along one or another ridge involved. Therefore there are a number of walkers instead of just one and the entire procedure is suitable for multi-degree-of-freedom (MDOF) systems. Thanks to these random walks, one can create the so-called occupation measures. These occupation measures are created for each point on the time-frequency plane. They represent numbers of time that certain points have been visited by walkers. The occupation measures are expected to have higher values near ridges as they are more attractive for climbers. The "Crazy Climbers" algorithm has a great advantage in terms of possible mode separation when closed vibration modes are involved. More detailed description of the entire algorithm can be found in [14], [15]. When occupation measures are created the results are chained to obtain skeletons. The chaining procedure consists of two major steps. Firstly, thresholding of occupation measures is performed. Values below the pre-defined fixed value τ are forced to zero, i.e.

$$\rho(t, \omega_n) = \begin{cases} \rho(t, \omega_n), & \text{if } \rho(t, \omega_n) \geq \tau \\ 0, & \text{otherwise} \end{cases} \quad (10)$$

where ρ is the occupation measure obtained by means of the "Crazy Climbers" algorithm. The second step considers chaining the relevant ridges into a number of skeletons in such way that maximal points are connected together when moving along time direction. The entire procedure allows for ridge extraction that is essential for system identification.

5.2 Ridge Optimization

Extracted and appropriately chained ridges are often non-smooth and have no physical meaning when natural frequencies are analysed. This is due to noise and/or numerical errors. Ridge optimization needs to be performed to obtain the best ridge solution. In order to achieve this, an assumption concerning the expected skeleton have to be made and some additional physical information have to be taken into account. The first step considered arises from the previously made definition of ridges. Ridges can be found from the areas of concentration of energy, i.e.

$$\varepsilon_1(\omega_n(t)) = - \int H(t, \omega_n(t)) dt \quad (11)$$

where the integral in the above equation defines the sum of TVFRF values along which the skeleton passes. One should note that this integral is multiplied by minus one. This is required by the optimization algorithm used; optimization concerns minimization of penalty function.

Since this method concerns real mechanical systems, smoothness of the ridge is expected. Mathematically this requires minimizing the second penalty function given in the form

$$\varepsilon_2(\omega_n(t)) = \lambda \int |\omega_n'(t)|^2 dt + \mu \int |\omega_n''(t)|^2 dt \quad (12)$$

where λ and μ are arbitrary parameters defining weights of the relevant integrals. Minimization of these integrals leads to more smooth results. The penalty functions - given by Equations (11) and (12) - can be combined to define one penalty function, i.e.

$$\varepsilon(\omega_n(t)) = \varepsilon_1(\omega_n(t)) + \varepsilon_2(\omega_n(t)) \quad (13)$$

that was used in the entire optimization process to extract smooth ridges. The optimization process can utilise genetic algorithms, as demonstrated in [16].

6. NUMERICAL SIMULATIONS

This section demonstrates the capability of the system identification procedure. The focus is on the "Crazy Climbers". Numerical simulations are used to define a simple MDOF system. The 2-DOF damped mass-spring lumped parameter system, illustrated in Figure 1, is simulated using the MATLAB/Simulink computation platform. The sampling frequency was equal to 1 kHz in these numerical simulations.

The system analysed is heavily damped and involves a time-variant mass element; the mass decreased with time. As a result, one of the natural frequencies was expected to vary in time.

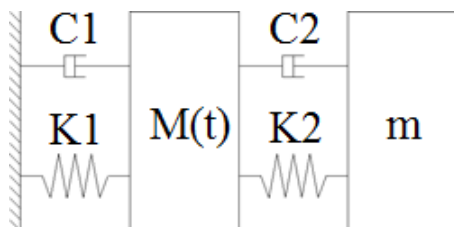


Figure 1. 2-DOF system with time-variant mass

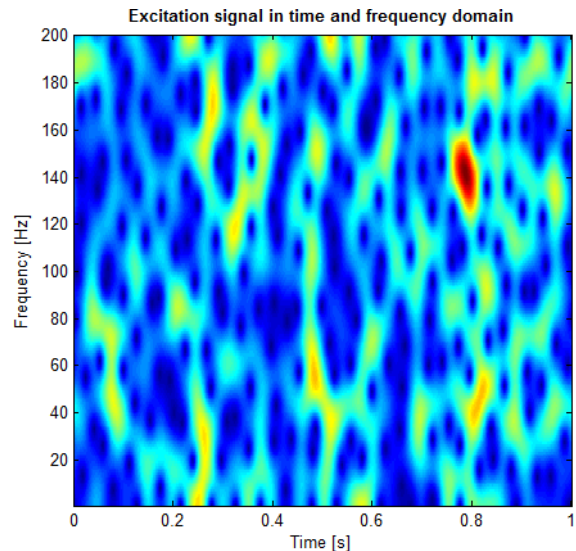


Figure 2. Time-frequency distribution for the Gaussian white noise excitation signal

The Gaussian white noise was used as an input signal to provide a broadband excitation. Figure 2 gives the time-frequency distribution for the excitation signal.

Firstly, the results obtained from numerical simulations were subjected to the classical analysis. The FRF for the system analysed is shown in Figure 3.

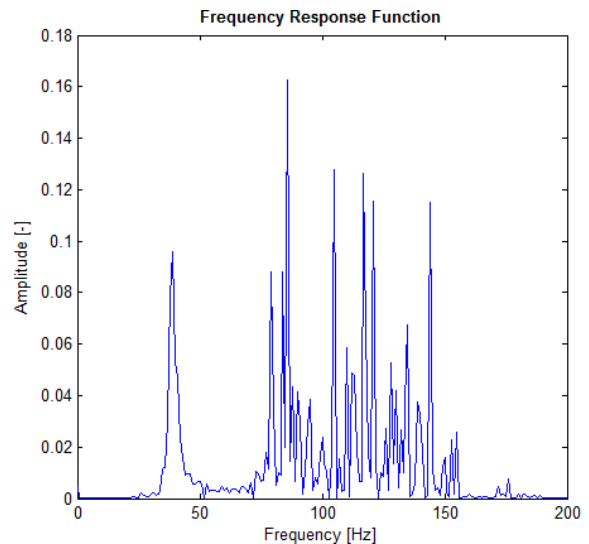


Figure 3. Classical FRF obtained with Fourier transform

The first natural frequency of 40 Hz is clearly exhibited by the FRF function. The second natural frequency is not so obvious due to the time-variant behaviour of the system. Clearly, the classical FRF analysis is not suitable for time-variant systems since natural frequencies are not properly identified.

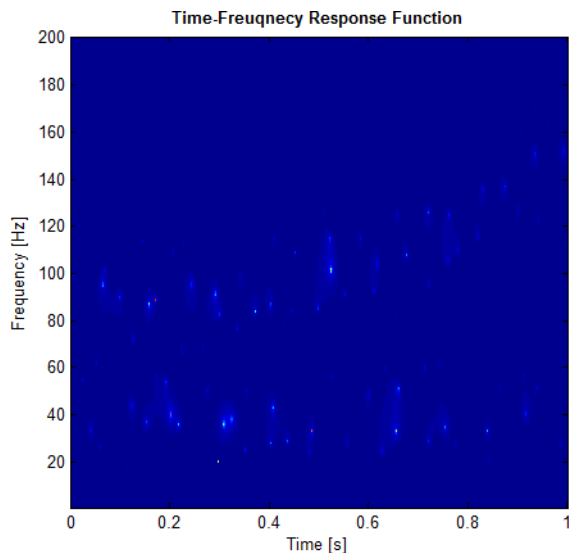


Figure 4. Time-variant FRF for the system shown in Figure 1

The excitation and response data were used to calculate the TVFRF from Equation (7). The result - presented in Figure 4 - is not easy for interpretation. That is why additional post-processing was performed. The "Crazy Climbers:" algorithm - described in Section 5.1 - was used to extract TVFRF ridges. The results of this extraction are shown in Figure 5. Here two vibration modes - represented by two white curves indicating varying natural frequencies - can be clearly identified. The natural frequency of the second mode involved increases with time, as expected. However, both natural frequencies extracted are very bumpy, due to the calculation procedure involved.

The optimization procedure - described in Section 5.2 - was performed to obtain smooth curves. The results are shown in Figure 5 as two red curves imposed on the white noisy characteristics.

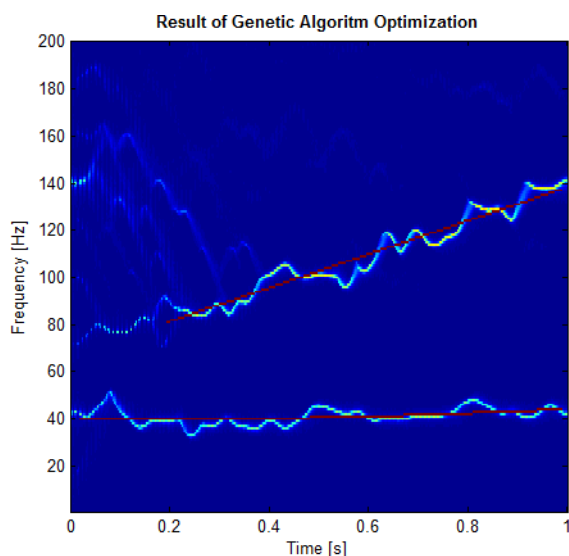


Figure 5. Ridges for the time-variant FRF shown in Figure 4

This clearly shows that the optimization procedure made the relevant ridges smoother and much easier for interpretation. The first natural frequency was estimated between 39 and 41 Hz, whereas the second natural frequency was found to vary between 80 to 140. The results in Figure 5 can be compared with Figure 6 where the so-called "frozen" spectra were used to obtain the natural frequencies of the analysed system. The dynamic behaviour of the system was frozen in time and the classical FRF was obtained. The results in Figure 6 shows that the time-variant behaviour exhibited by the TVFRF - shown in Figure 5 - is revealed properly. Thus the method can be used for identification of time-variant systems.

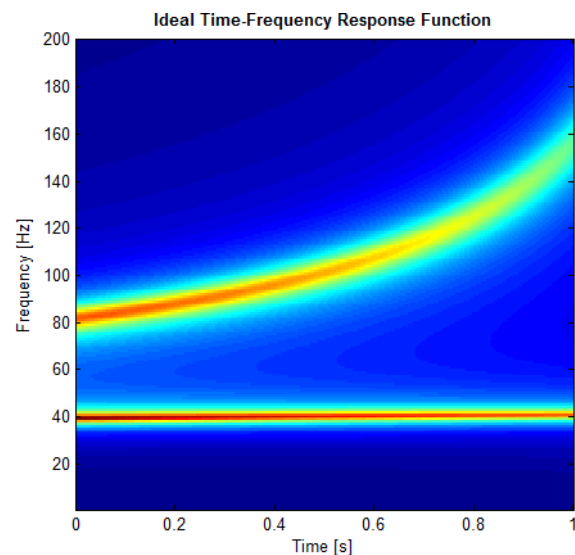


Figure 6. TVFRF obtained with frozen dynamical properties

7. CONCLUSIONS

The TVFRF based on the STFT was used for identification of time-variant systems. The "Crazy Climbers" algorithm together with the skeleton optimization schemes was applied to reveal varying natural frequencies of the simple 2-DOF time-variant system. The results show that the method can be used to reveal time-variant behaviour of the system and to extract its varying natural frequencies. It is important to note that the identification performance of the method have been tested using only one simple simulated example and one identified modal parameter. Future work should involve identification of the remaining modal parameters, i.e. mode shapes and damping. Also, more complex simulated and experimental systems should be investigated.

ACKNOWLEDGEMENTS

The work presented in this paper was supported by funding from the WELCOME research project No. 2010-3/2, sponsored by the Foundation for

Polish Science (Innovative Economy, National Cohesion Programme, EU).

REFERENCES

- [1] S. L. Hahn, *Hilbert transforms in signal processing*. Artech House, 1996.
- [2] N. E. Huang and S. S. Shen, *Hilbert-Huang Transform and Its Applications*. World Scientific, 2005.
- [3] N. Delprat, B. Escudie, P. Guillemain, R. Kronland-Martinet, P. Tchamitchian, and B. Torresani, *Asymptotic wavelet and Gabor analysis: extraction of instantaneous frequencies*, IEEE Transactions on Information Theory, vol. 38, no. 2, pp. 644–664, Mar. 1992.
- [4] P. J. Brockwell, “Time Series Analysis,” in *International Encyclopedia of Education (Third Edition)*, Editors-in-Chief: Penelope Peterson, E. B. Eva Baker and Barry McGawA2 - Editors-in-Chief: Penelope Peterson, and Barry McGaw, Eds. Oxford: Elsevier, 2010, pp. 474–481.
- [5] M. D. Spiridonakos and S. D. Fassois, *An FS-TAR based method for vibration-response-based fault diagnosis in stochastic time-varying structures: Experimental application to a pick-and-place mechanism*,” Mechanical Systems and Signal Processing.
- [6] M. D. Spiridonakos, A. G. Poulimenos, and S. D. Fassois, *Output-only identification and dynamic analysis of time-varying mechanical structures under random excitation: A comparative assessment of parametric methods*, Journal of Sound and Vibration, vol. 329, no. 7, pp. 768–785, Mar. 2010.
- [7] M. D. Spiridonakos and S. D. Fassois, *Parametric identification of a time-varying structure based on vector vibration response measurements*, Mechanical Systems and Signal Processing, vol. 23, no. 6, pp. 2029–2048, Aug. 2009.
- [8] A. G. Poulimenos and S. D. Fassois, *Parametric time-domain methods for non-stationary random vibration modelling and analysis — A critical survey and comparison*, Mechanical Systems and Signal Processing, vol. 20, no. 4, pp. 763–816, May 2006.
- [9] W. J. Staszewski and D. M. Wallace, *Wavelet-Based Frequency Response Function for Time-Variant Systems - an Exploratory Study*.
- [10] K. Dziejdiech, W. J. Staszewski, and T. Uhl, *Input-Output Time-Frequency Analysis of Time-Variant Systems*, presented at the International conference on Uncertainty in Structural Dynamics, Leuven, 2012, pp. 2765–2774.
- [11] W. J. Staszewski, *Identification of non-linear systems using multi-scale ridges and skeletons of the wavelet transform*, Journal of Sound and Vibration, vol. 214, no. 4, pp. 639–658, Jul. 1998.
- [12] W. Lin and M. Xiaofeng, *An adaptive Generalized S-transform for instantaneous frequency estimation*, Signal Processing, vol. 91, no. 8, pp. 1876–1886, Aug. 2011.
- [13] P. M. Oliveira and V. Barroso, *Definitions of Instantaneous Frequency under physical constraints*, Journal of the Franklin Institute, vol. 337, no. 4, pp. 303–316, Jul. 2000.
- [14] R. A. Carmona, W. L. Hwang, and B. Torresani, *Multiridge detection and time-frequency reconstruction*, IEEE Transactions on Signal Processing, vol. 47, no. 2, pp. 480–492, Feb. 1999.
- [15] R. Carmona, W. L. Hwang, and B. Torrésani, *Practical Time-Frequency Analysis: Gabor and Wavelet Transforms With an Implementation in S*. Academic Press, 1998.
- [16] G. Renner and A. Ekárt, *Genetic algorithms in computer aided design*, Computer-Aided Design, vol. 35, no. 8, pp. 709–726, Jul. 2003.



Kajetan DZIEDZIECH is a PhD student in the Department of Robotics and Mechatronics at the AGH University of Science and Technology in Krakow, Poland. His research includes various aspects of structural dynamics, modal analysis and signal processing



Wieslaw J. STASZEWSKI is a Professor of Mechanical Engineering at the AGH University of Science and Technology in Krakow, Poland. He contributed to over 300 research publications in the field of structural dynamics, signal processing, structural health monitoring, smart structures

and materials.



Tadeusz UHL is a Professor of Mechanical Engineering and Head of the Department of Robotics and Mechatronics at the AGH University of Science and Technology in Krakow, Poland. He is an author of over 600 publications in the field of mechatronics, structural health monitoring

and structural dynamics.

PARAMETER IDENTIFICATION OF STEEL - CONCRETE COMPOSITE BEAMS BY FINITE ELEMENT METHOD

Tomasz WRÓBLEWSKI, Agnieszka PEŁKA – SAWENKO, Małgorzata ABRAMOWICZ,
Stefan BERCZYŃSKI

West Pomeranian University of Technology of Szczecin
Faculty of Civil Engineering and Architecture
Address: ul. Piastów 50, 70-311 Szczecin, e-mail: aps@zut.edu.pl

Summary

Steel-concrete composite elements are very often used as main elements of floors or in bridge engineering as main carrying girders. This paper presents computational models and an analysis of natural vibrations conducted on steel-concrete composite beams. Simulation results were compared with experimental research results for beams in groups B1 and B2. In the group of beams B1 a connection that consisted of steel stud connectors was used whereas perforated steel slats were used in group B2. For modelling and calculations, Abaqus platform and Matlab environment were used and the finite element method (FEM) was applied. Each beam model was made in two versions that differ in the approach to modelling connection. In the first modelling approach beam elements were used whereas in the second spring elements were applied. Both models, after parameter identification, provided very good consistency with experimental research results.

Keywords: composite structures, identification, Abaqus, Matlab.

IDENTYFIKACJA PARAMETRÓW STALOWO-BETONOWYCH BELEK ZESPOLONYCH METODĄ ELEMENTÓW SKOŃCZONYCH

Streszczenie

Elementy zespolone stalowo – betonowe są najczęściej wykorzystywane jako główne elementy stropów oraz jako dźwigary nośne w mostach i wiaduktach. Niniejszy artykuł przedstawia modele obliczeniowe oraz analizę drgań swobodnych belek zespolonych stalowo – betonowych. Wyniki porównano z wynikami badań doświadczalnych belek z grupy B1 i B2. W grupie belek B1 zastosowano zespolenie w postaci stalowych sworzni zespalających, w grupie B2 zastosowano zespolenie w postaci stalowych listew perforowanych. Podczas modelowania i obliczeń użyto systemów Abaqus i Matlab, wykorzystując metodę elementów skończonych (MES). Model każdej belki wykonano dwukrotnie inaczej modelując zespolenie, raz wykorzystując w tym celu elementy belkowe, drugi raz z wykorzystaniem elementów sprężystych. Obydwa modele, po przeprowadzeniu identyfikacji ich parametrów, zapewniają wyniki o bardzo wysokiej zgodności z wynikami badań doświadczalnych.

Słowa kluczowe: konstrukcje zespolone, identyfikacja, Abaqus, Matlab.

1. INTRODUCTION

Steel-concrete composite beams are very often used in public space and industrial building engineering as elements of floors or in bridge engineering as main carrying girders. Special attention should be paid in each case to dynamic properties of a designed construction. Over the past decades many studies on steel-concrete composite constructions modelled as continuous or discrete systems have been published [1 - 3]. The finite element method (FEM) is the most frequently used method for three-dimensional modelling [3-7]. The method's primary advantage is its validated reliability and that it can be used on a wide range of calculation platforms, including Abaqus, Nastran and Ansys.

A comprehensive review of the literature on the topic is presented elsewhere [8].

The present study presents computational models and results of natural vibration analysis for two groups of steel-concrete composite beams B1 and B2. In the group of beams B1 a connection that consisted of steel stud connectors was used whereas perforated steel slats were used in group B2. Abaqus platform was used to develop the beam models. The beams were modelled as a spatial system using both solid (reinforced concrete slab) and shell elements (steel beam). The connection between the reinforced concrete slab and the steel beam was modelled in two ways. In the first model denoted as MB, beam elements were used. In the second model denoted as MS, spring elements were applied. Both models assumed that connections can be deflected in

two directions, i.e. perpendicular and parallel directions to the beam axis. Both models, after parameter identification, provided very good consistency with experimental research results.

2. DESCRIPTION OF BEAMS AND EXPERIMENTAL RESEARCH

The analysed beam was 3200 mm in length and consisted of a structural steel section IPE 160 and a reinforced concrete slab (600x60 mm). The structural steel section was made from S235 steel and the slab was made from C30/37 concrete. Owing to differences in type of connection, beams were divided into groups B1 and B2. The analysed beams are presented in Figure 1.

a)

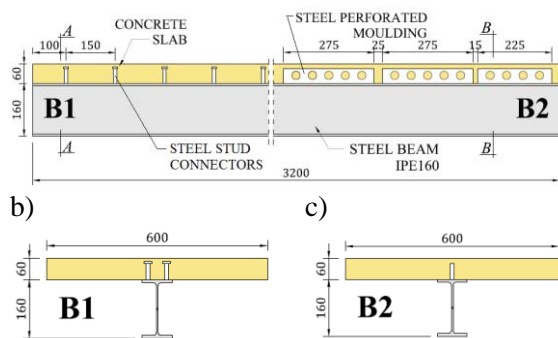


Fig. 1. Composite beams from B1 and B2 group: a) longitudinal view, b) cross-section beam B1, c) cross-section beam B2

Experimental tests were conducted on six composite beams: three from group B1 and three from group B2. Initially, the beams, were tested under static load at the level of 40% of elastic load capacity. The next stage was determination of dynamic characteristics of the beams for a free-end beam schematic. A detailed description of the test stand and test procedure is presented in [3]. Impulse excitation was applied and acceleration in predefined measurement points was measured. A measurement grid and excitation points are presented in Figure 2.

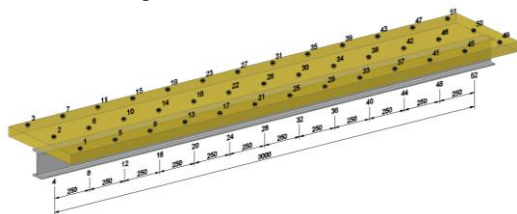


Fig. 2. Grid of measurement points

3. FEM BEAM MODEL

While defining the computational model, it was assumed that the beam has a static schematic with free ends and that its cross-section is constant at all its length. The model was defined on Abaqus platform as a spatial system with independently modelled reinforced concrete slab, steel beam and

connection. At this point of the research study it was decided that an expanded version of the model consisting of shell and solid elements be used. Shell elements (S8R) were used to define a structural steel section IPE 160. A finite element mesh was generated that consisted of 4 elements at the web of the beam, 4 elements along the width of a flange which were spaced every 50 mm along the length of the beam. The reinforced concrete slab was modelled with solid elements of the first order (C3D81). A finite element mesh was generated that consisted of 2 elements along the height of the slab and of 14 elements along the width of the beam (with a thickening in the central area where the slab was connected to the structural steel section) which were spaced every 50 mm along the length of the beam. This division of the beam into finite elements is presented in Figure 3.

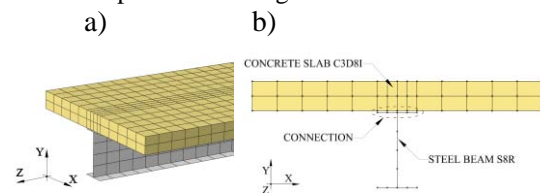


Fig. 3. FEM model of the analysed composite beam: a) view of the beam, b) cross-section

The connection is modelled (Figure 4) between shell element nodes and solid element nodes which are evenly spaced along the length and width of the top flange of the steel section.

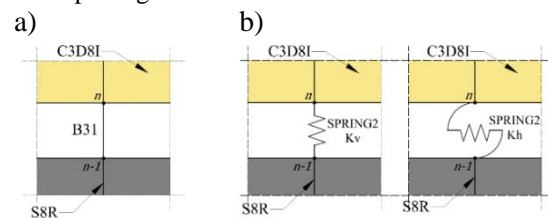


Fig. 4. FEM model of connection for composite beam: a) connection in MB model, b) connection in MS model

B31 beam elements were used in the first model (MB model). SPRING2 elements were used in the second model (MS model). Stiffness of the connection in two directions was assumed. The stiffness along the horizontal direction (the axis z) was denoted as K_h and that in the vertical direction (the axis y) was denoted as K_v . In MB model, the stiffness of connection was changed by changing parameters that defined B31 beam elements, i.e. a change of the cross-sectional area A reflected a change in stiffness K_v whereas a change of the moment of inertia J reflected a change in stiffness K_h . In MS model two independent groups of spring elements SPRING2 were used. The first group was responsible for stiffness K_h (along the axis z) while the second group was responsible for the interaction between steel and concrete along the

vertical direction (the axis y) - stiffness K_v . The stiffness of connection in the axis x (horizontal, perpendicular to the beam axis) was neglected owing to the scope of analysed modes of the beam vibrations.

4. DYNAMIC EQUATION OF MOTION

The dynamic equation of motion can be written as

$$M\ddot{q} + C\dot{q} + Kq = P \quad 4.1$$

where M is inertia matrix, C is damping matrix, K is the matrix of system stiffness, P is the vector of outside forces acting on the system, and q is the vector of generalised coordinates. For free vibration Equation 4.1 takes the following form

$$M\ddot{q} + Kq = 0 \quad 4.2$$

The frequency and the mode vector of natural vibration for the modelled composite beam can be found using Equations:

$$\det(K - \omega^2 M) = 0 \quad 4.3$$

$$(K - \omega^2 M)\Phi = 0 \quad 4.4$$

where ω is the frequency of natural vibration.

5. PARAMETER IDENTIFICATION

The first identified element of the model was substitute Young’s modulus of the reinforced concrete slab E_c which accounted for the influence of the slab’s longitudinal reinforcement. The second and the third identified elements were the stiffness of connection K_h and K_v . In MB model the stiffness of connection was indirectly identified by determination of cross-sectional area A and moment of inertia J for B31 elements.

The best fit of computational and experimental free vibration frequency values was assumed to be consistency criterion. Consequently, the minimised index S can be given by:

$$S = \sum_{i=1}^5 \left(\frac{f_{i,flex}^{exp} - f_{i,flex}^{com}}{f_{i,flex}^{exp}} \right)^2 + \left(\frac{f_{1,long}^{exp} - f_{1,long}^{com}}{f_{1,long}^{exp}} \right)^2 \quad 4.5$$

where S is the sum of squares of relative deviations of computational and experimental frequencies. The first five modes of flexural vibrations were represented by $f_{i,flex}$ and the frequency of fundamental mode of axial vibrations by $f_{1,long}$.

To optimise the identification process of the three above described parameters, the calculation programs were connected to create a calculation loop. The identification process was controlled in Matlab environment. Using a script developed in Python language, Matlab generated a parameterised model which was then sent over to be analysed in Abaqus. Analysis results were sent back to Matlab where optimisation procedures were used to decide what possible changes were to be introduced to the identified parameters. The procedure was repeated until the minimum of index S was reached. The process was fully automated.

Tables 1 and 2 present a comparison of experimental and computational results of free vibration frequencies determined for five modes of flexural vibrations and one mode of axial vibrations.

Table 1. Beam B1. Identification results – frequencies, relative errors, identified parameters

Mode of vibration	$f_{i,exp}$ [Hz]	MODEL MB		MODEL MS	
		$f_{i,com}$ [Hz]	Relative errors	$f_{i,com}$ [Hz]	Relative errors
1 _f	74,9	75,4	0,7	74,8	0,1
2 _f	173,5	172,1	-0,8	173,4	0
3 _f	274,8	275,1	0,1	276,7	-0,7
4 _f	375,4	375,5	0	374,6	0,2
5 _f	474,9	475,9	0,2	471,1	0,8
1 _a	593,9	594,5	0,1	593,9	0
R	S	1,19E-04	R	S	1,19E-04
E	E_c [N/m ²]		E	E_c [N/m ²]	
S]	2,94E+10	S]	2,94E+10
U	A_{zesp} [m ²]	1,26E-06	U	K_v	3,83E+07
L			L	[N/m]	
T	$J_{y,zesp}$ [m ⁴]	1,01E-10	T	K_h	
S			S	[N/m]	4,64E+07

Table 2. Beam B2. Identification results – frequencies, relative errors, identified parameters

Mode of vibration	$f_{i,exp}$ [Hz]	MODEL MB		MODEL MS	
		$f_{i,com}$ [Hz]	Relative errors	$f_{i,com}$ [Hz]	Relative errors
1 _f	74,9	76,1	0,02	75,3	0,6
2 _f	173,5	178,4	0,03	179,4	0,4
3 _f	274,8	287,8	0,05	290,4	-0,1
4 _f	375,4	392,9	0,04	394,5	-0,3
5 _f	474,9	496,3	0,04	494,4	0,2
1 _a	593,9	593,4	0,00	586,1	0,5
R	S	7,50E-03	R	S	8,61E-05
E	E_c [N/m ²]		E	E_c [N/m ²]	
S]	2,94E+10	S]	2,94E+10
U	A_{zesp} [m ²]	5,63E-06	U	K_v	1,39E+08
L			L	[N/m]	
T	$J_{y,zesp}$ [m ⁴]	1,25E-10	T	K_h	
S			S	[N/m]	3,40E+08

The next step was an analysis of the modes of free vibrations. The points in the computational model, for which modal vector components were determined, were assumed so that they overlapped with the measurement grid used in the experimental research - see Figure 5. Vector components in the vertical direction (the axis y) were analysed.

A comparison of corresponding experimental and computational modal vectors for the first four modes of flexural vibrations was conducted using MAC (Modal Assurance Criterion).

$$MAC = \frac{(\psi_{exp}^H \psi_{com})(\psi_{com}^H \psi_{exp})}{\psi_{exp}^H \psi_{exp} \psi_{com}^H \psi_{com}} \quad 4.6$$

where ψ_{exp} is the modal vector of the modes of vibration obtained in the experimental research and ψ_{num} is the modal vector determined with the computational model.

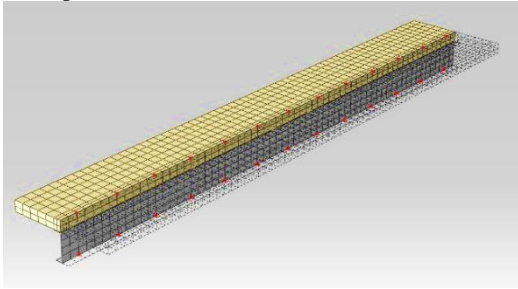


Fig. 5. The measurement grid used in the experimental research

A comparison of experimental and computational (MB model) modal vectors corresponding to the second flexural mode of vibrations is presented in Figure 6.

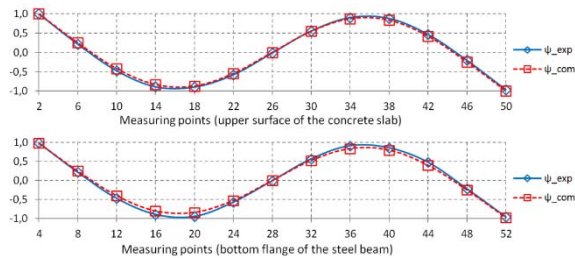


Fig. 6. Comparison of normalized modal vectors, second mode of flexural vibrations, MB model, vertical direction - axis y

MAC values for five flexural mode of vibrations for MB and MS models are presented in Table 3.

Table 3. MAC values for MB and MS models

BEAM	B1		B2	
	MB	MS	MB	MS
1 _f	1,00	1,00	1,00	1,00
2 _f	1,00	1,00	1,00	1,00
3 _f	0,99	0,98	0,98	0,98
4 _f	0,99	0,93	0,98	0,98
5 _f	0,95	0,81	0,67	0,57

6. CONCLUSIONS

The developed FEM models of steel-concrete composite beams B1 and B2 are highly consistent with real beams. The identification of selected parameters provided a very good fit of free vibration frequencies (a precision of ~1%). A further analysis of modal vectors confirmed their high consistency (MAC ~1.0). Combining computation programs into an automated computation loop optimised and accelerated the process of parameter identification. A comparison of two connection modelling techniques - MS and Mb models - revealed that MS better reflects the behaviour of a

real structure. Using MS model it is also possible to directly define connection stiffness whereas in MB model it is possible only through indirect modifications of the values of cross-sectional area A and moment of inertia J for B31 elements.

The time required for solving an individual task was much shorter for MS model which is important bearing in mind that during identification process every model is repeatedly recalculated.

The identified models were used to analyse beams with locally damaged connection. Simulation results are being analysed.

The future plans include a development of simplified FEM models of composite beams using shell elements for modelling the concrete part and beam elements for modelling the steel part.

7. ACKNOWLEDGMENTS

This research was carried out with the financial support of the Ministry of Science and Higher Education in Poland in the years 2010–2012.

LITERATURE

- [1] Biscontin G., Morassi A., Wendelp.: *Vibrations of steel-concrete composite beams*. Journal of Vibration and Control, 6(2000), 691-714.
- [2] Dilena M., Morassi A.: *A damage analysis of steel-concrete composite beams via dynamic methods: Part II. Analytical models and damage detection*. Journal of Vibration and Control, 9(2003), 529-565.
- [3] Berczyński S., Wróblewski T.: *Vibration of steel-concrete composite beams using the Timoshenko beam model*. Journal of Vibration and Control, 11(2005), 829-848.
- [4] Pi Y. L., Bradford M. A., Uy B.: *Second order nonlinear inelastic analysis of composite steel-concrete members. II: Applications*. Journal of Structural Engineering, 132 (2006)5, 762–771.
- [5] Thevendran V., Shanmugam N. E., Chen S., Richard Liew Journal Y.: *Experimental study on steel-concrete composite beams curved in Plan*. Finite Elements in Analysis and Design, 32(2000), 125–139.
- [6] Prakash A., Anandavalli N., Madheswaran C. K., Rajasankar Journal, Lakshmanan N.: *Three Dimensional FE Model of Stud Connected Steel-Concrete Composite Girders Subjected to Monotonic Loading*. International Journal of Mechanics and Applications, 1(2011)1, 1-11.
- [7] Mirza O., Uy B.: *Behaviour of headed stud shear connectors for composite steel-concrete beams at elevated temperatures*. Journal of Constructional Steel Research, 65(2009), 662–674.
- [8] Wróblewski T., Pełka-Sawenko A., Abramowicz M., Berczyński S.: *Modeling and analysis of free vibration of steel-concrete composite beams by finite element method*. Advances in Manufacturing Science and Technology 36(2012)4, 85-96.

STRUCTURE'S DAMAGE DETECTION SUPPORTED BY CONTACT AND CONTACT-LESS GLOBAL METHODS

Piotr KOHUT^a, Krzysztof HOLAK^b, Krzysztof MENDROK^c, Wojciech MAJ^d
AGH University of Science and Technology, Department of Robotics and Mechatronics,
Al. A. Mickiewicza 30, 30-059 Krakow, Poland
^apko@agh.edu.pl; ^bholak@agh.edu.pl; ^cmendrok@agh.edu.pl; ^dwojtekm@poczta.fm

Abstract

The paper briefly describes two Structural Health Monitoring (SHM) systems applied for damage detection in civil engineering structures: the vision-based system for in-plane measurement of a structure's displacement fields, and vibration-based SHM system with modal filter as a core component.

In vision-based system, the deflection curve is obtained as a result of analysis of two images of the construction: the reference one and the one acquired after application of the load. A modal filter is also an excellent indicator of damage detection, with such advantages as low computational effort, ease of automation and low sensitivity to environmental changes. To apply this method in a real SHM system, the measuring diagnostic unit has been designed and built. The system installed on the test stand consisted of a network of a sensors, needed by modal filtration system, placed in selected area of the structure. Additionally a linear transducer for measurement of deformation of the lower beam of the structure under investigation was used. The paper shows the results of their laboratory tests on truss structure. The experimental results obtained by both systems were compared.

Keywords: digital image correlation, image registration, vision systems, optical measurement system, deflection measurement, modal filter, damage detection, laboratory testing, truss structures.

WYKRYWANIE USZKODZEŃ KONSTRUKCJI Z WYKORZYSTANIEM GLOBALNYCH METOD KONTAKTOWYCH I BEZKONTAKTOWYCH

Streszczenie

Artykuł opisuje dwa systemy monitorujące stan konstrukcji (SHM) wykorzystane do wykrywania uszkodzeń konstrukcji inżynierii lądowej: system wizyjny przeznaczony do dwuwymiarowych pomiarów pól przemieszczeń konstrukcji, oraz system oparty na filtracji modalnej.

W systemie wizyjnym krzywa odkształcenia uzyskiwana jest w wyniku analizy dwóch zdjęć obiektu: obrazu odniesienia oraz zdjęcia obiektu obciążonego. Filtr modalny jest doskonałym wskaźnikiem detekcji uszkodzeń. Jego zaletą są niskie wymagania obliczeniowe, łatwość automatyzacji oraz mała wrażliwość na zmiany środowiskowe. Metoda ta została opisana i przetestowana numerycznie przez autorów. Aby zastosować ją w rzeczywistym systemie SHM zaprojektowano specjalny moduł diagnostyczny – pomiarowy. System zainstalowany na stanowisku składał się z grupy czujników wymaganych przez system filtracji modalnej umieszczonych w wybranym obszarze obiektu. Ponadto wykorzystano czujnik LVDT do pomiaru odkształcenia liniowego dolnej belki. Systemy zostały przetestowane na rzeczywistych konstrukcjach. Artykuł przedstawia wyniki testów laboratoryjnych na laboratoryjnej konstrukcji ramowej. Wyniki eksperymentu uzyskane za pomocą obu systemów zostały ze sobą porównane.

Słowa kluczowe: cyfrowa korelacja obrazów, rejestracja obrazów, system wizyjny, optyczny system pomiarowy, pomiar odkształceń, filtr modalny, wykrywanie uszkodzeń, testowanie laboratoryjne, struktury kratowe.

1. INTRODUCTION

Structural Health Monitoring (SHM) is an emerging field of technology that involves the integration of sensors, data transmission, processing and analysis for detection, as well as localization and assessment of damage which can lead to its failure in

the future [1, 2]. In general, SHM methods can be divided into two groups: local and global ones. The second group can be applied if a global change in the geometry of a structure can be observed. In practice, the most commonly used methods of damage detection are based on the analysis of

variations in various dynamic properties caused by damage [3, 4].

One of the techniques from this group is an application of modal filtration to the object characteristics for damage detection purposes [21]. In this method system response is divided into components related with different modal shapes. If any change in object structure occurs, then a significant change in system response filtered by modal filter will be observed. This effect can be very useful for object damage detection purposes.

However, sometimes it is extremely difficult to attach sensors to a structure because of the geometrical constraints. What is more, the excitation of large structures can be costly and difficult. The acquisition of static deflection requires much less effort, which makes the damage detection methods based on changes in deflection curves more attractive for practical use [5-13]. Therefore, a lot of non-contact measurement techniques have been developed. The vision systems can be a good alternative to other types of transducers. They are easy-to-use, accurate and low-cost tools which can be applied to deflection measurements.

In this paper, two developed systems based on above mentioned principles are presented: the vision system for in-plane measurement of a civil engineering structure's displacement fields, and modal filtration based damage detection system.

The principle of the vision method is calculation of object's point displacement by means of a normalized cross correlation coefficient. Perspective distortions of the construction's image are removed by means of homography mapping, which allows two photographs of the object to be taken from two distinct points in space.

Second of mentioned systems is based on global change detection in the object. It consists of group of sensors located on examined object, and uses them to gather it's characteristics (PSD or FRFs). Those characteristics are then filtered by appropriately tuned modal filters, and used for damage index estimation. This approach was presented for the first time by Deraemacker and Preumont in 2006 [21].

There are discussed developed methodology and software tool for both systems. As a key study, girder deflection under a load has been investigated.

The experimental results obtained by both systems were compared.

2. VISION IN-PLANE DEFLECTION MEASUREMENT METHOD

In vision system, the deflection curve is obtained as a result of analysis of two images of the construction: the reference one and the one acquired after application of the load.

The proposed vision based method of the in-plane deflection measurement consists of three steps: image rectification, displacement field measurement and scaling. The first step of the

method is optional and can be performed if the images of the structure are taken from two distinct points in space. The rectified photograph can be spatially overlaid with the reference image. In the next step, the image of the construction's plane is divided into intensity patterns. The set of corresponding patterns is identified on the reference image and images of the structure deformed under the load by means of the normalized cross correlation coefficient (NCC). The deflection curve is computed as the difference between positions of the corresponding image patches on two images. In the last step, the scale coefficient is calculated from objects with known geometric dimensions.

IMAGE RECTIFICATION

Homography transformation [16] has been introduced for reduction of perspective distortions which enabled a deflection's course to be obtained from images of a construction taken from distinct points of view. If coplanar corresponding points' \mathbf{x} and \mathbf{x}' positions are given in homogenous coordinates, homography can be represented by a 3-by-3 matrix denoted as \mathbf{H} . The transformation which maps coplanar points on the image with projective distortions to corresponding points on the reference image is given by:

$$\mathbf{x} = \mathbf{H} \mathbf{x}' \quad (1)$$

The homography matrix \mathbf{H} is computed from a set of corresponding points. Four pairs of coplanar corresponding points are necessary and sufficient to compute matrix \mathbf{H} if no three of them are co-linear. The plane of the construction is rectified when all image points are transformed by homography mapping [16]. Results of the rectification performed on the image of the lab setup are presented in Figure 1.

DISPLACEMENT MEASUREMENT

In the process of deflection measurement, the reference image of an unloaded construction is divided into random speckle intensity patterns [1,2]. Each of the patterns is matched with corresponding pixel subsets on the image of the loaded structure by means of the NCC coefficient (2).

$$NCC(u,v) = \frac{\sum_{x,y} (f_n(x,y) - \bar{f}_n)(f_d(x-u,y-v) - \bar{f}_d)}{\sqrt{\sum_{x,y} (f_n(x,y) - \bar{f}_n)^2 \sum_{x,y} (f_d(x-u,y-v) - \bar{f}_d)^2}} \quad (2)$$

Where:

$f_n(x,y)$ – intensity value for a pixel with coordinates (x, y) on the reference image;

\bar{f}_n – mean value of the intensity function of the pattern on the image before deformation;

$f_d(x-u,y-v)$ – intensity value for a pixel with coordinates (x, y) on the image after deformation;

\bar{f}_d – mean value of the intensity function in the analyzed region after deformation;

x, y – position of the pattern on the reference image;
 u, v – displacement of the pattern between two images;

The displacement vector is computed as the difference between positions of the pattern on two images. The method performed on each of the points of interest provides a complete course of deflection.



Fig. 1. Homography transformation: the reference image, the image with perspective distortion (taken by the second camera), the second image after rectification

SYSTEM CALIBRATION AND SCALING

The full camera calibration is carried out by means of the method developed by Zhang [17] to obtain the intrinsic parameters as well as coefficients for lens distortions correction. The chessboard planar pattern with black and white squares, an even number of rows and odd number of columns is used. The scale coefficient $\alpha_{\text{mm/pix}}$ is computed from an object on the scene with known geometric dimensions, a planar circular marker or the certified length standard.

DEVELOPED SOFTWARE TOOL

The developed software (Figure 2) enables construction deflection measurement using digital SLR cameras for remote image acquisition and provides image processing algorithms to calculate the displacement field. ED-SDK libraries provided by Canon have been used to control one or more cameras in the system. Two modes of operation are available: on-line and off-line. In the first case, the user specifies the date and number of measurements and then the system works fully automatically carrying out the image acquisition and deflection measurement. The off-line mode provides analysis of the images stored on hard disk.

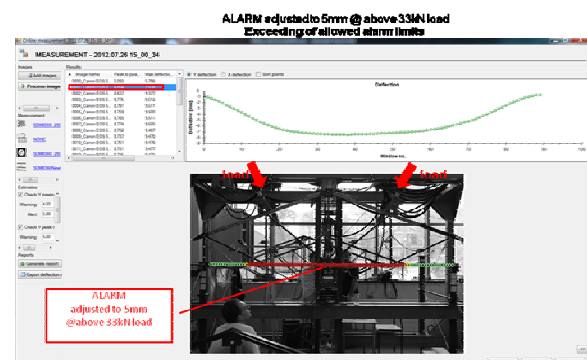


Fig. 2. Wiz2D Deflection - example form conducted tests during damage of the structure

The result browser module carries out the visualization of calculated curves of deflection and report generation in popular formats, like PDF, XML, CSV and TXT. An additional feature of the software is detection of exceeding the allowed level of a deflection and the sending of alerts to a client by an e-mail.

3. MODAL FILTRATION AS VIBRATION BASED METHOD OF DAMAGE DETECTION

The vibration based methods are one of the widest described damage detection methods [24]. One of the techniques from this group is an application of modal filtration to the object characteristics. A modal filter is a tool used to extract the modal coordinates of each individual mode from a system's output [25, 26]. It decomposes the system's responses into modal coordinates, and thus, on the output of the filter, the frequency response with only one peak, corresponding to the natural frequency to which the filter was tuned, can be obtained. Very interesting way of using modal filtering to structural health monitoring was presented by Deraemaeker and Preumont in 2006 [21] Frequency response function of an object filtered with a modal filter has only one peak corresponding to the natural frequency to which the filter is tuned. When a local change occurs in the object – in stiffness or in mass (this mainly happens when damage in the object arises), the filter stops working and on the output characteristic other peaks

start to appear, corresponding to other, not perfectly filtered natural frequencies. On the other hand, global change of entire stiffness or mass matrix (due to changes in ambient temperature or humidity) does not corrupt the filter and the filtered characteristic has still one peak but slightly moved in the frequency domain. The method apart from the earlier mentioned advantages, which results from its low sensitivity to environmental conditions has very low computational cost, and can operate in autonomous regime. Only the final data interpretation could be left to the personnel. This interpretation is anyhow not difficult and it does not require much experience. Another advantage of the method results from the fact that it can operate on the output only data.

GENERAL ASSUMPTIONS

As it was mentioned in the previous section the modal filtration can be a great tool for damage detection and further for structural health monitoring. For this reason the authors decided to implement as a practical measuring – diagnostic system. Its main assumption was that it should be completely independent. It means that the potential user should be able to perform full diagnostic procedure without necessity of usage of any additional measuring device or software. To fulfill above requirement the original 16-teen channel measuring – diagnostic unit MDU was designed and the dedicated modal analysis and modal filtration software was written. Generally the system composed of both hardware and software is supposed to work in one of the three modes:

- I. Operation in dynamic signal analyzer mode for the purposes of the modal testing. In this mode the modal filter coefficients are estimated for the reference structure.
- II. Operation in diagnostic mode:
 - Acceleration / displacement of vibration measurements,
 - Selected characteristics estimation (FRFs or PSDs),
 - Modal filtration of the above characteristics,
 - Damage index calculation,
 - Visualization of the filtered characteristics,
- III. Operation in monitoring mode:
 - Periodical acceleration / displacement of vibration measurements,
 - Selected characteristics estimation (FRFs or PSDs),
 - Modal filtration of the above characteristics,
 - Damage index calculation,
 - Reporting of the object to the central unit.

MEASURING DIAGNOSTIC UNIT

From technical point of view the diagnosis process is divided into a few basic steps:

- simultaneous synchronous acquisition of analog signal (converted into digital domain) from 16 channels.
- digital signal processing applied to measured signal
- output processing results

The block diagram of MDU is described in Figure 3.

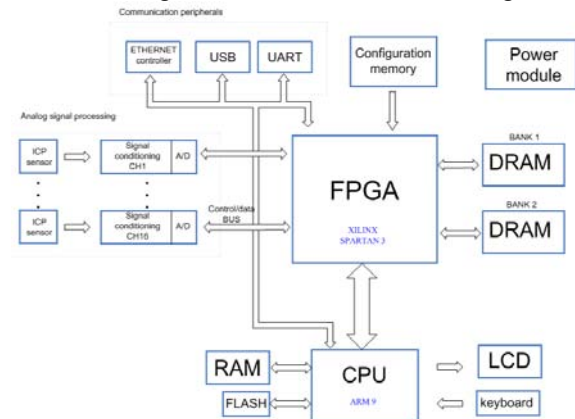


Fig. 3. Block diagram of design device

Diagnostic device contains of two fully independent and connected with each other modules: CPU and FPGA modules. The CPU module is included for control purposes – it implements user interface with some peripheral devices like keyboard, LCD display and communication peripherals. Using this interface it is possible i.e. to set gain or select required analog filter in each of 16 analog signal processing modules, or to start diagnostic process.

The FPGA module contains all logic modules needed for implementation of required digital signal processing. It is “seen” by CPU module as another peripheral device which can execute commands (like start data processing command) and send processing results.

In other words, the FPGA module act as a coprocessor, which shortens time necessary for full measure cycle and therefore allow for power savings.

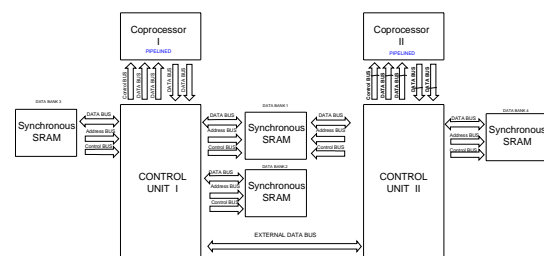


Fig. 4. FPGA processing module block diagram

The FPGA data processing module is designed using multi path, pipelined architecture (figure 4), which can be easily extended to support more signal channels, and less processing time as required.

MDU also contains non-volatile memory for data recording purposes.

The MDU can be accessed via Ethernet or USB, which is needed in system calibration phase, or to read remotely processed results. Analog signal processing module is shown in figure 5.

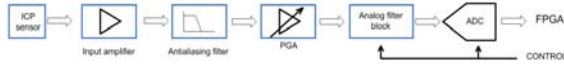


Fig. 5. Analog part of the circuit measuring

The input analog signal is delivered from ICP accelerometer sensors mounted on examined object. ICP signal standard is based on 4 – 20 mA current signal transmission, which main advantage is the ability of transmitting signal (with 1 kHz frequency band wide) without any distortion at ranges of 100 m and more.

Analog signal processing circuit also contains programmable gain amplifier (PGA) for three different values of gain: 1, 10 and 100. It also includes a set of analog antialiasing filters (with cutoff frequency set to: 10Hz, 50Hz, 250Hz, 500Hz and 1kHz) and 24-bit ADC converter.

MDU contains 16 identical analog signal processing channels, each for every analog input. The ADCs of every data channel are configured to provide synchronous signal acquisition, so that every sample gathered by first ADC is accurately synchronized in time with those coming from other ADCs.

With this hardware solution it is possible to detect and continuously monitor ICP status (whenever the input is shorted, opened or work in it is normal working conditions). It is also possible to detect input signal overshoots, so that device will not take such distorted data into account during measures.

DEDICATED SOFTWARE

The main goal of the software written for the described SHM system is the estimation of the modal filter coefficients. For this purpose, the application provides the following functionalities:

- Geometrical model definition of the tested object.
- Measurement points definition, namely the assignment of specific points of a geometric model to the sensors placed on an object.
- Execution of measurement and presentation of the results (time histories, PSD, FRF and coherence), and data archiving.
- Execution of modal analysis by:
 - calculation of stabilization diagram,
 - estimation and visualization of mode shapes for selected poles,
 - estimation of modal filter coefficients and visualization of filtration results.

The application was created in the .Net Framework 3.5 environment with use of additional external libraries:

- Developer Express v9.1 (tables and standard application controls)
- Steema TeeChart for .Net v3 (charts)
- Intel IPP (signal spectrum calculation)

All calculations related to the modal analysis are performed by the Matlab engine. The application provides the ability to debug these functions from Matlab level. For this reason, at the user-specified location, mat-files are stored that contain input parameters for the appropriate Matlab functions. In Figure 14 the graphical user interface of described software allowing for impulse modal testing and mode shape visualization control is presented.

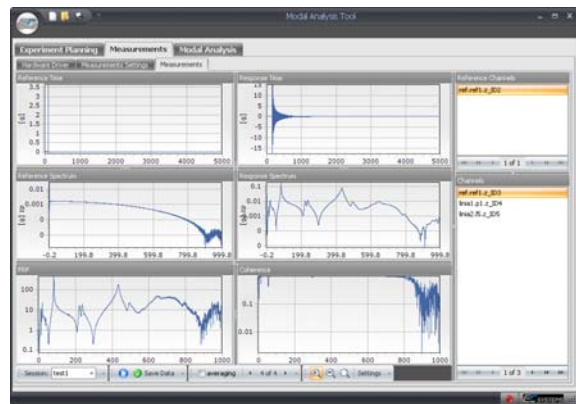


Fig. 6. GUI of described software

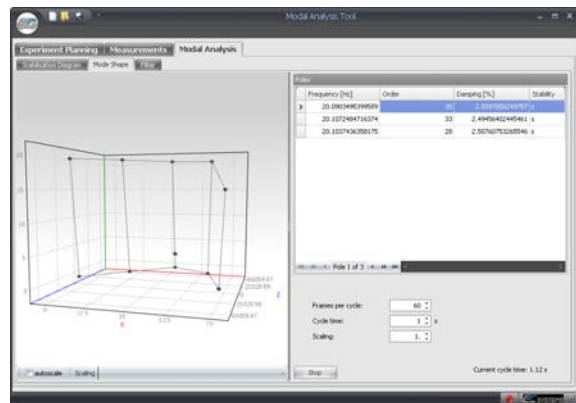


Fig. 7. GUI of described software

It was assumed that in order to fluently visualize the mode shapes it is necessary to refresh screen with a minimum speed of 30 fps. There are not available on the market sufficiently effective controls to allow the visualization and animation of 3D models with the assumed speed. Therefore, implementation of such control was done by using the XNA environment. The control uses a graphics accelerator which allows for refresh at 60 fps at 10,000 points of geometrical model.

4. EXPERIMENTAL SET-UP AND PROGRAM OF TESTS

During the experiment a load was applied on a single girder shown in Figure 7 mounted on a specially built test stand [14, 15]. The experiment was carried out until the damage of the girder. Actuators, two hydraulic jacks, were used to apply the load on the truss. Experimental conditions imitated the real working conditions of the trusses typically used in roof constructions. Jack's mounting points on the construction were placed symmetrically in the middle of the upper truss members. During the experiment load cycles were applied to the construction. In each cycle load was slowly increased in several steps and later removed in the same manner.

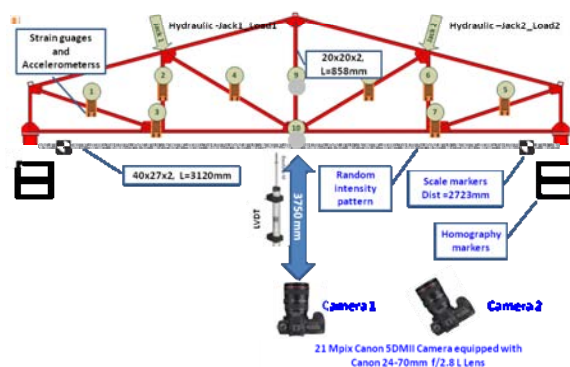


Fig. 8. Experimental set-up: a) transducer's and camera's arrangement on the girder. Dimensions of the bottom truss member: 40x27x3120 mm, dimensions of the vertical truss: 20x20x85 mm

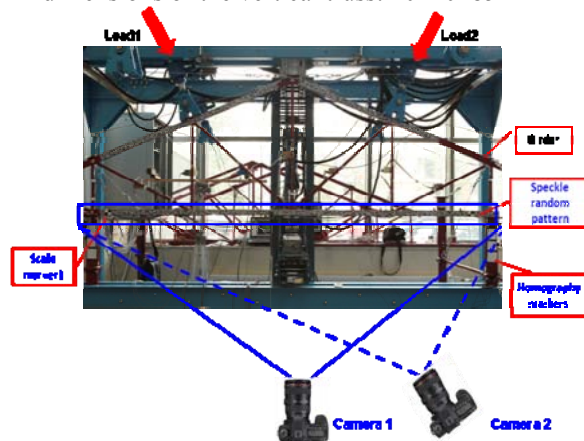


Fig. 9. Experimental set-up: camera's, scale markers, homography markers arrangement on the girder

Deflection of the bottom truss of the girder was measured by the developed vision system (Figure 8). The truss of length 3120 mm and member's cross section 40x27 mm was used. The beam was fixed at both ends. The texture characterized by random distribution of diameters and positions of oval patterns was stuck on the analyzed truss surface. The set of rectangular markers necessary for homography matrix computation was placed on the

both side of the truss. Photographs of the construction were acquired by a system of two digital Canon 5D Mark II cameras with 21.1 MPix image resolution and Canon 24-70mm f/2.8L lens with focal length $f \approx 39$ mm adjusted. The position of the cameras were fixed. One of the cameras had its optical axis perpendicular to the plane of the construction. The reference images were obtained by that camera. The second camera was translated and rotated with respect to the first one and used for calculation of the deflection field from the images after application of rectification. The distance d_0 of the reference camera amounted to 3750 mm. The distance d_1 between the cameras was 960 mm and the angle between the optical axes of the first and the second camera amounted to 14.5 degrees. To calculate scale coefficient (0,5873 mm/pixel) the two crash-test markers were stuck on the truss at a known distance, 2723.5 mm. Regarding scene illumination, there were extremely changeable natural lighting conditions with sunlight and cloudy variations.

In order to detect object damages with modal filtering system, a set of vibration sensors were installed on bottom beam of the truss as shown in Figure 9. Each sensor is connected directly to the measurement system, so that the truss state was continuously monitored. A significant advantage of this approach is that it is not necessary to place a large number of sensors on examined object even if it is large. The user can place only a few sensors evenly distributed on the object. What is more, position of each sensor cannot be changed during measurements, as it would affect damage detection quality [27].

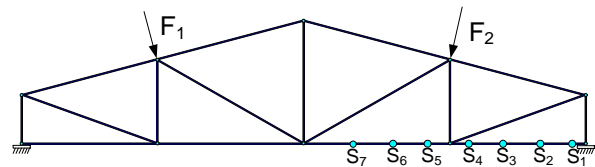


Fig. 10. Experimental set-up: Object of tests with sensors mounted on it

As a matter of fact this method can be successfully used in applications where the measures are performed periodically. In this case sensors doesn't need to be installed permanently, however user have to ensure that every sensor is mounted exactly in the same point of the object as it was during reference measure. This can be achieved by using dedicated spacers (between object and sensors) mounted permanently on tested object.

5. VISION-BASED MEASUREMENT RESULTS

The repeatability of the vision based measurement method has been carried out for both cameras in the system. There were no significant difference of the standard deviation of the measured

displacement between the data obtained using reference camera and the camera the data computed after rectification. There was decrease of the repeatability observed with the increasing value of the load. The results are presented in table 1.

Table 1. Repeatability of the vision based measurement method

Force [kN]	Reference [mm]	Rectification [mm]
5	0.0085	0.0085
10	0.0096	0.0102
20	0.0129	0.1278
25	0.0166	0.0209
30	0.0161	0.0191
35	0.0143	0.0157

COMPARISON OF THE VISION BASED SYSTEM WITH LVDT MEASUREMENT

The displacement computed in one point (Fig.10) by the vision system was compared with the value obtained by a contact measurement method using LVDT sensor. The absolute difference between two results ranged from 0.099 mm to 0.386 mm. The absolute difference between displacements registered by two systems is summarized in table 2. The figure 3 shows the displacement in a point as a function of applied load for vision system as well as contact type sensor.

Table 2 Absolute difference between vision and contact measurement

Force [kN]	Difference [mm]
5	0.1719
10	0.2623
20	0.2517
25	0.0292
30	0.3860
35	0.0997

DAMAGE DETECTION BY THE DEVELOPED VISION SYSTEM

The developed vision system monitors the state of the structure and informs the user when the measurement estimates has been exceeded and a message can be sent by email. In this matter the developed software tool enables damage detection based on the comparison measured data with the adjusted thresholds of the warning and alarm values. The visualization of the warning and alarm threshold exceed are illustrated in the Figure 11. Yellow-colored points represent warning and exceeded deflection values of the measurement points, while red-colored points indicate the alarm and exceeded deflection values of measurement points calculated by digital image correlation method.

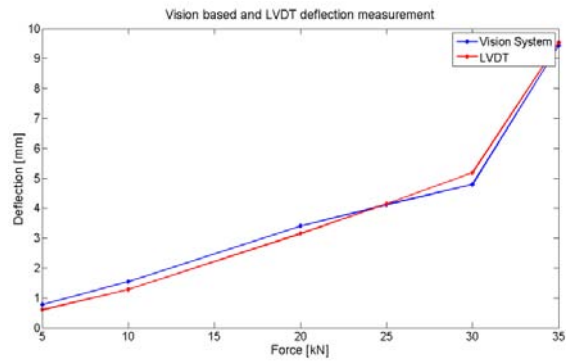


Fig. 11. The displacement in a point as a function of applied load for the vision system as well as contact type sensor

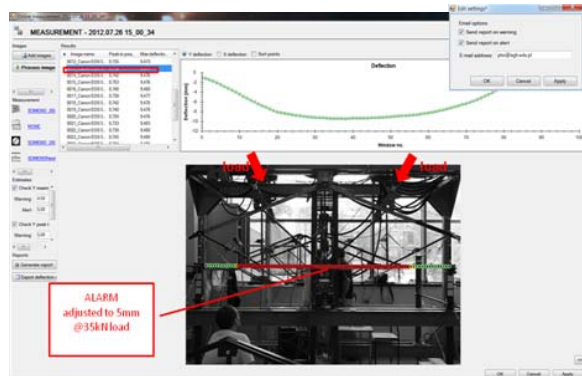


Fig. 12. Example of alarm thresholds' value exceeding (red color) indicating damage of the girder

6. VIBRATION – BASED MEASUREMENT RESULTS AND COMPARISON WITH VISION SYSTEM RESULTS

During the experiment, load was slowly increased in several steps, until the first symptoms of damage appeared. As an input to the diagnostic procedure based on modal filter only one type of characteristics was considered: FRFs. All the results were evaluated with use of damage index proposed in [28]:

$$DI = \frac{\int_{\omega_s}^{\omega_f} |x_i(\omega) - x_{ref}(\omega)|^2 d\omega}{\int_{\omega_s}^{\omega_f} x_{ref}(\omega)^2 d\omega} \tag{3}$$

where:

ω_s, ω_f – starting and closing frequency of the analyzed band,

x_i, x_{ref} – characteristic in the current and reference state respectively.

The measure results are presented in Table 3.

Table 3. Modal filtration system measure results

No	Measure Results			comment
	DI[0]	DI[1]	DI[2]	
1	1.46E-02	4.53E-02	2.82E-02	REFER. F=0kN
2	8.07E-01	8.17E-01	4.00E-01	F=5kN
3	8.83E-01	7.59E-01	4.80E-01	F=10kN
4	9.60E-01	9.24E-01	6.98E-01	F=20kN
5	1.03E+00	1.11E+00	7.52E-01	F=25kN
6	1.11E+00	1.30E+00	8.31E-01	F=30kN
7	1.44E+00	1.31E+00	1.34E+00	F=35kN
8	8.54E-01	8.71E-01	7.10E-01	F=15kN
9	2.07E-01	4.39E-01	3.50E-01	F=0kN
10	1.35E+00	1.16E+00	1.13E+00	F=35kN

For every measure there are three damage index values calculated for different modal filter. Measurement no. 1 was performed in object reference state. We can notice relatively small values, which may lead to conclusion that there is little or no change in truss internal structure since the reference measure was done.

Next step was to increase value of force applied to the object and measure damage index values for each step. As we can see in Table 3, larger force values means higher damage index values. This fact fully agree with theory, as internal structure stress have an impact on modal response.

The load was increased up to the value of 35 kN, when the object started to deflate.

The object deflation was confirmed by vision system measurements used in parallel during tests. If we look again at characteristics shown in Figure 10 we can see a bend in both load curves around the point where load with value of 30kN was applied. This suggests internal truss structure change.

After that a value of force was step-by-step decreased up to the point where no force was applied to the object. Looking at Table 3 we can easily notice the difference in damage index values between measurements 1 and 9.

If there were no internal change in the structure of truss, measured damage index values would be similar. However, these values are over 10 times greater, which means that internal structure of truss had changed. This conclusion had been confirmed by measures, as the object remained deformed after load removal (Figure 12).



Fig. 13. Deformed truss in the point of jack mounting

CONCLUSIONS

Deflection and displacement measurements are valuable indicators of the state of analyzed structures. Displacement of points can point to elongation or shortening of the structural members due to temperature change, breaking loads or a damage. Multimodal sensor integration (strain gauges and LVDT) in the SHM system allowed to reveal an unexpected deflection increase and to detect a damage within the girder. Main advantages of the vision techniques application are high measurement density, the possibility of carrying out global examination of the object's state, flexibility, universality and low cost. The measurements are carried out contactless and without introducing undesirable changes in its dynamical properties like additional masses or stiffness.

Second of tested systems is based on modal filtration of system characteristics. This obviously involves need of installing sensors on tested object. However there is no need to apply a large number of sensors even on large objects. The system in general detects damage with good sensitivity (as confirmed by used in parallel vision system), however the sensors should not be replaced during system operation, as this could affect measurement results.

The performed research has confirmed the applicability of vision-based technique and modal filtration based method to evaluate the engineering structures' state and to detect the presence of a damage.

ACKNOWLEDGEMENT

Research funding from the Polish research project MONIT (No. POIG.01.01.02-00-013/08-00) is acknowledged by the authors

Authors would like to express their special thanks to Professor Stanislaw Radkowski, dr Jędrzej Mączak and A. Gałęzia for the possibility to make measurement on the stand in Warsaw University of Technology.

REFERENCES

- [1] T. Uhl, P. Kohut, K. Holak, *Prototype of the vision system for deflection measurements*. Diagnostyka (4), 3–11, 2011
- [2] T. Uhl, P. Kohut, K. Holak, K. Krupiński, *Vision based condition assessment of structures*, Journal of Physics, Conference Series, vol. 305 (2011) pp. 1–10
- [3] P. Kohut, P. Kurowski, *The integration of vision based measurement system and modal analysis for detection and localization of damage Engineering achievements across the global village*, The International Journal of INGENIUM, pp. 391–398, 2005
- [4] P. Kohut, P. Kurowski, *The integration of vision system and modal analysis for SHM applications Proceedings*, Of the IMAC-XXIV a conference and exposition on structural dynamics, pp. 1–8, St.Louis, USA, 2005
- [5] S. Jang, S. Sim, B. Spencer, *Structural damage detection using static strain data* Proceedings of the World Forum on Smart, Materials and Smart Structures Technology, China, 2007
- [6] H. J. Guo, Z. Li, *Structural damage detection based on strain energy and evidence theory*. Journal of Applied Mechanics and Materials 48–49, 1122–11256, 2011
- [7] X. Chen, H. Zhu, C. Chen, *Structural damage identification using test static databased on grey system theory*, Journal of Zhejiang University Science 6(5), 790–796, 2005
- [8] Dilena M., Morassi A., *Identification of crack location in vibrating beams from changes in node positions*, Journal of Sound and Vibration, Vol. 255, Nr 5, 2002, s. 915-930
- [9] H. J. Guo, Z. Li, *Structural damage detection based on strain energy and evidence theory*. Journal of Applied Mechanics and Materials 48–49, 1122–11256, 2011
- [10] X. Chen, H. Zhu, C. Chen, *Structural damage identification using test static databased on grey system theory*, Journal of Zhejiang University Science 6(5), 790–796, 2005
- [11] H. Li, H. Yong, J. O, Y. Bao, *Fractal dimension-based damage detection method for beams with a uniform cross-section*. Computer-Aided Civil and Infrastructure Engineering 26(3), 190–206, 2011
- [12] Hensman J., Surace C., Gherlone M., *Detecting mode-shape discontinuities without differentiation - examining a Gaussian process approach*, Journal of Physics: Conference Series 305, 2011, s. 1-10
- [13] S. Patsias, W. J. Staszewski, *Damage detection using optical measurements and wavelets*. Structural Health Monitoring 1(1), 5–22, 2002
- [14] A. Gałęzia, S. Gontarz, M. Jasiński, J. Mączak, S. Radkowski, J. Seńko, *Distributed system for monitoring the large scale infrastructure structures based on changes analysis of its static and dynamic properties*. Key Engineering Materials. Vol. 518, 2012, pp 106-118, 2012
- [15] J. Bajkowski, M. Jasiński, J. Mączak, S. Radkowski, R. Zalewski, *The active magnetorheological support as an element of damping of vibrations transferred from the ground to large-scale structure supports*. Key Engineering Materials, Vol. 518, pp 350-357, 2012
- [16] Hartley R., Zisserman A., *Multiple View Geometry in Computer Vision*, Cambridge University Press, 2004
- [17] Z. Zhang. *A flexible new technique for camera calibration*. IEEE Trans. Pattern Anal. Mach. Intell., 22 (11) (2000) 1330-1334
- [18] Holak K., Kohut P., Martowicz A., Uhl T., *An uncertainty analysis for developed measurement vision system aided by numerical simulations*, Mechanics and Control, vol. 30, Nr 2, 2011, s. 65-72
- [19] Holak K., Uhl T., Kohut P., Krupiński K., *Vision based condition assessment of structures*, 9th International Conference on Damage Assessment of Structures (DAMAS 2011), Journal of Physics: Conference Series 305, IOP Publishing, 2011
- [20] Holak K., Kohut P., Uhl T., Krupiński K., Owerko T., Kuraś P., *Structure's Condition Monitoring Based on Optical Measurements*, Key Engineering Materials, Vol. 518, s. 338-349.
- [21] Deraemaeker A., Preumont A., *Vibration based damage detection using large array sensors and spatial filters*, Mechanical Systems and Signal Processing, Vol. 20, Is. 7, 1615-1630, (2006)
- [22] Mendrok K., Uhl T.: *Modal filtration for damage detection and localization*, Proceedings of 4th EWoSHM, Krakow, (2008)
- [23] Mendrok K.: *Simulation verification of damage detection algorithm*, Diagnostyka, Vol. 3, 17–23, (2010)
- [24] Mendrok K., Uhl T., *Overview of modal model based damage detection methods*, Proceedings of 2004 ISMA, Leuven, Belgium, (2004)
- [25] Zhang Q., Allemang, R.J., Brown, D.L., *Modal Filter: Concept and Applications*, Proceedings of International Modal Analysis Conference, pp. 487-496, (1990)
- [26] Meirovitch L., Baruh H., *Control of self-adjoint distributed parameter system*, Journal of Guidance Control and Dynamics, 8 (6), 60-66, (1982)
- [27] Mendrok K., Maj W.: “Laboratory tests of the SHM system based on modal filtration”, Diagnostyka, Vol. 1, 13–20, (2011)
- [28] Mendrok K., Uhl T.: *The application of modal filters for damage detection*, Smart Structures and Systems, Vol. 6, No. 2 115-133, (2010)



Ph.D. **Piotr KOHUT**, is an adjunct professor at the Department of Robotics and Mechatronics of AGH University of Science and Technology in Cracow. His scientific interests focus on mechatronics, vision systems, methods of image processing and analysis as well as 3D measurement techniques.



DSc. Eng. Krzysztof MENDROK

is a senior researcher in the Department of Robotics and Mechatronics of the AGH University of Science and Technology. He is interested in development and application of various SHM algorithms. He mainly deals with low frequency vibration based methods for damage detection and inverse dynamic problem for operational load identification.



M.Sc. Eng. Krzysztof HOLAK

is Ph.D. student at the Department of Robotics and Mechatronics of AGH University of Science and Technology in Cracow. His works are connected with image processing, analysis and vision measurement systems.



MSc, Eng. Wojciech MAJ

is PhD student in the Department of Robotics and Mechatronics of the AGH University of Science and Technology. The main areas of his interest are digital signal processing and parallel computing architectures.

MAINTENANCE ON DEMAND FOR VEHICLE SUSPENSION SYSTEM

Przemysław MAGDA, Tadeusz UHL

Katedra Robotyki i Mechatroniki, Akademia Górniczo-Hutnicza im. Stanisława Staszica w Krakowie
tel: +48 12-617-31 16, fax: +48 12 634 35 05, pmagda@agh.edu.pl

Summary

This paper presents a method for evaluation health condition of car suspension. Research covered verification between 3D model from Virtual.Lab and mathematical models created in the Matlab/Simulink environment. All the analysis is performed for the full car model.

Created models are used for verification of suspension test in cars: EUSAMA and Minimum Phase Shift (MPS). Subsequently they are simulated in order to present behavior of degrading suspension with gamma distribution.

Research was performed under Maintenance on Demand project with cooperation with LMS International, DHL, Volvo.

Keywords: Structural Health Monitoring, vehicle suspension, mathematical car model.

MONITOROWANIE STANU ZAWIESZENIA W POJAZDACH

Streszczenie

W artykule przedstawiono wyniki prac nad wyznaczaniem stanu amortyzatorów w zawieszeniu samochodów osobowych. Badania obejmowały weryfikację modeli 3D w programie Virtual.Lab z modelami matematycznymi wykonanymi w środowisku Matlab/Simulink. W pracy przedstawione będą wyniki analiz uproszczonego modelu samochodu.

Opracowane modele posłużyły w dalszej części do testowania metod używanych do sprawdzania stanu zawieszenie w pojazdach: EUSAMA i Minimum Phase Shift (MPS). Następnie prezentacji ich zachowania dla degradowanych amortyzatorów przy użyciu dystrybucji gamma.

Prace realizowane były w ramach projektu Maintenance on Demand przez m. in. LMS International, DHL, Volvo.

Słowa kluczowe: Monitorowanie stanu konstrukcji, zawieszenie pojazdu, matematyczny model pojazdu.

1. INTRODUCTION

Machine condition monitoring and fault diagnostic is a technical activity in which selected physical parameters are observed in order to determine machinery integrity. Once it is diagnosed, this information can be used for maintenance activities. The ultimate goal in case of maintenance is optimum use of resources [1].

Machine failure can be determined when machine exceeds operational limit which is designed for safe operation. As machine gradually reaches the end of its designed lifetime, the frequency of failures increases. It is connected with degradation of the parts, metal fatigue, wear mechanisms between moving parts, corrosion. Such failures are called "wearout".

Maintenance strategies can be divided into types:
- run-to-failure – also called breakdown maintenance or corrective maintenance is a strategy in form of repair work or replacement if and only if machinery, object has failed. This type of maintenance can be used if the equipment is redundant, spare parts are cheap or the repair/replacement is quick [1],

- scheduled maintenance – also called planned maintenance is any scheduled service to ensure that machinery is working within operational limits [2],
- condition-based maintenance – is a strategy requiring assessing the actual condition of the machinery thus machinery could be corrected at the right time [2].

2. FULL CAR MODEL

2.1 Mathematical model

Mathematical model was created in Matlab/Simulink software. As illustrated in fig. 1 model has 7 degree-of-freedom: main body (chassis – can rotate along the pitch and roll poles, and translate along z axis) is connected to four unsprung masses (wheel hubs) located at each corner, subsequently front-left (fl), front-right (fr), rear-left (rl), rear-right (rr). Hubs translate vertically with respect to the sprung (main body). Suspensions situated between sprung and unsprung masses are modeled as linear viscous dampers and spring with constants coefficients. In case of tire, simple linear

spring with constant coefficient is used [3]. For simplicity, small pitch and roll angles are assumed, which results in linearization of $\sin(\varphi)$ to φ .

Equations describing 7-DOF vehicle with passive suspension:

- Sprung mass (chassis) motion:

$$M_{ch}\ddot{Z}_{ch} = F_{sfl} + F_{dfl} + F_{sfr} + F_{dfr} + F_{srl} + F_{drl} + F_{srr} + F_{drr} \quad (1)$$

M_{ch} is a chassis mass, \ddot{Z}_{ch} vertical acceleration along z axis. Each corner is represented by pair of forces, one is a spring force while second comes from damper. For example F_{sfl} is a spring force and F_{dfl} is a damper force, both located at the front left corner of the vehicle.

$$I_{pitch}\ddot{\theta} = (F_{sfl} + F_{dfl} + F_{sfr} + F_{dfr})lL + (F_{srl} + F_{drl} + F_{srr} + F_{drr})lR \quad (2)$$

I_{pitch} is a moment of inertia about the pitch center (y axis), $\ddot{\theta}$ corresponds to pitch acceleration, lF and lR are distances between center of gravity and front axle, rear axle.

$$I_{roll}\ddot{\varphi} = (F_{sfl} + F_{dfl} + F_{srl} + F_{drl})\frac{wC}{2} - (F_{sfr} + F_{dfr} + F_{srr} + F_{drr})\frac{wC}{2} \quad (3)$$

I_{roll} is a moment of inertia about the roll center (x axis), $\ddot{\varphi}$ corresponds to roll acceleration and wC is a model width (it is assumed that center of gravity is located on the roll center).

- Unsprung mass (wheel) motion:

$$M_{WhFL}\ddot{Z}_{FL} = F_{tireFL} - F_{sfl} - F_{dfl} \quad (4)$$

$$M_{WhFR}\ddot{Z}_{FR} = F_{tireFR} - F_{sfr} - F_{dfr} \quad (5)$$

$$M_{WhRL}\ddot{Z}_{RL} = F_{tireRL} - F_{srl} - F_{drl} \quad (6)$$

$$M_{WhRR}\ddot{Z}_{RR} = F_{tireRR} - F_{srr} - F_{drr} \quad (7)$$

M is a mass of a wheel hub in particular corner of chassis, Z corresponds to vertical acceleration and F_{tire} is a tire force.

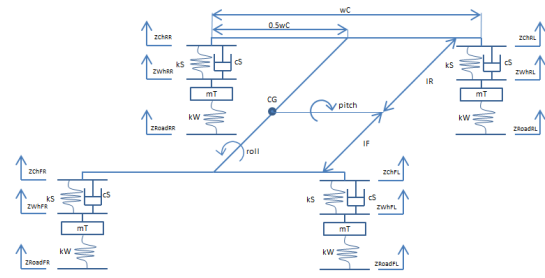


Fig. 1. Full car – mathematical model

2.2 Virtual.Lab model

CAD model was created in the LMS Virtual.Lab software. Idea behind that was to check and validate results from that model with the one designed using mathematical equations in Matlab environment. Obtaining the same results, could significantly reduce time needed to create and computer simulation (as it is faster to create a model in CAD environment instead of developing equations).

In order to obtain reliable outputs from the simulations, simplified full car model in Virtual.Lab was created as close as possible to its mathematical version. Main body (chassis) was constrained with use of bracket joint (special type of joint which gives user opportunity to constrain body between 6 to 0 DOF), so it could translate along z axis and rotate along x and y axis, while wheel hubs were constrained with translational joint (allows translation only along one axis).

As it was in case of Matlab, CAD models had the same type of suspension (with linear viscous damper with linear spring) and tire (linear spring, no damping), they were created by TSDA force (Translational – Spring – Damper - Actuator) [4].

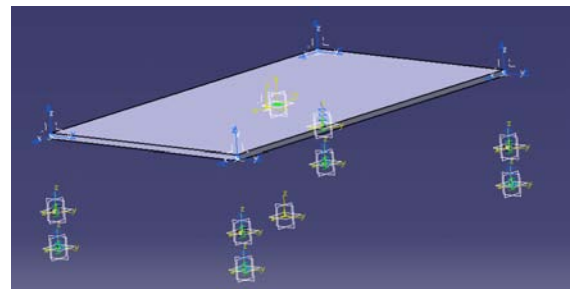


Fig. 2. Full car – Virtual.Lab model

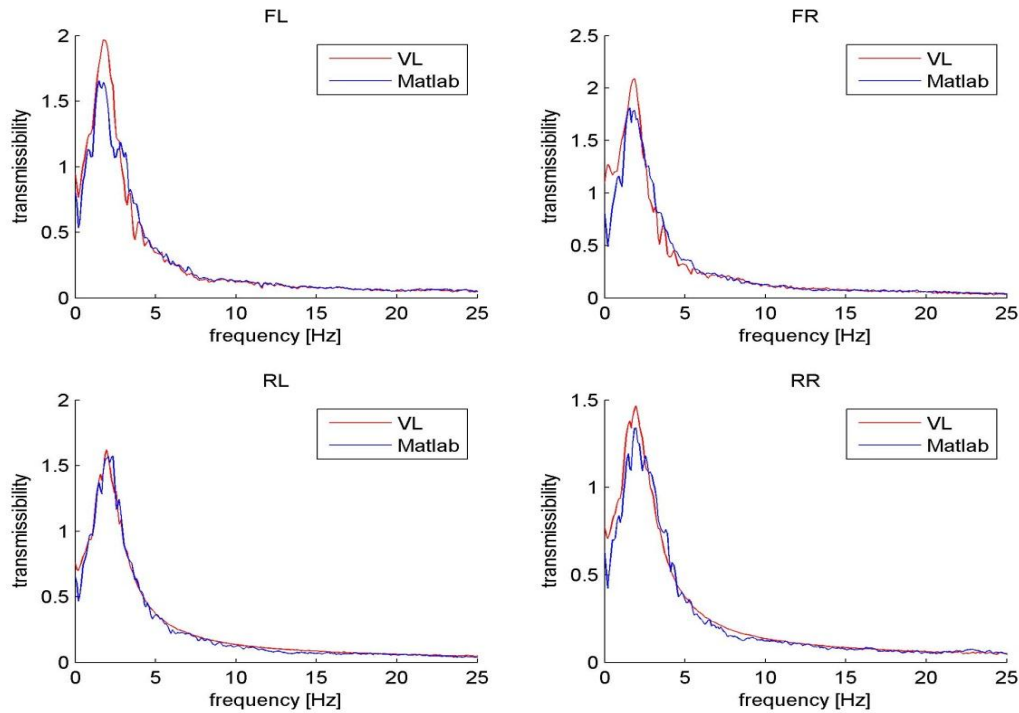


Fig. 3. Full car simulation comparison

2.3. Results validation between mathematical and Virtual.Lab model

Both models (from VirtualLab and Matlab) were simulated with the same real road data, which was measured by LMS International equipment installed on the car - Mercedes C350.

Full car model parameters used in simulation are provided in Table 1. CAD model shows some differences compared to the mathematical one (fig. 3). Apart from the difference in magnitude, Matlab and VL results are slightly shifted along the frequency axis. Such a phenomena can be explained by the errors in roll and pitch rotation. Unfortunately it was impossible to eliminate yaw.

Table 1. Car parameters for Matlab and VL

mT = 70; % hub mass
mC = 1640; % car mass
kW = 240000; % tire stiffness
kS = 64000; % spring stiffness
cS = 700; % damping
wC = 1.6; % car width
IR = 1.4904; % distance from rear to CG
IF = 1.2696; % distance from front to CG
Ir = 540; % roll inertia
Ip = 2800; % pitch inertia

3. SHOCK ABSORBER TEST

3.1 EUSAMA test

EUSAMA (European Shock Absorber Manufacturers Association) evaluated test for determination suspensions' condition [5] Adhesion (EUSAMA value) is a minimal percentage of instantaneous remnant vertical tire contact force between the tire and the road surface.

$$EUSAMA = \frac{F_{min}}{F_{static}} * 100\% \quad (8)$$

During measurement each axle is tested separately on shaker/test bed. First equipment weights static load of each wheel, then plate of a shaker vibrates with chirp sinus starting from 0Hz to 25Hz and 6mm stroke. Minimum EUSAMA value (adhesion) occurs at the resonant frequency of the unsprung mass (between 10– 20Hz, depending on parameters of a suspension).

Table 2. EUSAMA value interpretation [5]

EUSAMA value	Interpretation
61% - 100%	Excellent dynamic wheel contact
41% - 60%	Good dynamic wheel contact
21% - 40%	Poor dynamic wheel contact
0% - 20%	Damper is classified as broken

Damper is classified as broken when the EUSAMA value is lower than 21% (Table 2) or difference between left and right wheel for axle is bigger than 50% [5].

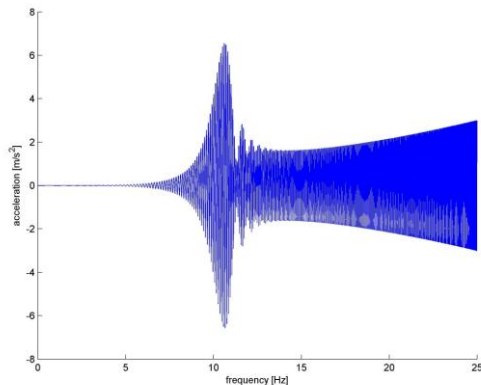


Fig. 4 Wheel hub response

3.2. Minimum phase shift test

Minimum phase shift test is introduced by GOCA (Belgian vehicle inspection) [6], because EUSAMA was not reliable for super light vehicles, vehicles with run flat tire, and it could have happened that heavy vehicles despite a bad working shock absorber pass the EUSAMA test [6].

Phase shift is an angular difference between the sinusoidal position of the suspension tester platform and the sinusoidal vertical tire contact force between the tire and suspension tester platform. This test uses the same measurement equipment and input chirp signal (sinus signal with amplitude 3mm and frequency varying from 0 to 25Hz) as it is in case of EUSAMA test [6].

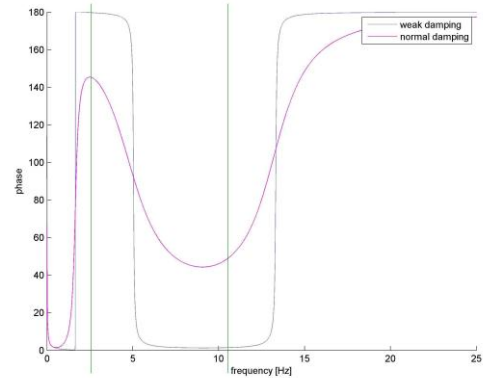


Fig. 5 Minimum phase shift – ideal

Resonant frequency of the sprung mass is located between 1 and 3 Hertz. If no damping occurs, the phase angles are equal to:

$$\varphi_{23} = \varphi_2 - \varphi_3 = 180^0 \quad (9)$$

$$\varphi_{13} = \varphi_1 - \varphi_3 = 0^0 \quad (10)$$

$$\varphi_{12} = \varphi_1 - \varphi_2 = -180^0 \quad (11)$$

where:

- φ_1 – phase angle of sprung mass
- φ_2 - phase angle of unsprung mass
- φ_3 - phase angle of suspension tester platform/road
- φ_{12} - phase shift between φ_1 and φ_2 (transmissibility phase)
- φ_{13} - phase shift between φ_1 and φ_3
- φ_{23} - phase shift between φ_2 and φ_3

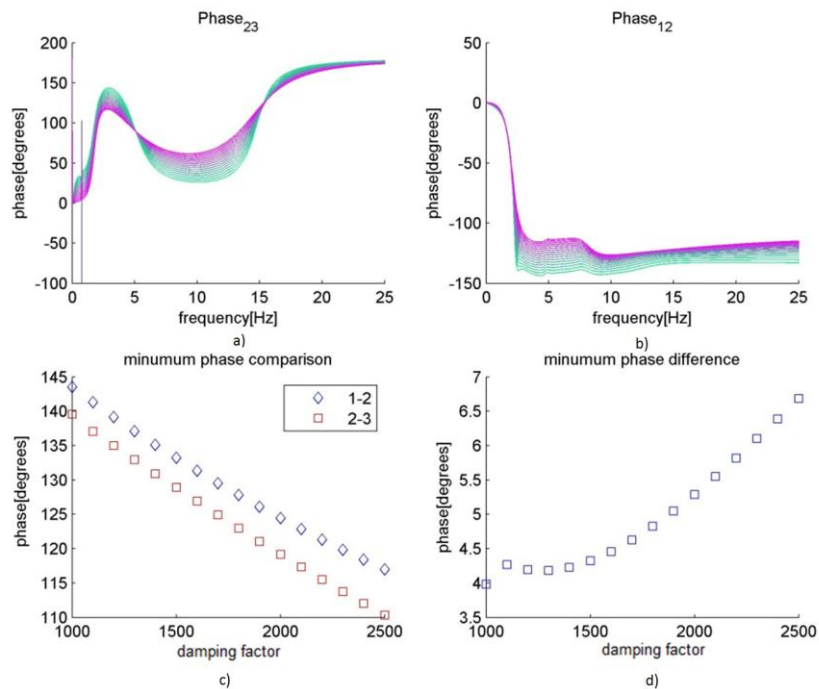


Fig. 6 Phase difference – full car model (front left wheel) – a) phase shift between φ_2 and φ_3 , b) phase shift between φ_1 and φ_2 , c) comparison between minimum phase shift values for $-\varphi_{12}$ and φ_{23} with respect to damping factor, d) difference between minimum phase shifts $-\varphi_{12}$ and φ_{23} with respect to damping factor

At that frequency, relative displacement between sprung and unsprung mass is maximum. Increasing damping factor results in decreasing mentioned distance and increasing φ_{23} [7]

Resonant frequency of sprung mass depending on the parameters varies between 10 and 20 Hertz.

The phase angle between indicates the strength of the shock absorber in the vehicle. Term “minimum phase shift” corresponds to the lowest value of the phase angle between sprung and unsprung mass. Corresponding to the criteria introduced by GOCA, shock absorber is classified as broken if that value is lower than 40° [6].

3.3. Relations between transmissibility and minimum phase shift test

Fig. 6a and 6b presents phase shifts evaluated for φ_{23} and φ_{12} .

The transmissibility calculated between wheel hub and chassis cannot be directly connected to the minimum phase shift criterion. However according to the equations (eq. 9, eq. 10, eq. 11), some similarities can be found. Minimum value of transmissibility between 1Hz and 3Hz should be exactly opposite to the phase shift between wheel hub and tester platform within the same frequency range (fig 6c).

As it is illustrated in fig. 6d the difference between phase shift and transmissibility from 1Hz to 3Hz is equal up to 10 degrees. In most cases it can be expressed in form of quadratic or cubic function. The error between those two quantities could be even assumed to be zero, for simplicity.

Unfortunately there is no easy and clear way how to move from transmissibility value of phase shift from 1Hz to 3Hz, to minimum phase shift value.

4 ROAD PROFILE

Road surface is considered as random surface. As with any random signal such profile can be represented with use of Fourier transform into sum of sine waves with varying amplitudes and phase shifts. A plot of amplitude with respect to the frequency can be represented in form of power spectral density.

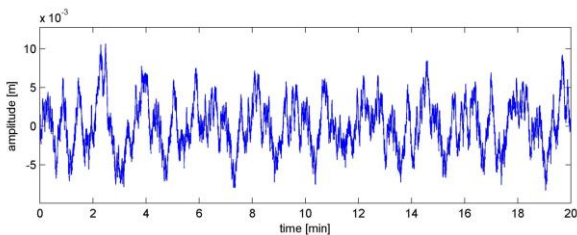


Fig. 7 Road signal (road class A – highway), dt = 200ms

It is known that PSD of the roughness of a road profile has the decreasing tendency with increasing

wavelength. In the table below one can see the approximations of PSD, obtained by fitting the experimental data [8].

Table 3. PSD approximation – analytical [8]

Name	PSD approximation	Wavenumber
ISO (1995-09-01)	$G_d(n) = Cn^{-w}$	$0 \leq n \leq \infty$
BSI (1972)	$G_d(n) = \begin{cases} Cn^{-w_1} \\ Cn^{-w_2} \end{cases}$	$0 \leq n \leq n_0$ $n_0 \leq n \leq \infty$
Two Split	$G_d(n) = \begin{cases} Cn^{-w_1} \\ Cn^{-w_2} \\ Cn^{-w_3} \end{cases}$	$0 \leq n \leq n_1$ $n_1 \leq n \leq n_2$ $n_2 \leq n \leq \infty$
Sayers (1986)	$G_d(n) = \frac{C_1}{n^4} + \frac{C_2}{n^2} + C_3$	$0 \leq n \leq \infty$
Gillespie (1985)	$G_d(n) = \frac{C(1 + (\frac{0.066}{n^2}))}{n^2}$	$0 \leq n \leq \infty$
Marcondes et al. (1991)	$G_d(n) = \begin{cases} C_1 \exp(-kn^p) \\ C_2(n - n_0)^q \end{cases}$	$0 \leq n \leq n_0$ $n_0 \leq n \leq \infty$
Sussman (1974)	$G_d(n) = \frac{C}{\alpha^2 + n^2}$	$0 \leq n \leq \infty$
Macvean (1980)	$G_d(n) = \frac{C}{(\alpha^2 + n^2)^2}$	$0 \leq n \leq \infty$
Xu et al. (1992)	$G_d(n) = \frac{A}{2\alpha \exp(\frac{-n^2}{2\alpha^2})}$	$0 \leq n \leq \infty$
Kozin and Bodanoff (1961)	$G_d(n) = \frac{A}{\alpha \exp(\frac{-n^2}{\alpha^2})}$	$0 \leq n \leq \infty$

Note: C, C1, C2, C3 – unevenness index, ω – waviness of the road surface, p, k, q, α and β are real positive constants.

MoDe project is focused on frequency range between 0.2 Hz and 20Hz, which is normally considered in vehicle dynamics for comfort, safety and road holding analyses as ride. Mentioned frequency corresponds to the wavelength from 100m to 1m. However for wavelengths higher than 100m PSD function become flat. It means that road input excitation is not a white noise, but Brownian or red one [8].

International Organisation for Standardization introduced road roughness divided into eight classes

(ISO 1995-09-01, starting with A – highway and ending on H – offroad).

ISO standards suggest $w = 2$ for road undulations, for disturbances with wavelength greater than 6 meters, and $w = 1.37$ for irregularities with a wavelength smaller than 6 meters [8].

Road input with desired ISO class was generated in time domain and low pass filtered for frequencies below 25Hz. Graphs of estimated PSD, PSD of generated signal before and after filtering, and PSD of real measured signal are plotted on fig. 8.

Fig. 8 represents comparison between four PSD.

- ideal PSD – corresponds to the PSD approximation according to ISO standard
- raw PSD – PSD of artificially generated road signal
- filtered PSD – raw PSD + low pass filter (25Hz)
- measured PSD – PSD from measured road signals on Mercedes C350.

Table 4 ISO – PSD approximation coefficients [8]

Road class	C factor
A	1.6e-7
B	6.4e-7
C	2.56e-6
D	1.024e-5
E	4.096e-5
F	1.6384e-4
G	6.5536e-4
H	2.62144e-3

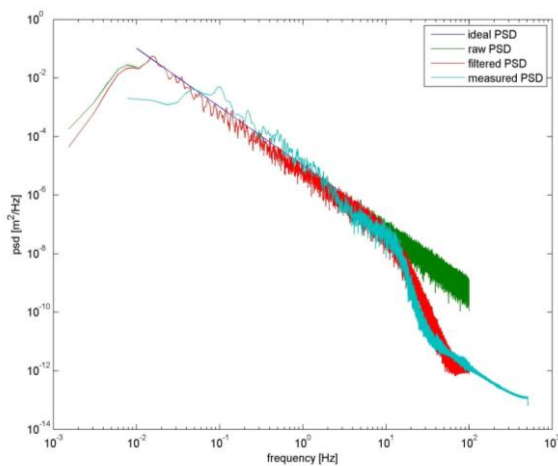


Fig. 8 Comparison between ideal, raw, filtered and measured PSD

5. GAMMA DEGRADATION

The gamma process is ideally suited to model graduate damage that monotonically accumulates over time, such as wear, corrosion, erosion, and creep of materials, which are common causes of failure of engineering components [9]

However two types of gamma degradation models can be distinguished:

- Threshold model supposes that the item or system fails whenever its degradation level reaches a certain critical deterministic or random threshold [9].
- Shock model supposes that the item or system is subjected to external shock which may be survived or lead to failure. The shocks usually occur according to Poisson process whose intensity depends on degradation and environmental factors [9].

It is possible to combine those two models into one (as Lemoine and Wenocur suggested) and obtain degradation – threshold – shock model (DTS model).

6. DEGRADATION DATA – SIMULATION (GUI)

6.1. Road profile

At the beginning of the program user loads a symbolic road profile from the text file (*.txt). File should consist of 3 columns and minimum one row.

Table 5 Symbolic road profile 1

B	50	20
A	120	20
C	50	10
D	30	5
B	30	15
E	35	5

First column is a road class (according to ISO standards – letter from A to H), second one is an average speed of the vehicle (km/h) while last one time (min).

For example (generated road profile is illustrated in fig. 9) It is assumed that road profile is the same for the side wheels. However signal between front and rear is shifted by the time delay derived from average velocity and distance between wheels. Generated profile is assumed to have constant surface condition of dry road without any influence of snow or rain.

6.2. Transmissibility

After road profile is generated, program calculates damping degradation (starting from healthy to worn damper with previously determined damping factors) for each wheel separately. Subsequently full car Matlab model is simulated n times, (where n is a number of measurements) with road signal divided into equal length parts each with damping changing damping factor.

6.3. Minimum transmissibility

As an output from simulation, program calculates the minimum values of each transmissibility phase (between 0Hz and 25Hz). Comparing to the transmissibility amplitude, the minimum phase is monotonically decreasing with dropping damping factor.

Normally the minimum value of phase transmissibility should be located between 1Hz and 3Hz, but it can move on the frequency axis when influenced by other shock absorbers.

Script generates random road signal according, and subsequently calculates phase shifts (fig. 11).

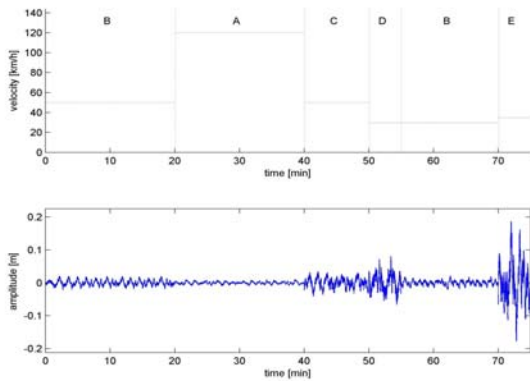


Fig. 9 Generated road profile

Result of minimum phase values after simulation with 400 measurement points are shown in the plot fig 10.

It is easy to notice that main assumption about degradation is satisfied – the smallest value of the phase shift between wheel and chassis is always decreasing.

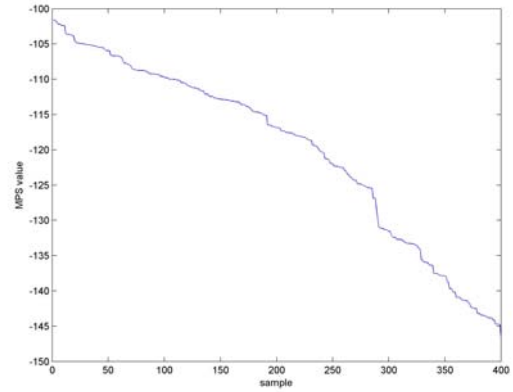


Fig. 10 MPS value during the simulation

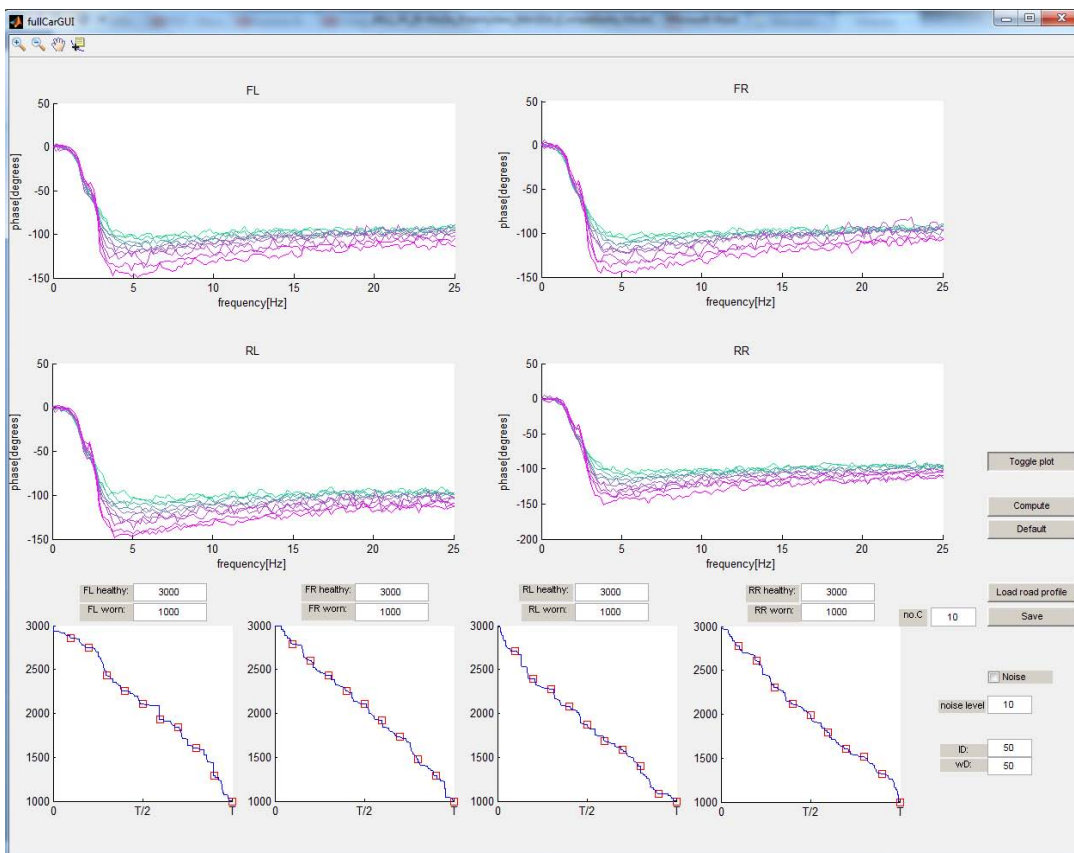


Fig. 11 Degradation data simulation (GUI)

7. CONCLUSIONS

Project originally was created for Volvo trucks, however all the measurement were performed on the Mercedes C350, which means that all the steps made so far, should be repeated with focus on a truck model.

After validation between Matlab and Virtual.Lab environment results were still different.

It is necessary to point out that output data from simulation is the same from those two programs in case no rotation.

Further work should be focused on evaluating gamma degradation based on real data from the manufactures.

Eventually, minimum value of transmissibility ought to be connected to the EUSAMA or minimum phase shift method to determine if damper is healthy or broken.

8 BIBLIOGRAPHY

- [1] Mechefsk C. K., *Machine Conditioning, Monitoring and Fault Diagnostics*, Vibration and Shock Handbook, CRC Press, 2005, pp. 25-1 – 25-9.
- [2] Randall R. B., *Vibration-based Condition Monitoring: Industrial, Aerospace and Automotive Applications*, Wiley, 2011, pp. 1-23.
- [3] Abramov S., Durieux O., Mannan S.: *Semi-Active Suspension System Simulation Using SIMULINK*, Int. J. of Engineering Systems Modelling and Simulation – Vol. 1 No. 2/3, 2009, pp. 101-114.
- [4] LMS Virtual.Lab on-line help, Revision 9-SL3, 2010.
- [5] Tsymborov A.: *An Improved Non-Intrusive Automotive Suspension Testing Apparatus with Means to Determine the Condition of the Dampers*, SAE Technical Paper 960735, 1996
- [6] Buekenhoudt P.: *Minimum phase shift*, CITA International Motor Vehicle Inspection Committee Conference and 15th General Assembly, 2011.
- [7] Goktan A. G., Yetkin A., *Road Load Data Estimation on Multiaxial Test Rigs for Exhaust System Vibrations*, SAE Technical Paper 2002-01-0805, 2002
- [8] Soria L., delli Carri A., Peeters B., Anthonis J., Van der Auweraer H.: *Active Suspension Systems for Passenger Cars: Operational Modal Analysis as a Tool for the Performance Assessment*, Modal Analysis Topics, Volume 3, Springer New York, 2011, pp. 313-323.
- [9] Lehmann A.: *Failure Time Models Based on Degradation Processes*, Advances in Degradation Modeling, Birkhäuser Boston, 2010, pp. 209-231.



non-destructive testing.

Przemyslaw MAGDA received a M.Sc. degree in Mechatronics from the Faculty of Mechanical Engineering and Robotics, AGH University of Science and Technology in 2012. He is a Ph.D. student in the Department of Robotics and Mechatronics. His main research interest is structural health monitoring and



non-destructive testing.

Tadeusz UHL received a M.Sc. degree in 1979 at AGH University of Science and Technology, the Ph.D. in 1983. He is currently employed at AGH University as a professor and Head of Department of Robotics and Mechatronics. His main area of research is construction dynamics, especially modal analysis. His field of scientific interest concerns control systems and mechatronic systems.

non-destructive testing.

Tadeusz UHL received a M.Sc. degree in 1979 at AGH University of Science and Technology, the Ph.D. in 1983. He is currently employed at AGH University as a professor and Head of Department of Robotics and Mechatronics. His main area of research is construction dynamics, especially modal analysis. His field of scientific interest concerns control systems and mechatronic systems.

DYNAMIC STATE ASSESSMENT OF THE WATER TURBINE WITH THE POWER OF 600 kW

Grzegorz ŻYWICA, Paweł BAGIŃSKI, Łukasz BREŃKACZ

Institute of Fluid-Flow Machinery, Polish Academy of Sciences
80-231 Gdansk, Fiszerka 14 str., gzywica@imp.gda.pl

Summary

The article discusses the results of experimental studies to assess the dynamic state of the turbine set with the Kaplan turbine. The dynamic assessment was made on the basis of appropriate standards, based on the measurement results of selected parameters of vibration, which have been measured for several states of the machine load. In addition, we attempted to identify the causes of the increased vibration levels based on the measured vibration spectrum and the temperature distribution on the machine casing. On the basis of analysis results, the tested fluid-flow machine was qualified in the appropriate zone (defining the state of vibration) and identified the source of high levels of vibration.

Keywords: machine's dynamic state, vibrodiagnostics, water turbine, Kaplan turbine.

OCENA STANU DYNAMICZNEGO TURBINY WODNEJ O MOCY 600 kW

Streszczenie

W artykule omówiono wyniki badań eksperymentalnych mających na celu ocenę stanu dynamicznego hydrozespołu z turbiną Kaplana. Oceny stanu dynamicznego dokonano w oparciu o odpowiednie normy, na podstawie wyników pomiarów wybranych wielkości charakterystycznych drgań, które zostały zmierzone dla kilku stanów obciążenia maszyny. Dodatkowo, podjęto próbę wskazania przyczyn podwyższonego poziomu drgań w oparciu o zmierzone widma drgań oraz rozkład temperatury na korpusie maszyny. Na podstawie przeprowadzonych analiz zakwalifikowano badaną maszynę przepływową do odpowiedniej strefy (określającej jej stan drganiowy) oraz wskazano źródło podwyższonego poziomu drgań.

Słowa kluczowe: stan dynamiczny maszyny, wibrodiagnostyka, turbina wodna, turbina Kaplana.

1. INTRODUCTION

During diagnostic tests we can distinguish two main phases (regardless of the type of technical objects); they are the evaluation of the condition and the damage identification. The evaluation of the condition focuses on testing whether the examined object is suitable for use as a whole one, whereas during the damage identification only individual elements of the technical object are checked [1]. Since defects in the different parts of the machine may occur in a similar manner, the task of locating the damage is much more difficult.

The reason for the development of the article was to show the practical possibility of the use of modern diagnostic methods during the tests carried out on the working fluid-flow machine. The usefulness of diagnostic methods developed and used by researchers can be evaluated in the best way by solving unconventional problems in real machines.

1.1. Purpose and scope of research

These studies have been made on demand of a private company – the owner of the hydroelectric

power plant. The company has asked the Institute of Fluid-Flow Machinery PAS in Gdansk, expressing doubts about the quality of the machinery's elements and the proper operation of the turbine set in modernized hydroelectric power plant. After upgrading the power plant the exploited Francis turbine was replaced by a modern Kaplan turbine. It turned out that the work of the new turbine set is accompanied by higher noise and vibration levels than before the replacement.

The aim of this study was to assess the dynamic state of the turbine set (containing Kaplan turbine) in modernized hydroelectric power plant. In the study, the values taken into account were: characteristic parameters of vibration for several states of the machine, vibration spectra and the temperature distribution on the casing. In addition to assessing the condition of the machine, there was also an attempt to identify the causes of high levels of vibration and noise.

1.2. Object of investigation

The tested turbine set with Kaplan turbine has nominal power of 600 kW. The machine works in

the water power plant, which is located next to the cardboard factory, and electricity generated is fed into the national power grid, significantly improving the energy balance of a nearby factory. The dam on the river is shown in Figure 1.



Fig. 1. The dam located next to the hydroelectric power plant



Fig. 2. Tested turbine set in a technical room located in the hydroelectric power plant

Before the experimental study began, operation and maintenance documentation of the turbine set was studied (along with the assembly drawing and technical design of toothed gear). Most important technical data of the machine are included in Tab. 1.

Because of the design solutions, the water turbine's shaft was located under the floor of the technical room (used for the operation of the device). Therefore, there was no direct access to the shaft and its bearings. The upper end of the shaft was supported on the axial spherical roller bearing at the bottom of the wheelcase (that bearing also allowed the transfer of small lateral loads). The toothed gear and the generator were above the floor, as shown in Figure 2. The gear was equipped with a forced oil circulating system. The generator rested on the gear and was fixed by a flange connection.

The power generator's shaft had its own system of bearings and was cooled by a forced air.

Tab. 1. Basic specifications of turbine set.

Water turbine	
Country of origin	Poland
Type of turbine	Kaplan
Year of manufacture	2012
Number of blades	4
Rated speed	147 rpm
Generator	
Country of origin	Poland
Type of generator	Asynchronous, 3-phase
Year of manufacture	2012
Nominal power	600 kW
Rated speed	756 rpm
Mass	4620 kg
Toothed gear	
Country of origin	Poland
Type of gear	Planetary (multiplying)
Year of manufacture	2012
Nominal power	600 kW
Gear ratio	5,11

2. DYNAMIC STATE ASSESSMENT

2.1. Testing method

The study of dynamic state of the machine was carried out according to the standards of ISO10816-1: 1995 [2] and ISO10816-5 [3]. The first of these standards provides general guidance for the measurement and evaluation of mechanical vibration and the other standard sets out detailed recommendations for hydraulic machinery, including water turbines. On the basis of these standards the measurement parameters and measurement nodes were defined. Due to the design solution the turbine set was classified according to [3] to a group number 4, that is, vertical machines sets with lower bearing housings braced against the foundation and upper bearing housings braced against the generator stator only, usually with operational speed of between 60 rpm and 1000 rpm. The scheme of the test machine along with the designation of the measurement nodes, and coordinate system is shown in Figure 3.

The measurements were carried out in three measurement nodes, and each of them was measured in three directions consistent with adopted axes (Fig. 3). This represented a total of nine measurement locations (points). Measurement nodes were located within the upper bearing of the turbine shaft (I) and the lower (II) and the upper (III) bearing of the generator's shaft. Closed machine housings prevented a direct measurement of vibrations on the bearings, and therefore according to the standards, the measurement points were located on steel flanges connected to the bearing support housings. Due to the construction of turbine set, it was

impossible to perform measurements within the lower bearing of the turbine shaft.

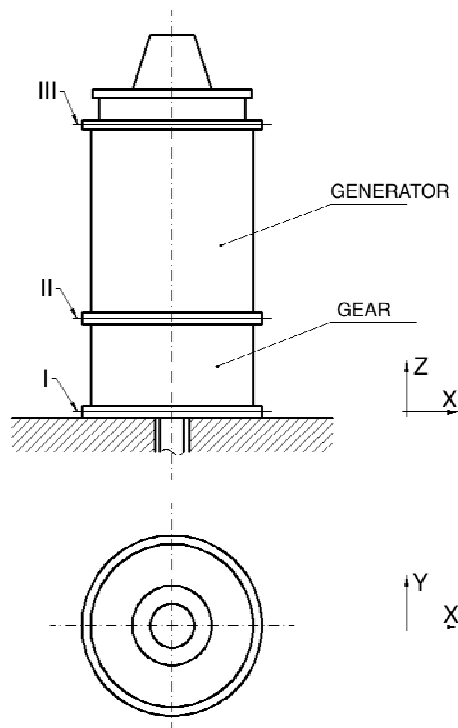


Fig. 3. Scheme of the turbine set with the coordinate system

Based on the standards used [2, 3], the following measuring characteristic values of vibrations were adopted: root mean square of vibration velocity V_{RMS} and peak to peak of vibration displacement A_{P-P} . This was due to the expected wide range of frequencies, in which the harmonic components could occur. For the measurement a mobile device - DIAMOND 401AXT vibration analyzer was used with a connected uniaxial accelerometer. Measurements were carried out in the frequency range 2-1000 Hz with the averaging time equal to 2 seconds. The measurement at each point was performed three times at intervals for approximately 20 seconds, and the final results were determined as the arithmetic mean of three measurements.

Research of the characteristic values of vibrations was carried out for five load states of turbine set. Variable load condition was achieved by adjusting the stator blades of the water turbine and rotor blades in such a way that the level of electric power was 105, 200, 307, 403 and 480 kW. Research for several power levels were designed to evaluate the dynamic state of the machine at different load conditions.

2.2. The results

In the case where both the amplitude and the vibration velocity are recorded, an evaluation of the dynamic state of the machine should be carried out based on the more restrictive requirements [3]. The thresholds values provided for new machines of

group 4 are $A_{P-P} = 30 \mu\text{m}$ and $V_{RMS} = 1,6 \text{ mm/s}$ for the bearings supported within the foundation and the $A_{P-P} = 65 \mu\text{m}$ and $V_{RMS} = 2,5 \text{ mm/s}$ for the bearings above the foundation. In the testing machine, measuring node I was within the foundation, while the nodes II and III were above the foundation.

The measurement results of the root mean square value and the vibration amplitude for the three selected levels of load are presented in Tab. 2-4. The values, which according to the standard ISO10816-5 were above the level of vibration for new objects are highlighted in gray.

Tab. 2. The results of measurements at 105 kW

Node number	Direction X		Direction Y		Direction Z	
	V_{RMS} (mm/s)	A_{P-P} (μm)	V_{RMS} (mm/s)	A_{P-P} (μm)	V_{RMS} (mm/s)	A_{P-P} (μm)
I	0,56	7,66	0,61	7,75	2,76	16,50
II	3,61	24,30	3,47	22,23	1,14	12,60
III	3,25	33,77	3,18	38,73	2,18	15,77

Tab. 3. The results of measurements at 307 kW

Node number	Direction X		Direction Y		Direction Z	
	V_{RMS} (mm/s)	A_{P-P} (μm)	V_{RMS} (mm/s)	A_{P-P} (μm)	V_{RMS} (mm/s)	A_{P-P} (μm)
I	0,38	5,45	0,42	7,04	1,40	13,17
II	2,45	20,53	2,59	20,10	0,88	11,63
III	2,55	34,03	2,83	38,20	2,05	16,30

Tab. 4. The results of measurements at 480 kW

Node number	Direction X		Direction Y		Direction Z	
	V_{RMS} (mm/s)	A_{P-P} (μm)	V_{RMS} (mm/s)	A_{P-P} (μm)	V_{RMS} (mm/s)	A_{P-P} (μm)
I	0,36	5,29	0,41	7,01	1,21	18,47
II	2,26	22,43	2,34	23,63	0,84	13,47
III	2,24	34,43	3,02	39,17	1,92	18,93

According to the criteria of evaluation, in the turbine set there was an excess of threshold level of vibration velocity (provided for the machines which are ready for use) at each load level. Summing up the results of the measurements as a whole, we can say that the worst results were obtained for the measurement node no III in the direction of Y. Rms values of vibration velocity, however, did not exceed the second level of vibrations provided in the standard [3], suitable for machines that can be normally accepted for unrestricted long-term operation. At the same time any of the tested operating conditions have not exceeded the value of the amplitude of vibration provided for the new machines. It can therefore be concluded that the source of elevated levels of vibration were high

frequency vibrations. Therefore, there was also an attempt to identify the direct cause of this situation, as discussed in the next part of the article.

It is also worth noting that the standard used [3] gives the universal values developed on the basis of surveys of many machines. This standard also allows to specify by the manufacturer other, acceptable vibration levels, but it must be due to reasonable cause.

3. THE ASSESSMENT OF THE POSSIBILITY OF DEFECT OCCURRENCE

In order to identify the main sources of vibration in the turbine set, spectral frequency analysis was carried out, in which measurement data were collected at various locations on the machine casing. For the testing machine, over a dozen characteristic frequencies associated with the work of the rotors and toothed gear were appointed (summarized in Tab. 5). In determining these frequencies widely known equations, reported in the literature (in the field of diagnostics of rotating machines) were used (e.g. [4-11]). High levels of vibration at these frequencies could indicate the existence of specific defects or malfunction of some components.

Tab. 5. Characteristic frequencies of tested turbine set

Defect	Frequency (Hz)
Water turbine shaft	
Unbalance	2,45
Misalignment or bend	2,45; 4,9; 7,35
Turbine blade vibrations	9,8
Generator shaft	
Unbalance	12,52
Misalignment or bend	12,52; 25,04; 37,56
Electrical excitation	~50, ~100
Toothed gear	
Frequency of meshing the toothed ring with the planetary cage	271,95; 815,85
Frequency of meshing the toothed ring with the satellite wheels	102,9; 308,7
Frequency of meshing the satellite wheel with the central gear	174,83; 524,48

It should be noted that the vibration components measured on the real object almost never coincide exactly with the theoretically determined frequencies, due to the limited FFT resolution. In addition, in the case of vibrations originating from the toothed gear it comes to frequency modulation of signal, which creates so-called sidebands. On one hand it reduces the transparency of the recorded results, but on the other it helps to identify the frequency of meshing gears.

The two most noted frequency characteristics are shown in Figures 4 and 5. The vibration spectra presented in the following figures were recorded at the highest load of the machine, at which the generator obtained power of 480 kW. In order to facilitate the interpretation of the results in the low frequency range (up to 100 Hz) measured quantity was a vibration amplitude (Fig. 4). At higher frequencies (up to 1600 Hz) measured quantity was a vibration velocity (Fig. 5).

Analyzing the vibration spectrum shown in Figure 4 we can see the dominance of the following components of vibration. At very low frequencies (up to 2 Hz), components were associated with the resonance frequency of the system, which results in the vibration of the whole machine and the foundation. At a frequency of 2.5 Hz the rotational speed component was observed (for the water turbine shaft). At 7.5 Hz we can distinguish the component associated with the shaft misalignment or bend, but its amplitude was lower than the synchronous component. At a frequency of 12.5 Hz synchronous component of generator shaft appeared, and at 25 Hz the increased amplitude of vibration testified about a misalignment or deflection of the shaft. Other components of vibrations in Figure 4 was characterized by a much smaller amplitude. Since in the case of measuring the amplitude A_{P-P} vibration limits for new machines are not exceeded even once, it can be concluded that the observed symptoms of various defects were at an acceptable level. Synchronous vibrations of both shafts were relatively low, and the successive harmonics were reduced almost twice, which meant a slight bend or misalignment.

At higher frequencies, for all the measuring nodes similar vibration spectra were recorded. Characteristics shown in Figure 5 was determined for the measured signal at node II in the direction of the Y axis (on the flange connecting the generator with the transmission gear). The recorded vibration signal allowed to draw the following conclusions. The dominant component (272 Hz frequency) of the resulting characteristics relates to the toothed ring's meshing frequency (it was marked by a blue point and its harmonics by yellow and red points). The origin of the vibrations of toothed gear also testified clear sidebands. Elevated levels of vibration can also be observed in successive harmonic frequencies of toothed ring's meshing: 544, 816, 1088, 1360 Hz. At the frequency of 103 Hz a component occurred resulting from the frequency of meshing the satellite wheels with the toothed ring. Under the frequencies within the range of 170 Hz appeared increased vibration levels that could be associated with the co-operation of the satellite wheels with the central wheel of the planetary gear. Other areas of high vibration levels were difficult to clearly interpret.

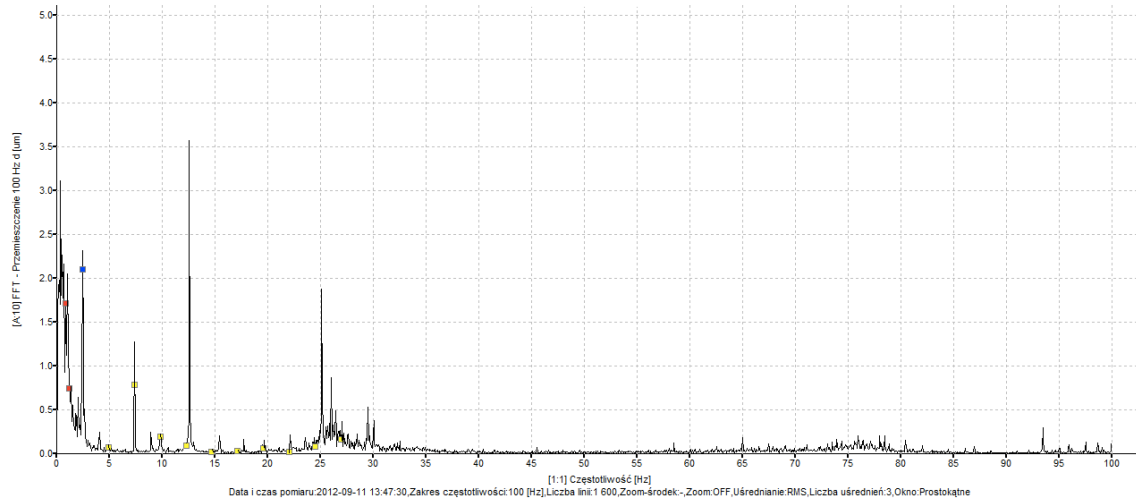


Fig. 4. Frequency spectrum of the vibration amplitudes measured at node III in the direction Y with the selected synchronous frequency of water turbine's shaft at 2.5 Hz (blue dot) and its harmonics (red and yellow dots)

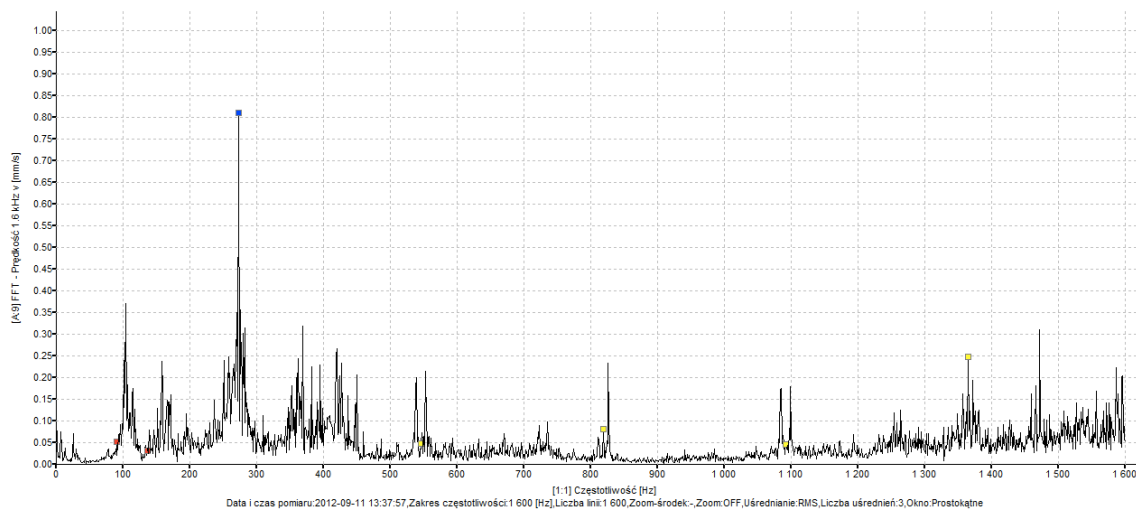


Fig. 5. Frequency spectrum of the vibration velocity measured at measuring node II in the Y direction with the marked frequency of toothed ring meshing with the planetary cage at 272 Hz (blue dot) and its harmonics (red and yellow dots)

The study clearly showed that the cause of elevated levels of rms values of vibration velocity was the operation of planetary gear, and more specifically the lack of smooth cooperation of gears. Since the vibration of the machine was measured on the housing, the registered signal was dominated by vibrations coming from the toothed ring cooperation with the planetary gear. This ring was permanently connected to the gear's body, resulting in the direct transfer of vibrations to the housing.

The analysis conducted of vibrations therefore clearly indicated the source of high level of vibrations, which impacted directly on the acceptable level of vibration (for new objects which are ready for use). The cause of the elevated vibration level was due to the planetary toothed gear. Since this was a new gear, it was unlikely that such quick wearing or damage could have occurred, so this evidenced by low accuracy performance of toothed wheels.

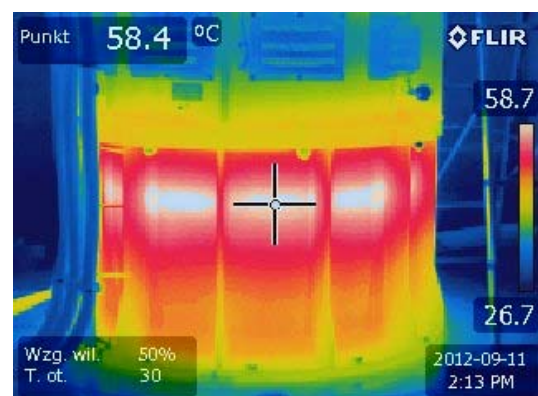


Fig. 6. The temperature distribution on the external surface of the gear housing.

During the assessment of the dynamic state and while searching the defects of the turbine set, supplementary research was conducted in a form of temperature distribution control on the external

surfaces of the housing. Thermovision research of the parts such as bearings and gears allows for the detection of excessive wearing and serious damage, since such defects cause local temperature increase. An infrared camera manufactured by Flir was used in the study (model E50). The study was conducted at the highest load of turbine set (480 kW). One of the thermograms obtained is shown in Figure 6.

In case of the examined water turbine no excessive temperature levels were observed for any of the controlled parts. The highest temperature in the housing of toothed gear was 59.7 °C and it was in the area of connection of toothed ring with the housing (Fig. 6). The temperature on the outer surface of the generator was up to 46.4 °C in the vents, where hot air was removed. Housings design prevented temperature measurement directly on the bearing housing, but the steel elements connected to these retainers had a low temperature. It can be concluded that the control of the temperature distribution showed no symptoms of excessive wearing or damage.

4. CONCLUSIONS

The study of the water turbine with a capacity of 600 kW allowed formulating the following conclusions:

- In the test machine at each of the five tested states the level of RMS value of vibration velocity was exceeded (according to the standard ISO10816-5:2000 for newly commissioned machines),
- The results of measurements allowed to qualify the turbine set for zone B, which according to [3] is the possibility of long-term operation without restrictions,
- The frequency analysis showed that the cause of high levels of vibration was due to the toothed gear operation, and other incompatibilities (e.g. rotors unbalance, bend or misalignment) were at an acceptable level,
- Because studies have shown that the vibration levels were exceeded for the new objects placed in operation, the next inspection of the machine is recommended in the future to detect possible rapid wearing of components (mainly the parts of toothed gear).

REFERENCES

- [1] Niziński S., Michalski R., *Diagnostyka obiektów technicznych*, Biblioteka Problemów Eksploatacji, Radom 2002.
- [2] ISO 10816-1:1995
- [3] ISO 10816-5:2000
- [4] Kiciński J., *Rotor dynamics*, IFFM PAS Publisher, Gdańsk 2006.
- [5] Rao J. S., *Rotor dynamics*, Third Edition, New Age International, New Delhi 2009.

- [6] Barszcz T., *Systemy monitorowania i diagnostyki maszyn*, Wyd. Instytutu Technologii Eksploatacji - PIB, Kraków 2006.
- [7] Barszcz T., Urbanek J., *Monitorowanie i diagnostyka maszyn wirnikowych*, Wyd. Instytutu Technologii Eksploatacji - PIB, Kraków 2008.
- [8] Łączkowski R., *Drgania elementów turbin cieplnych*. WN-T, Warszawa 1974.
- [9] Cempel Cz., *Diagnostyka wibroakustyczna maszyn*, PWN, Warszawa 1989.
- [10] Łazarz B., Wilk A., Madej H., *The diagnosis of planetary gear by means of vibration methods*, Proceed. of the International Congress on Noise Control Engineering, vols 1-3 (1999), pp. 65-70
- [11] Figlus T., Wilk A., Madej H., Łazarz B., *Investigation of gearbox vibroactivity with the use of vibration and acoustic pressure start-up characteristics*, Archive of Mechanical Engineering, Vol. 58, Issue 2 (2011), pp. 209-221.



Grzegorz ŻYWICA, PhD, Eng. Since 2005 has been working at the Institute of Fluid-Flow Machinery PAS in Gdansk, at the Rotor Dynamics and Slide Bearing Department.

In the scientific work he deals with the problems of modelling and computational simulation of the rotating machinery, modal analysis and diagnostics of the machines.



Paweł BAGIŃSKI, M.Sc, Eng., an assistant in the Rotor Dynamics and Slide Bearings Department in the Institute of Fluid-Flow Machinery PAS in Gdansk. Currently a PhD student at Gdansk University of Technology. His main research areas are:

experimental modal analysis, experimental rotor dynamics and numerical modelling of foil bearings.



Łukasz BREŃKACZ, M.Sc, Eng., an assistant in the Rotor Dynamics and Slide Bearings Department in the Institute of Fluid-Flow Machinery PAS in Gdansk. Currently a PhD student at Gdansk University of Technology. His main research areas are:

computational and experimental modal analysis, rotor dynamics and computer aided design.

LEAK DETECTION IN LIQUID TRANSMISSION PIPELINES USING STATISTICAL ANALYSIS

Andrzej SOBOLEWSKI*, Paweł OSTAPKOWICZ**

* Białystok University of Technology, Faculty of Electrical Engineering
Wiejska Street 45C, 15-351 Białystok, Poland, e-mail: a.sobolewski@pb.edu.pl

** Białystok University of Technology, Faculty of Mechanical Engineering
Wiejska Street 45C, 15-351 Białystok, Poland, e-mail: p.ostapkowicz@pb.edu.pl

Abstract

Pipeline leak detection systems based on flow and pressure data from a SCADA are commonly used for supporting maintenance and increasing the reliability and safety of pumping process. Such systems should maintain high sensitivity with minimum number of false alarms over the long term. This paper examines the application of a statistics based leak detection system in a physical model of water pipeline (380-metre-long, 34 mm in internal diameter, made of polyethylene (PEHD)) and compares it to a reference algorithm. Sophisticated statistical analysis techniques constantly evaluate all new and existing information in the database, discard invalid data, and perform leak detection basing only on high-quality information in the current database.

Key words: pipelines, leak detection, statistical analysis.

DETEKCJA PRZECIEKU PŁYNÓW W RUROCIĄGACH ZA POMOCĄ ANALIZY STATYSTYCZNEJ

Streszczenie

Systemy wykrywania przecieków w rurociągach wykorzystujące dane z pomiaru przepływów i ciśnień w układach pomiarowych typu SCADA są często stosowane do wspierania obsługi i zwiększenia niezawodności oraz bezpieczeństwa procesu pompowania. Wymaga się od tego typu systemów wysokiej czułości z jednoczesną odpornością a jednocześnie ograniczenia występowania fałszywych alarmów podczas pracy. W tym artykule przetestowano algorytm detekcji działający wykorzystujący metody analizy statystycznej w fizycznym modelu wodociągu (długość 380 metrów, średnica wewnętrzna 34 mm, materiał polietylen (PEHD)) i porównano go z algorytmem referencyjnym. Zaawansowane techniki analizy statystycznej dokonują ciągłej oceny wszystkich nowych i istniejących informacji w bazie danych, odrzucając dane nieprawidłowe. Celem takiego działania jest dokonywanie detekcji wycieków w wodociągu na podstawie tylko wysokiej jakości informacji w budowanej bazie danych.

Słowa kluczowe: rurociąg, detekcja wycieku, analiza statystyczna.

1. INTRODUCTION

The primary purpose of leak detection systems (LDS) is to assist pipeline controllers in detecting and localizing leaks. LDS alarm and provide leak related data to the pipeline controllers in order to aid the decision-making process. Pipeline leak detection systems are also beneficial because they can enhance productivity and system reliability thanks to reduced downtime and reduced inspection time. Leak detection systems should maintain high sensitivity with minimum number of false alarms over the long term. Most popular leak detection systems are developed with the use of diagnostic methods which are based on measurements of internal flow parameters (flow rate, pressure and fluid temperature) [5, 7, 8]. Elaboration of a leak detection system requires the use of at least several internal methods working concurrently [5]. Systems developed with the use of such methods are usually

additional modules of SCADA systems which are used in pipelines for monitoring, regulation and control of pumping processes.

SCADA systems comprise measuring devices and transducers located along the pipeline and data transmission systems which provide parameter measured flow data (process variables). Due to large distances between measurement points and the control of a SCADA system, it is possible that the LDS will only have part of useful measurement data [6]. In addition, the measurement data are often disturbed by additive measurement noise. In many cases, this limits the use of diagnostic methods such as, for example, the method based on pressure wave detection [4, 5]. Effective application of this method requires not only accurate synchronization of measuring time and continuous reception of pressure signals from individual measurement points along the pipeline (with imposed very short sampling periods), but also a reliable and unambiguous

measurement. Acquisition of data with additive measurement noise is therefore a challenge for algorithms performing continuous measurement data analysis and often limits their effectiveness. Statistical methods, on the other hand, that can be used to estimate parameters and test hypotheses about them prove to be much more effective in such conditions. The paper proposes statistical methods of leak detection that provide an alternative to the methods based on pressure wave detection.

2. DESCRIPTION OF THE LEAK PHENOMENON

A pipeline usually has flowmeters installed on the ends which measure pump forced flow at the inlet and the flow at the outlet. In case of a leak, juxtaposing flows at the inlet and outlet allows for a diagnostic decision to be made. Moreover, pipelines are often equipped with additional pressure sensors installed at regular intervals along the pipeline. They are installed in order to increase the accuracy of leak detection and thus reduce the number of false alarms.

The occurrence of leakage leads to changes of pressure and flow in the pipeline. Leakage is accompanied by the formation and propagation of pressure waves. These waves are produced by a sudden pressure drop at the place of the leakage and propagate from there in both directions of the pipeline with the speed of sound. In the case of sudden leaks waves have clearly visible fronts, and in the case of leakages increasing slowly, due to a milder character of pressure changes, waves have a smoother shape. Behind the wave front, the longer is the distance from the leak point, the smaller is the pressure drop in the pipeline. Example signals of pressure and flow rate in the pipeline without and with leakage are shown in Figure 1. The signals are measured at the inlet and outlet, and in the case of pressure, additionally at several points along the pipeline.

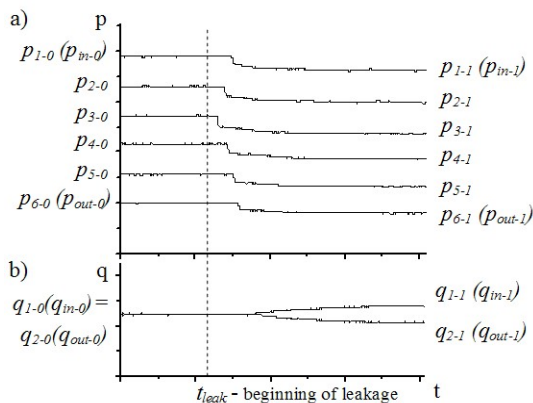


Fig. 1. Pressure profiles a) and flow profiles b) from transducers in the pipeline before and after the occurrence of leakage

For small intensity leaks, when additionally the measurement data are strongly disturbed, the detection of wave front propagation causes a problem. In such situations, it is also difficult to balance the flows. This, however, can be solved using statistical methods which verify hypotheses about changes in the average values of the measured signals basing on the analysis of data collected in n -samples time windows. Fig. 2. shows data disturbed by measurement noise in a time window for one of the signals in the state of a leak at 20th second of data recording.

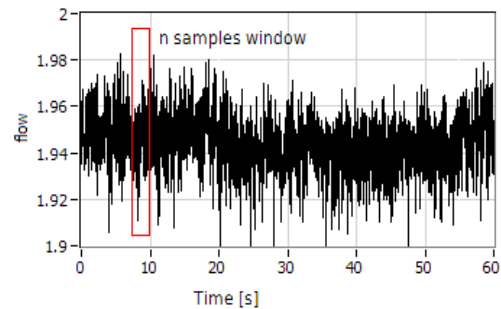


Fig. 2. Data with noise and n -samples window for statistical analysis. Leakage occurs at 20sec

3. SCOPE OF RESEARCH

An important element of this research was to compare the diagnosis of simulated leaks obtained by means of two solutions:

- the reference method. It operates in a continuous cycle and generates diagnostic results each time it receives the signals with a sampling period T_p . It involves the use of pressure and flow signals from two measuring transducers located at the inlet and outlet or, additionally, the use of signals from all pressure transducers located along the pipeline;
- the elaborated statistical-based method. The system receives flow and pressure data from a SCADA (Supervisory Control and Data Acquisition) system and calculates the probability of a leak at regular intervals e.g. every 0.3 seconds. The hypothesis test procedure is used in order to determine signal mean change probability.

2.1. Description of the reference method

A detection algorithm presented in [2] was used. The algorithm is using measurement signals from two devices (sensors) located at the beginning and end of the pipeline (Fig. 3). The signals which were used were pressure signals p_{in} and p_{out} and, for comparison, measured signals of the flow q_{in} and q_{out} . The algorithm includes:

- recursive filtering of signals using a recursive filter with a low-pass characteristics –

- recursive averaging with fading memory (exponential smoothing) – the results of which are reference values for the calculation of deviations Δx_{in} and Δx_{out} ;
- calculation of the maximum of the correlation function of the deviations Δp_{in} and Δp_{out} for the pressure signals, and the minimum of the correlation function of deviations Δq_{in} and Δq_{out} for the flow signals for the time shift τ_{max}^A . The shift value τ_{max}^A is determined using the velocity of the pressure wave propagation and taking into account the distance between the pressure measurement points;
- recursive filtering of the calculated extremes of the correlation functions with the resulting values F_x (F_p and F_q respectively) which, when they exceed the alarm threshold P_x (P_p and P_q respectively) inform about the occurrence of leakage.

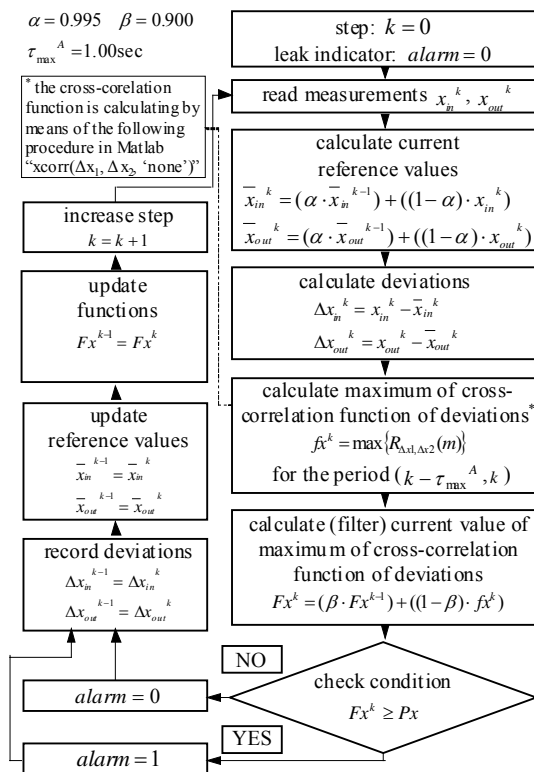


Fig. 3. The reference algorithm

The algorithm can also operate with the use of a larger number of signals. In this case, the pressure signals measured at the inlet and outlet and also in the other points along the pipeline were used. The resulting function here is the function \overline{Fp} . This function is the medium value of a set of $n-1$ functions Fp_n based on the calculation of the cross-correlation of the variables Δp_n . Particular functions Fp_n are the result of filtration of the functions fp_n

based, in turn, on a recursive filter, referred to as recursive averaging with fading memory (exponential smoothing). The individual functions fp_n are the maximum values of the cross-correlation function which corresponds to the correlation of the variable Δp_n . The variable represents a given measuring point z_n with the variable Δp_{n+1} which, in turn, represents the neighbouring measuring point z_{n+1} located along the pipeline. The cross-correlation functions are calculated with the time shift τ_{max}^B . The shift value τ_{max}^B is determined using the velocity of the pressure wave propagation and taking into account the distance between the pressure measuring points. If the function \overline{Fp} exceeds its alarm threshold \overline{Pp} , the alarm is generated.

2.2. Description of the elaborated method

The proposed method is based on statistical analysis of pressure/flow signals at several points in the pipeline in order to detect a leak. A leak changes the hydraulics of the pipeline and therefore changes the pressure or flow readings after some time. Local monitoring of flow at the beginning and the end of the pipeline can therefore provide a simple way of detecting leaks. However, in order to minimize false alarms and properly identify changes in the pressure and flow signals when a leak occurs, it is necessary to read data from several points. This gives the opportunity of optimizing leak detection provided that some statistical assumptions hold. The uncertainty of the mean value of the measured data requires the estimation of its real value by calculating confidence intervals (CI) and its limits. A confidence interval for a mean specifies a range of values within which the unknown population parameter, in this case the mean, may lie. CI for means are calculated as follows:

$$P\left(|m - \mu_0| < u_{\alpha/2} \frac{s}{\sqrt{n}}\right) = 1 - \alpha \quad (1)$$

where:

- P probability value
- $1-\alpha$ confidence level.
- s estimated standard deviation
- m estimated mean
- μ_0 unknown population mean
- n number of samples
- $u_{\alpha/2}$ normal distribution = 1.96 for confidence level 0.95

Confidence intervals (CI) for means are calculated for each of the measured data intervals. Limits of the interval will be used as a reference for the detection of transducer signal mean change. The (two sided) confidence interval for a mean contains all the values of μ_0 (the true population mean) which

would not be rejected in the two-sided hypothesis test of:

$H_0: m = \mu_0$ (no significant mean change)
against

$H_1: m$ not equal to μ_0 (a significant mean change)

To minimize false alarms, P-value, the strength of evidence in support of a null hypothesis, is averaged over all data sets. It allows setting a custom threshold for leak detection. A leak is detected if the average P-value exceeds the custom threshold (50% in the work). Otherwise, the leakage is not detected.

2.3. Description of the algorithm

The existence of noisy data makes it necessary to choose a time window length, e.g. 0.3 sec, and calculate the confidence interval and its limits for all considered signals. The limits may be used as a start up parameters. The next step is to move the time window and perform a hypothesis test for all signal means, taking as the start up references the CI limits, and then calculate P -values as a hypothesis test result. Each signal has its P -value. If the average of P -values is smaller than the threshold, the current measurements should be added to the previous ones and new confidence limits should be calculated. This operation extends the database so that mean estimation can be performed more precisely in further calculations (Fig. 4). If the average of P -values exceeds the threshold, the leak is detected (Fig. 5).

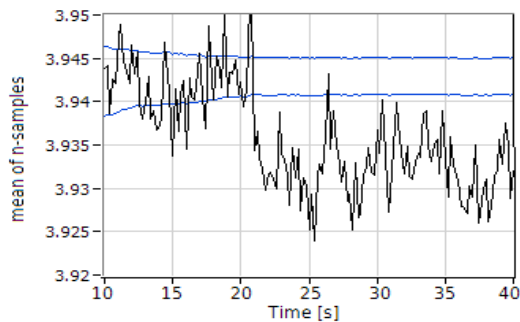


Fig. 4. The n -samples window means and confidential interval limits for a chosen signal.
Leakage occurs at 20sec

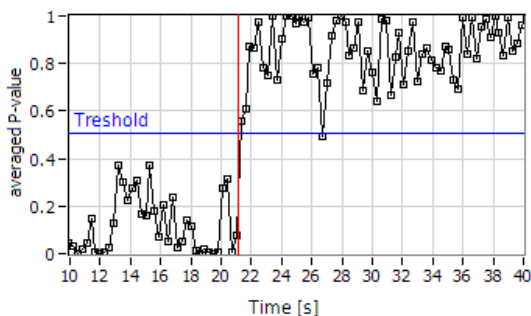


Fig. 5. P -value averages and the chosen threshold.
Leakage occurs at 20sec

3. VERIFICATION EXPERIMENTS ON A PHYSICAL MODEL OF A WATER PIPELINE

The elaborated technique has been tested on a test stand with a physical model of a water pipeline. The scheme of the test stand is shown in Figure 6, Figures 7 and 8 show the general scheme and the view of the pipeline model.

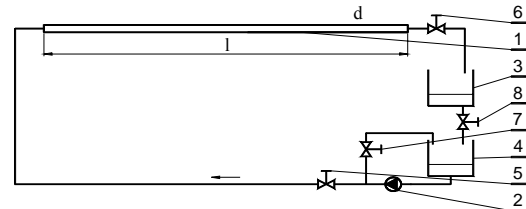


Fig. 6. Laboratory plant scheme1 – pipeline; 2 – pump; 3, 4 – tanks; 5, 6 – stations of control valves; 7 – control valve; 8 – bleeding valve

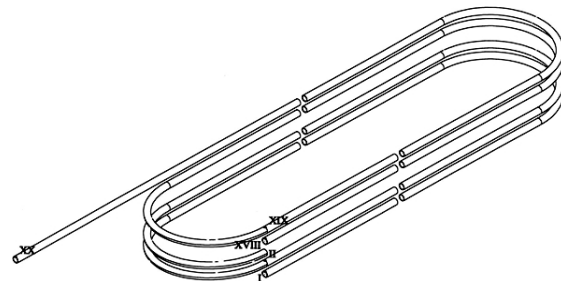


Fig. 7. Scheme of the pipeline
I – the inlet, II – the outlet



Fig. 8. View of the pipeline

The pipeline is 380 meters long and is made of polyethylene (PEHD) pipes which are 34 mm in internal diameter and 40 mm in external diameter. It consists of three sections each of which is over one hundred meter long. The sections: 0÷140 m, 140÷280 m and 280÷380 m, are joined with the use of special connectors which have the same diameter as the pipeline. The model pipeline is equipped with standard measuring devices: two electromagnetic flow meters, six pressure transducers and two thermometers. They are connected to a PC equipped with a 16 bit A/D converter. Table 1 contains

information about the location and meteorological characteristics of the sensors and the measurement system. Proportionally controlled solenoid valves were used to simulate leakage. The valves were installed in several selected points in the pipeline.

Table. 1. Characteristics of the elements of the measuring system

devices	pressure transducers	flow rate transducers
location [m]	$P_{1(in)}=1; P_3=61;$ $P_4=141; P_5=201;$ $P_6=281; P_{2(out)}=341$	$Q_{1(in)}=-6;$ $Q_{2(out)}=382,2;$
range	0÷10 [bar]	0÷200 [l/min]
accuracy	0.1 % of range	0.2 % of range
uncertainty of measurement*	±0.012 [bar]	±0.44 [l/min]
* uncertainty of measurement = transducer + 16-bit converter		

3.1. Research conditions

Before each simulation of a leakage the pipeline operated under steady-state conditions. The tests included slowly simulated leakages. The following settings of the operating point of the pipeline were used: inlet pressure $p_{in-0} \approx 6.0$ bar, outlet pressure $p_{out-0} \approx 1.0$ bar, nominal flow rate $q_{in-0} \approx 120$ l/min, temperature of the pumped medium $T_{water} \approx 20$ °C. In order to simulate leakages, solenoid valves were installed in several points along the pipeline. Measured signals were sampled with the frequency $f_p = 100$ Hz. The tests included simulated leaks of a size of 0.02 ÷ 4.00% of the nominal flow rate q_{in-0} at 155th and 235th meter of the pipeline. The leaks were slowly increasing, which means that they reached the nominal value some time after the moment of their occurrence. Two tests were performed for a given leakage size. From the diagnostic point of view the chosen way of simulating leaks was not too favourable, since the resulting phenomenon of pressure wave propagation is characterized by a smooth shape of wave fronts. Commonly used diagnostic method based on the detection of pressure waves can be in this case not very effective.

4. RESULTS OF TEST WITH SIMULATED LEAKS

An important element of the research was the comparison of the detection times (i.e. response times) of simulated leaks obtained by means of the reference method with the results obtained using the elaborated statistical method. The results are shown in Table 2. All times are given in seconds. They were measured from the moment of the opening of the valves. The results are the mean values of the two tests for a given size of the leak. The sign “-” in the table means that the algorithm did not detect the given leakage.

4.1. Application of the reference method

Three variants were considered for the method: variant “A” – involving the use of two pressure signals p_{in} and p_{out} , variant “B” – involving the use of two stream signals q_{in} and q_{out} (the signals in both variants were measured at the inlet and outlet of the pipeline), and additional variant “C” – involving the use of a package of two pressure signals measured at the inlet and outlet and additional four pressure signals measured along the pipeline.

The choice of alarm thresholds was based on the established minimum threshold values that ensured no alarm in states without leakage (in the whole series of tests). In the case of the algorithms based on two signals the values of alarm thresholds were $Pp = 0.0115$ and $Pq = -0.0100$, respectively, whereas in the case of the algorithm with six pressure signals the alarm threshold was $\overline{Pp} = 0.00490$. For individual algorithms, the following parameter values were used: $\alpha = 0.995$, $\beta = 0.900$, $\tau_{max}^A = 1$ sec, and $\tau_{max}^B = 0,25$ sec.

Also some additional information may be useful for determining the possible level of leak detection. Such a piece of information is the difference between the mean values for individual flow and pressure signals, before and after the leak, calculated basing on the profiles and taking into account the fact of exceeding the field of the measurement uncertainty. The results of this analysis are shown in Table 2 which, for a given signal, provides the comparison of its mean value (calculated for a 5-second interval which started 5 seconds after the start of the leak) with the mean value before the leak (calculated for three consecutive 5-second intervals, where the end of the last interval ended just before the start of the leak). If, for the two tests, for a given simulated leak size, the difference in mean values exceeded the field of measurement uncertainty, then such a case was marked by a “+”, and the reverse case was marked by a “-”. If, however, for individual tests, for a given size of the leak, it was ambiguous, such a case was marked by “-/+”.

4.2. Application of elaborated method for simulated leak detection

The following paragraph presents examples of two averaged P-values in the case of leakage occurring at 20s. Fig. 8. shows P-value averages for a 0,37% leak. The leak was detected at 24.1s. In contrast, the 50% probability threshold is exceeded at 21.30s in the case of 1.19 % q_0 leakage (Fig. 9). Table 2 presents the comparison of leak detection time for leakages at 155m and 235m respectively in relation to the size of the leakage.

Table 2. Times of detection of simulated leakages

leakages			changes of mean values				reference method			elaborated method		
							A	B	C	D	E	F
[m]	[l/min]	[% q_0]	P_{in}	P_{out}	q_{in}	q_{out}	P_{in} , P_{out}	q_{in} , q_{out}	six pressure signals	P_{in} , P_{out}	q_{in} , q_{out}	six pressure signals
155	0.09	0.07	-	-	-	-	-	-	-	-0,80	7,30	11.70
	0.17	0.14	-	-	-	-	-	-	-	-5,30	7,75	9.10
	0.28	0.23	-	-	-	-	-	-	-	-4,70	8,50	6.10
	0.44	0.36	-	-	-	-	-	-	-	-5,60	6,70	1.90
	0.77	0.63	+	-	-	-/+	1.62	2.89	1.12	1,20	2,65	1.45
	1.19	0.97	+	-	-	+	1.69	3.38	1.16	-6,80	2,65	1.30
	1.55	1.28	+	+	-/+	+	1.55	2.87	1.12	0,60	3,10	1.00
	1.84	1.51	+	+	+	+	1.43	3.04	1.07	1,30	2,50	1.30
	2.20	1.81	+	+	+	+	1.75	2.86	1.23	-4,40	2,80	1.30
	2.55	2.10	+	+	+	+	1.59	2.81	1.08	1,15	2,35	1.45
235	2.89	2.37	+	+	+	+	1.56	2.75	1.15	-0,80	2,85	1.30
	3.19	2.62	+	+	+	+	1.58	2.95	1.10	-0,50	2,80	1.45
	0.04	0.03	-	-	-	-	-	-	-	19,90	12,10	20.35
	0.11	0.09	-	-	-	-	-	-	-	7,55	12,10	27.25
	0.37	0.31	-	-	-	-	-	-	-	1,90	7,30	3.40
	0.78	0.65	+	-	-	+	-	4.44	1.37	1,60	3,10	1.60
	1.18	0.97	+	+	-	+	2.06	3.58	1.38	1,90	2,95	1.45
	1.55	1.28	+	+	-	+	2.00	2.85	1.36	1,90	2,50	1.60
	1.77	1.46	+	+	-	+	1.95	3.19	1.34	1,75	3,10	1.60
	2.06	1.70	+	+	-/+	+	1.97	3.25	1.34	1,85	3,10	1.60
2.37	1.96	+	+	-/+	+	1.93	3.38	1.35	-0,80	7,30	11.70	

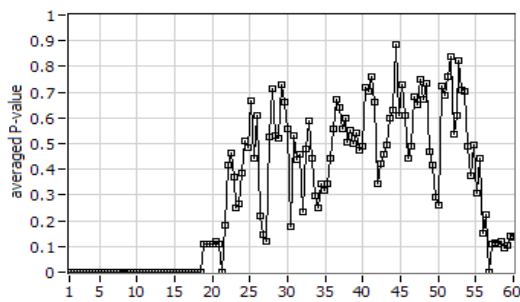


Fig. 8. P-value averages. 0,37% q_0 leak at 20s.
Average P-value exceeds 50% at 24.10s

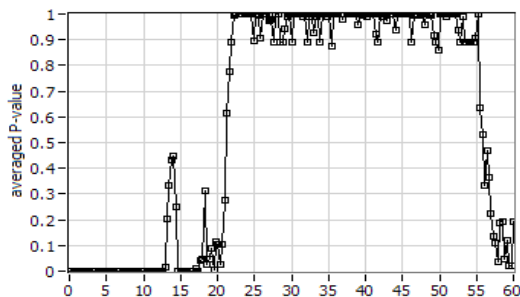


Fig. 9. P-value averages. 1,19% q_0 leak at 20s.
Average P-value exceeds 50% at 21.30s

The results in columns "C" and "F" (including the results for all available pressure signals) clearly show that for all leakage sizes the statistically oriented method is more sensitive and faster in some

cases than the reference method. The use of the statistical approach ensures detection even for leakages smaller than 0.5%, whereas the reference method is able to detect leakages of approximately 0.77% q_0 . Even though the use of the statistical method allows for detecting very small leakages, the time of detection is about ten times longer than for leakages over 1% q_0 . However, the column "D" includes results only for two pressure signals p_{in} , p_{out} . Some of the time values are negative, which should be interpreted as false alarms. When the method uses only few signals, the results are less certain.

4. SUMMARY

The use of algorithms operating on a continuous basis may be exposed to the risk of significant errors and disturbances occurring in individual moments of measuring pressure and flow signals or even the lack of data. The measurement data for a LDS should be provided periodically in a continuous manner and without significant delays. However, even the most advanced measuring systems installed on transmission pipelines are not completely resistant to interference, including errors associated with the transmission of data on such long distances.

In such situations, statistical methods prove to be a good solution. They are characterized by a short time of leak detection, high sensitivity, and accuracy. They are also very easy in application and

do not involve advanced analysis methods. Statistically oriented approach gives more accurate results, because the detection is more sensitive and fast as well in comparison with the reference method.

REFERENCES

- [1] Billman L., Isermann R., *Leak detection methods for pipelines*, *Automatica*, 1987, 23 pp. 381-385.
- [2] Ostapkowicz P., *Improving the efficiency of diagnosing of leaks from liquid transmission pipelines by using the new diagnostic information - the signals of weak interactions between objects*, *Solid State Phenomena*, 2009, 147-149 pp. 492-497.
- [3] Siebert H., Isermann R., *Leckerkennung und Lokalisierung bei Pipelines durch on-line Korrelation mit einem Prozesrechnes*, *Regelungstechnik*, 1977, 25 pp. 69-74.
- [4] Sobczak R., *The pipeline leakage location method by following the pressure wave front*, *Chemical Industry*, 2004, 83 pp. 296-299.
- [5] Turkowski M., Bratek A., Słowikowski M., *Methods and systems of leak detection in long range pipelines*, *J. of Automation, Mobile Robotics & Intelligent Systems*, 2007, 1 pp. 39-46.
- [6] Zhang J., *Statistical pipeline leak detection for all operating conditions*, *Pipeline & Gas Journal*, 2001, 2 pp. 42-45.
- Reference to a chapter in an edited book:
- [7] Kowalczyk Z., Gunawickrama K., *Detecting and locating leaks in transmission pipelines*, in.: Korbicz K.J., Koscielny J.M., Kowalczyk Z., Cholewa W. (Eds.), *Fault Diagnosis: Models, Artificial Intelligence, Applications*, Springer-Verlag, Berlin, 2004, pp. 822-864.
- [8] ADEC - Alaska Department of Environmental Conservation, *Technical review of leak detection technologies for crude oil transmission pipelines*, *Proceedings of the Pipeline Reliability Conference*, 1996, Houston, USA.

The research work financed with the means of the Ministry of Science and Higher Education (Poland) in the years 2010-2013 as the research project Nr N N504 494439.



Andrzej SOBOLEWSKI, Ph.D, Employee of the Faculty of Electrical Engineering since 1998 Bialystok University of Technology. Doctoral thesis in the field of technical diagnostics of electrical machines defended in 2008

Currently employed as a lecturer in the Department of Automation and Electronics. The main directions of research are diagnostics and fault detection and modern control methods.



Paweł OSTAPKOWICZ, Ph.D. Graduate and employee of the Faculty of Mechanical Engineering at Bialystok University of Technology since 1998. Doctoral thesis in the field of technical diagnostics of machines in 2007. Currently employed as a lecturer in the

Department of Automatics and Robotics. The main directions of research are diagnostics and fault detection methods, design and operation of machines, vibroacoustics.

Diagnostyka

APPLIED STRUCTURAL HEALTH, USAGE AND CONDITION MONITORING

Obszar zainteresowania czasopisma to:

- ogólna teoria diagnostyki technicznej
- eksperymentalne badania diagnostyczne procesów i obiektów technicznych;
- modele analityczne, symptomowe, symulacyjne obiektów technicznych;
- algorytmy, metody i urządzenia diagnozowania, prognozowania i genezowania stanów obiektów technicznych;
- metody detekcji, lokalizacji i identyfikacji uszkodzeń obiektów technicznych;
- sztuczna inteligencja w diagnostyce: sieci neuronowe, systemy rozmyte, algorytmy genetyczne, systemy ekspertowe;
- diagnostyka energetyczna systemów technicznych;
- diagnostyka systemów mechatronicznych i antropotechnicznych;
- diagnostyka procesów przemysłowych;
- diagnostyczne systemy utrzymania ruchu maszyn;
- ekonomiczne aspekty zastosowania diagnostyki technicznej;
- analiza i przetwarzanie sygnałów.

Wszystkie opublikowane artykuły uzyskały pozytywne recenzje wykonane przez niezależnych recenzentów.

Topics discussed in the journal:

- General theory of the technical diagnostics,
- Experimental diagnostic research of processes, objects and systems,
- Analytical, symptom and simulation models of technical objects,
- Algorithms, methods and devices for diagnosing, prognosis and genesis of condition of technical objects,
- Methods for detection, localization and identification of damages of technical objects,
- Artificial intelligence in diagnostics, neural nets, fuzzy systems, genetic algorithms, expert systems,
- Power energy diagnostics of technical systems,
- Diagnostics of mechatronic and antropotechnic systems,
- Diagnostics of industrial processes,
- Diagnostic systems of machine maintenance,
- Economic aspects of technical diagnostics,
- Analysis and signal processing.

All the published papers were reviewed positively by the independent reviewers.

Redaktorzy działowi:

dr hab. inż. Tomasz BARSZCZ, prof. AGH
dr hab. Andrzej BIELECKI, prof. AGH
prof. dr hab. inż. Wojciech CHOLEWA
prof. dr hab. Wojciech MOCZULSKI
prof. dr hab. inż. Stanisław RADKOWSKI
prof. dr hab. inż. Wiesław TRAMPCZYŃSKI
prof. dr hab. inż. Tadeusz UHL

Kopia wszystkich artykułów opublikowanych w tym numerze dostępna jest na stronie www.diagnostyka.net.pl

Druk:

Centrum Graficzne „GRYF”, ul. Pieniężnego 13/2, 10-003 Olsztyn, tel. / fax: 89-527-24-30

Oprawa:

Zakład Poligraficzny, UWM Olsztyn, ul. Heweliusza 3, 10-724 Olsztyn
tel. 89-523-45-06, fax: 89-523-47-37

Wszystkie opublikowane w czasopiśmie artykuły uzyskały pozytywne recenzje, wykonane przez niezależnych recenzentów.

Redakcja zastrzega sobie prawo korekty nadesłanych artykułów.

Kolejność umieszczenia prac w czasopiśmie zależy od terminu ich nadesłania i otrzymania ostatecznej, pozytywnej recenzji.

Wytyczne do publikowania w DIAGNOSTYCE można znaleźć na stronie internetowej:
<http://www.diagnostyka.net.pl>

Redakcja informuje, że istnieje możliwość zamieszczania w DIAGNOSTYCE ogłoszeń i reklam.

Jednocześnie prosimy czytelników o nadsyłanie uwag i propozycji dotyczących formy i treści naszego czasopisma.

Zachęcamy również wszystkich do czynnego udziału w jego kształtowaniu poprzez nadsyłanie własnych opracowań związanych z problematyką diagnostyki technicznej. Zwracamy się z prośbą o nadsyłanie informacji o wydanych własnych pracach nt. diagnostyki technicznej oraz innych pracach wartych przeczytania, dostępnych zarówno w kraju jak i zagranicą.